Internal Field NMR of Cobalt nanoparticles in catalysts : size effects and particle-support interaction

Ilia Iakovlev

THÈSE DE DOCTORAT

DE L'UNIVERSITÉ PSL

Préparée à l'Ecole Supérieure de Physique et de Chimie Industrielles de la ville de Paris (ESPCI Paris PSL)
Dans le cadre d'une cotutelle avec Novosibirsk State University

RMN en champ interne de nanoparticules de cobalt dans des catalyseurs - effets de taille et interactions avec le support

Internal Field NMR of Cobalt nanoparticles in catalysts - size effects and particle-support interaction

Soutenue par
Ilia IAKOVLEV
Le 1 décembre 2022

Ecole doctorale n° 397
Physique et Chimie des Matériaux

Spécialité
Chimie théorique, physique, analytique

Composition du jury :

Franck, FAYON — *Président*
Directeur de recherche, CEMHTI – UPR3079 CNRS, Orléans

Elena, BAGRYANSKAYA — *Rapporteur*
Directrice, Novosibirsk Institute of Organic Chemistry SB RAS

Laurent, Le POLLES — *Rapporteur*
Maître de conférences,
Ecole Nationale Supérieure de Chimie de Rennes

Geoffrey, BODENHAUSEN — *Examinateur*
Professeur, Ecole Normale Supérieure PSL

Guillaume, LANG — *Examinateur*
Chargé de recherches, CNRS, ESPCI Paris PSL

Jean-Baptiste, d'ESPINOSE de LACAILLERIE
Professeur, ESPCI Paris PSL — *Co-directeur de thèse*

Olga, LAPINA — *Co-directeur de thèse*
Professeur, Novosibirsk State University

Table of Contents

General Introduction 1

Chapter 1: Literature review 4

1.1 Nuclear magnetic resonance inside ferromagnetic materials 4

1.1.1 Magnetic susceptibility of the interacting system of nuclei and electrons system 5

1.1.2 Domain structure. Domain walls. Demagnetizing field. 9

1.2 Application of the Internal Field NMR spectroscopy technique for ^{59}Co nuclei 14

1.2.1 Demagnetizing field. Structure of hyperfine field 15

1.2.2 Spin echo in ferromagnetic materials 17

1.2.3 Magnetic anisotropy energy and superparamagnetism 20

1.3 Experimental observations of the ^{59}Co Internal Field nuclear magnetic resonance 22

1.3.1 Metallic cobalt 22

1.3.2 Binary cobalt compounds 25

1.3.3 Superparamagnetic cobalt compounds 27

1.4 Functional materials based on cobalt nanoparticles 29

1.4.1 Fischer-Tropsch catalysts 29

1.5 References 31

Chapter 2: Experimental methods 41

2.1 ^{59}Co Internal Field NMR 41

2.2 Additional characterization techniques 44

2.3 Sample synthesis 44

2.4 References 44

Chapter 3: Superparamagnetic behavior of Co nanoparticles supported by multi-walled carbon nanotubes 45

3.1 Introductory comments 45

3.2 Superparamagnetic behaviour of metallic Co nanoparticles according to variable temperature magnetic resonance 46

3.2.1 Abstract 46
3.2.2 Introduction 47
3.2.3 Experimental 48
3.2.4 Results and Discussion 51
3.2.5 Conclusions 62
3.3 Supplementary materials 63
3.4 Conclusion 65
3.5 References 67
Chapter 4: Influence of alumina crystal planes on the structure of Co nanoparticles in model Fischer-Tropsch catalysts 69
4.1 Introductory comments 69
4.2 Crystal plane dependent dispersion of cobalt metal on metastable aluminas 70
4.2.1 Abstract 70
4.2.2 Introduction 71
4.2.3 Experimental 73
4.2.4 Results 75
4.2.5 Discussion 89
4.2.6 Conclusions 91
4.3 Supplementary materials 93
4.4 Conclusion 95
4.5 References 97
General conclusions 104

List of abbreviations

bcc – base-centered cubic

BET – Brunauer-Emmett-Teller technique

fcc – face-centered cubic

hcp – hexagonal close-packed

IF NMR – internal field nuclear magnetic resonance

MWCNT – multi-walled carbon nanotube

TEM – transmission electron microscopy

RF – radio frequency

FID – free induction decay

HFI – hyperfine interaction

FTS – Fischer-Tropsch synthesis

FMR – ferromagnetic resonance

NMR – nuclear magnetic resonance

DFT – density functional theory

HAADF-STEM – high-angle annular dark-field scanning transmission electron microscopy

MAS – magic angle spinning

γ – gyromagnetic ratio

$\widehat{H}_Z$ – Zeeman Hamiltonian

ν_L – Larmor frequency

Ω_N – nuclear Larmor frequency

Ω_e – electronic Larmor frequency

η – enhancement factor

λ_m – molecular field parameter

T_2 – spin-spin relaxation constant

K_{Eff} - effective magnetic anisotropy constant

τ_0 – superparamagnetic relaxation time constant

τ_m – characteristic time of the experiment

T_B – blocking temperature

V_B – blocking volume

General Introduction

Metallic nanoparticles and composite materials containing them have found application in many scientific and technical fields, such as heterogeneous catalysis, energy storage, electromagnetic radiation absorption, medicine, etc. Of particular interest are metallic cobalt nanoparticles, which demonstrate high efficiency in heterogeneous catalysis combined with a relatively low cost. The functional properties of cobalt nanoparticles depend on many possibly interrelated factors, such as size, shape, crystal and magnetic structures. In addition, the particle size is distributed in most samples and the shape of the particle size distribution is important for practical applications. Thus, studying the structure of cobalt nanoparticles is an important problem in the design and synthesis of functional composite materials based on them.

Different physical methods can be used to study cobalt nanoparticles, with their own advantages and disadvantages. For example, electron microscopy methods, which provide the possibility to examine cobalt nanoparticles with atomic resolution, have a significant disadvantage, namely their local character. The widely used X-ray diffraction technique is limited when applied to very small or defective particles, which are often the most effective in terms of chemical reactivity.

One of the most informative techniques for studying functional materials is solid-state nuclear magnetic resonance (NMR) spectroscopy. NMR spectroscopy is a generic method than can be employed in a variety of experiments giving access to a large range of structural information despite its low sensitivity.

^{59}Co Internal Field NMR (^{59}Co IF NMR) stands out among other NMR approaches. In contrast to conventional NMR, in this case, resonant absorption of radiofrequency (RF) radiation occurs in the absence of an external magnetic field due to the presence of the strong local magnetic fields inside the ferromagnetic Co particles produced by the collective behavior of electronic magnetic moments. This technique makes it possible to obtain various data on the structure of cobalt particles, namely, their crystal and magnetic structures, the presence of defects and alloying, as well as data on the particle size. This method remains somewhat confidential despite the fact that it has been applied for more than 60 years. This is probably due to the large number of factors influencing the shape and position of the resonance lines making the analysis of ^{59}Co IF NMR a complex task. As a result, the potential of this method as applied to cobalt nanoparticles is far from being fully exhausted.

In that respect, this work focused on the relationship between the ^{59}Co IF NMR signal and two aspects of importance for heterogeneous catalysis: particle size distribution and particle-support interaction.

In order to fulfill these aims, the following objectives were completed:

- Obtaining model systems of cobalt particles in or on multi-walled carbon nanotubes to study the effect of superparamagnetism and paramagnetism in particles of narrow particle size distribution;

- Describing the structure of the obtained systems by ^{59}Co IF NMR and additional physical and chemical methods;

- Using the Neel superparamagnetism model to describe the behavior of the samples at various temperatures in NMR experiments;

- Obtaining model cobalt catalysts deposited on alumina support to study the influence of the support surface on the structure of the deposited particles;

- Characterizing the obtained samples by NMR spectroscopy and additional methods;

- Proposing a model describing the interaction of cobalt nanoparticles with the alumina support surface.

This manuscript is structured as follows.

In **Chapter 1**, we will review the necessary physical phenomena to comprehend ^{59}Co IF NMR. Then we provide a literature review of ^{59}Co IF NMR in different forms of pure cobalt metal as well as binary alloys. Finally, we will provide a brief overview of heterogeneous catalysis by cobalt nanoparticles.

In **Chapter 2**, we will describe the experimental approaches used in this work with the main focus on data acquisition and treatment in ^{59}Co Internal Field NMR. We will summarize the spectral intensity corrections applied during the data treatment in order to extract the quantitative information. A brief description of supplementary experimental techniques used for characterization of the samples will be given.

Chapter 3, is devoted to the investigation of the influence that the size of Co nanoparticles has on the shape and intensity of ^{59}Co Internal Field NMR spectra. This size effect is demonstrated on the model sample of Co nanoparticles embedded inside multi-walled carbon nanotubes that undergo a transition from superparamagnetic to ferromagnetic state after the decrease of experimental

temperature. The core content of this chapter has been published as a peer reviewed article in *Physical Chemistry Chemical Physics*.

In **Chapter 4** we will demonstrate the dependence of crystal structure of Co nanoparticles on the structure of the support surface. The supports in this work are represented by two distinct metastable phases of aluminum oxide γ-Al_2O_3 and χ-Al_2O_3 that possess noticeably different surface crystal planes and hydroxyl coverages. The core content of this chapter is under review as an article in *The Journal of Catalysis*.

Chapter 1: Literature review

1.1 Nuclear magnetic resonance inside ferromagnetic materials

The phenomenon of nuclear magnetic resonance (NMR) manifests itself as the resonant absorption of radio frequency radiation by nuclei with non-zero spin placed in a magnetic field[1]. The interaction of the nuclear spin **S** (here and below, boldface denotes vector quantities) of gyromagnetic ratio γ with an external magnetic field $\mathbf{B_0}$ is described by the Zeeman spin Hamiltonian:

$$\widehat{H}_Z = -\hbar\gamma \boldsymbol{B_0}.\widehat{\boldsymbol{S}} \tag{1.1}$$

where γ is the gyromagnetic ratio of the nucleus, a constant value related to the nature of the nucleus under study. The splitting of the energy levels corresponding to different projections of the spin onto the dedicated axis (coinciding with the direction of the external magnetic field) makes it possible to observe magnetic dipolar transitions between the energy levels when irradiated at the Larmor frequency:

$$\nu_L = \frac{\gamma}{2\pi} B_0 \tag{1.2}$$

In the classic version of the NMR experiment, the sample is placed in a strong constant external magnetic field with an induction of 5-20 T (which corresponds to Larmor frequencies in the range of 20-1000 MHz). Information about the structure of the sample under study is extracted from various interactions of the nuclear spin (chemical shielding by its own electron shell, dipole-dipole and quadrupole interactions), which lead to a shift in the resonant frequency. In the overwhelming majority of cases, the energy of interaction with an external magnetic field exceeds all the sample's internal interactions by many orders of magnitude, and the resulting relative shift of the resonant frequency from the Larmor frequency lies in the range 10^{-6}-10^{-3}.

A completely different picture is observed in the case of studying magnetically ordered substances, namely ferromagnets, when in presence of a system of strongly coupled electronic

[1] Here and below, for brevity, the generalized term "magnetic field" will refer exclusively to the B field, which is strictly called "magnetic induction" or "magnetic flux density" and measured in T (SI) and G (CGS). It is this field that determines the amount of torque applied to a magnetic moment by both external and internal sources. At the same time, the term "magnetic field" is often used to denote the field H, which is also called "magnetic field strength" and is connected with external sources such as free currents (as opposed to the bound magnetization currents) and measured in A/m (SI) and Oe (CGS). In most parts of this chapter, we are following the torque exerted on the nuclear magnetic moment (which is the reason for the precession of the latter) and thus only the B-field is of interest to us. When considering the demagnetizing field, a clear distinction between fields B and H will be made.

magnetic moments interacting with the nuclear spins. The induction of the local magnetic field generated by electrons at the location of the nucleus can reach and often exceed the induction of magnetic fields used in common NMR spectrometers. For example, the induction of the local magnetic field in metallic cobalt (fcc packing), first calculated by Marshall [1] and measured in the NMR experiment by Gossard and Portis [2], [3], is about 21 T, which is comparable in magnitude to the most advanced NMR systems with a magnet having a field of 23.5 T. Such a value of the local magnetic field makes it possible to observe nuclear magnetic resonance in the absence of any constant external magnetic field, i.e. the interaction of nuclear magnetic moments with the local field generated by the subsystem of bound electrons should be considered as the main interaction lifting the degeneracy of the nuclear spin energy levels.

1.1.1 Magnetic susceptibility of the interacting system of nuclei and electrons system

The mathematical calculations on which the description of this interaction is based can be found in [4]. In this manuscript, only the main provisions and conclusions that are directly related to the case of nuclear magnetic resonance in the local field of the sample in the absence of an external constant magnetic field are presented. As mentioned above, in the case of NMR inside a local field, in addition to the subsystem of nuclear spins, we must consider the subsystem of electron spins, which generates the magnetic field experienced by the nuclei. Moreover, unlike the static field encountered in classical NMR, this field does not have a constant value, since the state of the electronic subsystem changes under the influence of the external radio frequency field, the magnetic anisotropy field, the demagnetizing field and the field generated by the nuclei subsystem. To describe the behavior of such a coupled system, one can on first analysis use the classical vectorial approximation. The system of classical Bloch equations for the magnetization of the nuclear (**m**) and electron (**M**) subsystems then reads:

$$\frac{d\boldsymbol{m}}{dt} = \gamma_N[\boldsymbol{m} \times \boldsymbol{b}] + \boldsymbol{r} \tag{1.3}$$

$$\frac{d\boldsymbol{M}}{dt} = \gamma_e[\boldsymbol{M} \times \boldsymbol{B}] + \boldsymbol{R} \tag{1.4}$$

where γ_N and γ_e are the gyromagnetic ratios of nuclei and electrons, respectively; **r** and **R** are relaxation terms, and **b** and **B** are effective magnetic fields acting on the nuclear and electronic subsystems, respectively. In this case, the molecular (mean) field theory allows to approximate the effective magnetic fields (magnetic fields generated by the magnetizations of each of the subsystems):

$$\boldsymbol{b} = \boldsymbol{B_1} e^{i\omega t} + \lambda_m \boldsymbol{M} = \boldsymbol{B_1} e^{i\omega t} + \boldsymbol{B_{hf}} \tag{1.5}$$

$$\boldsymbol{B} = \boldsymbol{B_a} + \boldsymbol{B_1} e^{i\omega t} + \lambda_m \boldsymbol{m} \tag{1.6}$$

Here, $\mathbf{B_1}$ is the applied RF field with frequency ω, and λ_m is the molecular field parameter, the effective hyperfine interaction constant that determines the hyperfine interaction field $\mathbf{B_{hf}}$. The magnetic anisotropy field $\mathbf{B_a}$ acting on electron spins makes it possible to effectively describe their collective behavior depending on the crystal structure of the material. Accordingly, in ferromagnetic crystals with an anisotropic crystal structure (for example, those with hexagonal symmetry) there are axes of easy and hard magnetization, which leads to preferential alignment of the electronic magnetization along the easy axis in the absence of external magnetic fields.

The solution of a differential equation with a harmonic right-hand side is also a harmonic function, that is, the magnetizations **m** and **M** can be represented as $\mathbf{m}(0)e^{i\omega t}$ and $\mathbf{M}(0)e^{i\omega t}$. Then the solution of the system of Bloch equations for the transverse magnetization components in the absence of an external RF field and neglecting the relaxation terms, gives the eigenfrequencies Ω_N and Ω_e of nuclear magnetic resonance and electronic ferromagnetic resonance, respectively:

$$\Omega_N = \left|\gamma_N B_{hf}\left(1 - \frac{B_{hf}}{B_a}\frac{m}{M}\right)\right| \approx \left|\gamma_N B_{hf}\right| \tag{1.7}$$

$$\Omega_e = \left|\gamma_e B_a\left(1 + \frac{B_{hf}}{B_a}\frac{m}{M}\right)\right| \approx \left|\gamma_e B_a\right| \tag{1.8}$$

where m and M are the equilibrium values of the magnetizations. Thus, in the first approximation, the NMR frequency in a ferromagnet is determined by the Zeeman interaction of nuclear spins with the molecular field generated by the electron subsystem. The small correction to the NMR frequency is called a dynamic frequency shift, but it appears only at very low temperatures due to the fact that the nuclear magnetization has a 1/T dependence [5]–[7].

Thus, the solution of the Bloch equations in the absence of an external RF magnetic field makes it possible to determine the eigenfrequencies for the oscillations in this interconnected system. To characterize the response of this system to an external RF irradiation at frequencies close to Ω_N (since only the case of NMR is of interest here), it is necessary to return to the Bloch equations in presence of the RF field $\mathbf{B_1}$. This approach will allow determining the total magnetic susceptibility of the bound system of nuclei and electrons in the plane orthogonal to the anisotropy magnetic field $\mathbf{B_a}$, since it is the magnetization in this plane that is responsible for the intensity of the signal in NMR. As a result,

after some simplifications, the following nuclear (χ_N) and electronic (χ_e) components of the transverse magnetic susceptibility can be obtained:

$$\chi_N = -\mu_0(1+\eta)\frac{\gamma_N m}{\omega - \Omega_N} \tag{1.9}$$

$$\chi_e = \chi_0 - \mu_0\eta(1+\eta)\frac{\gamma_N m}{\omega - \Omega_N} \tag{1.10}$$

where μ_0 is the magnetic permeability of the vacuum, and χ_0 is the static susceptibility of the electronic subsystem, and η is the so-called enhancement factor:

$$\eta = \frac{B_{hf}}{B_a} \tag{1.11}$$

The concept of the enhancement of magnetic susceptibility in ferromagnets is one of the key features of Internal Field NMR. The origins of this enhancement in both the magnetic domains and domain walls will be discussed below.

The static susceptibility χ_0 does not depend on the frequency of the RF radiation and, therefore, does not contribute to resonant absorption:

$$\chi_0 = \mu_0\frac{M}{B_a} \tag{1.12}$$

In both components of the magnetic susceptibility, a resonant character is observed when the RF radiation frequency approaches the NMR eigenfrequency, that is, both the nuclear subsystem and the electron subsystem contribute to the NMR signal. Moreover, it can be seen that both contributions to the magnetic susceptibility also depend on the enhancement factor, the value of which lies in the range of 10-100 depending on the material under study. Interestingly, while the nuclear susceptibility has a dependence ~η, the electronic component is enhanced as η^2, and thus, the dominant interaction of RF radiation at the NMR frequency occurs with the electronic subsystem rather than with the nuclear subsystem.

Finally, in order to determine what power the interconnected system of nuclei and electrons absorbs at frequencies close to Ω_N, it is necessary to return to the relaxation components of the Bloch equations. Phenomenologically, the magnetizations **m** and **M** undergo relaxation to equilibrium with an exponential time dependence. From the mathematical viewpoint, the same effect can be achieved by substituting the purely real value of the resonant frequency with a complex value, whose imaginary part Γ accounts for the relaxation term of the time-dependent magnetization:

$$\Omega_N^* = \gamma_N B_{hf} + i\Gamma \tag{1.13}$$

By inserting this complex frequency into Equations (1.9) and (1.10) we obtain the total magnetic susceptibility of a ferromagnetic material in the form of its real and imaginary parts χ' and χ" as [8]:

$$\chi'(\omega) = \chi_e + (1+\eta)^2 \frac{\omega - \Omega_N}{(\omega - \Omega_N)^2 + \Gamma^2} \gamma_N m \mu_0 \tag{1.14}$$
$$\chi''(\omega) = (1+\eta)^2 \frac{\Gamma}{(\omega - \Omega_N)^2 + \Gamma^2} \gamma_N m \mu_0$$

Here, only the imaginary part χ" is of interest to us since according to the fluctuation-dissipation theorem it determines the power of the absorbed radiation P:

$$P = \omega\chi''(\omega) B_1^2 \propto \omega(1+\eta)^2 B_1^2 \approx \omega(\eta B_1)^2 \tag{1.15}$$

The same general relation remains true for any system with a complex susceptibility χ including diamagnetic materials studied with conventional NMR with only difference being the absence of any enhancement of the RF magnetic field:

$$P\,(diamagnetic) = \omega\chi''(\omega) B_1^2 \propto \omega(B_1)^2 \tag{1.16}$$

Thus, we can see that the power absorbed by a ferromagnetic material is enhanced by a factor of η^2 compared to a non-magnetic substance, or, equivalently, the nuclear spins "feel" an alternating magnetic field that is η times stronger that the applied one. The effect of the external magnetic field amplification can be demonstrated visually with the simple vector model shown in Figure 2.1.

Let us assume that there is a ferromagnetic substance with a single axis of easy magnetization in the absence of an external magnetic field. In the fully relaxed state, the electron magnetization **M** is directed along the magnetic anisotropy field $\mathbf{B_a}$. At the same time, the electronic moments that make up this magnetization generate the hyperfine interaction field $\mathbf{B_{hf}}$, which acts on the nuclear spins. When the external RF magnetic field $\mathbf{B_1}$ is applied in a plane orthogonal to the easy magnetization axis, the electron magnetization **M** quickly (electron relaxation scale is much shorter compared to nuclei) aligns along the total magnetic field $\mathbf{B_a} + \mathbf{B_1}$, forcing the hyperfine interaction field to turn. Thus, in addition to the orthogonal field $\mathbf{B_1}$, the nuclear subsystem is affected by the orthogonal component of the hyperfine field $\mathbf{B_{hf}}^{\perp}$, which is several orders of magnitude larger than the applied field $\mathbf{B_1}$ itself:

$$B_{hf}^{\perp} \approx B_{hf} \frac{B_1}{|\boldsymbol{B_a} + \boldsymbol{B_1}|} \approx \frac{B_{hf}}{B_a} B_1 = \eta B_1 \gg B_1 \tag{1.17}$$

In such a simplified approach, the same enhancement factor η arises as in the Bloch equations, which shows how many times the part of the hyperfine field acting on nuclear spins exceeds the applied RF field $\mathbf{B_1}$. It is important to note that the enhancement factor is a characteristic of the material under study and does not depend on the applied RF field (however the application of a constant external magnetic field reduces this coefficient [4]).

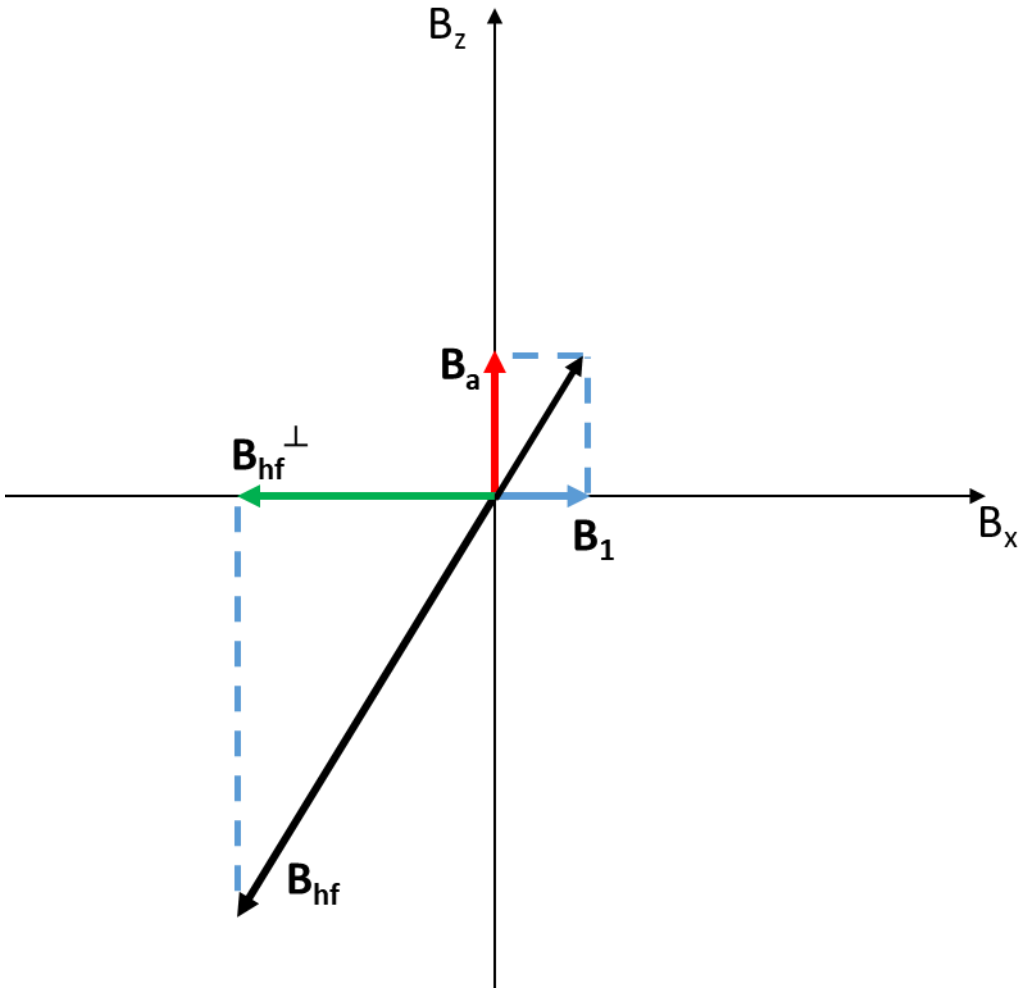

Fig. 1.1. A schematic representation of the vector model for the magnetic field enhancement inside a ferromagnetic material.

1.1.2 Domain structure. Domain walls. Demagnetizing field.

It should be noted that in the above calculations, only the regions in which the entire electronic magnetization is homogeneous were considered – the magnetic domains. Magnetic domains cannot be arbitrarily large, since a domain is essentially a magnetic dipole and generates an external (demagnetizing) magnetic field. When the energy of this magnetic field reaches a certain critical value with an increase in the domain, it becomes energetically favorable to split this domain into several

domains with magnetizations directed in such a way that the magnetic field generated by this system decreases, and in the limiting case it becomes completely zeroed out (Figure 1.2).

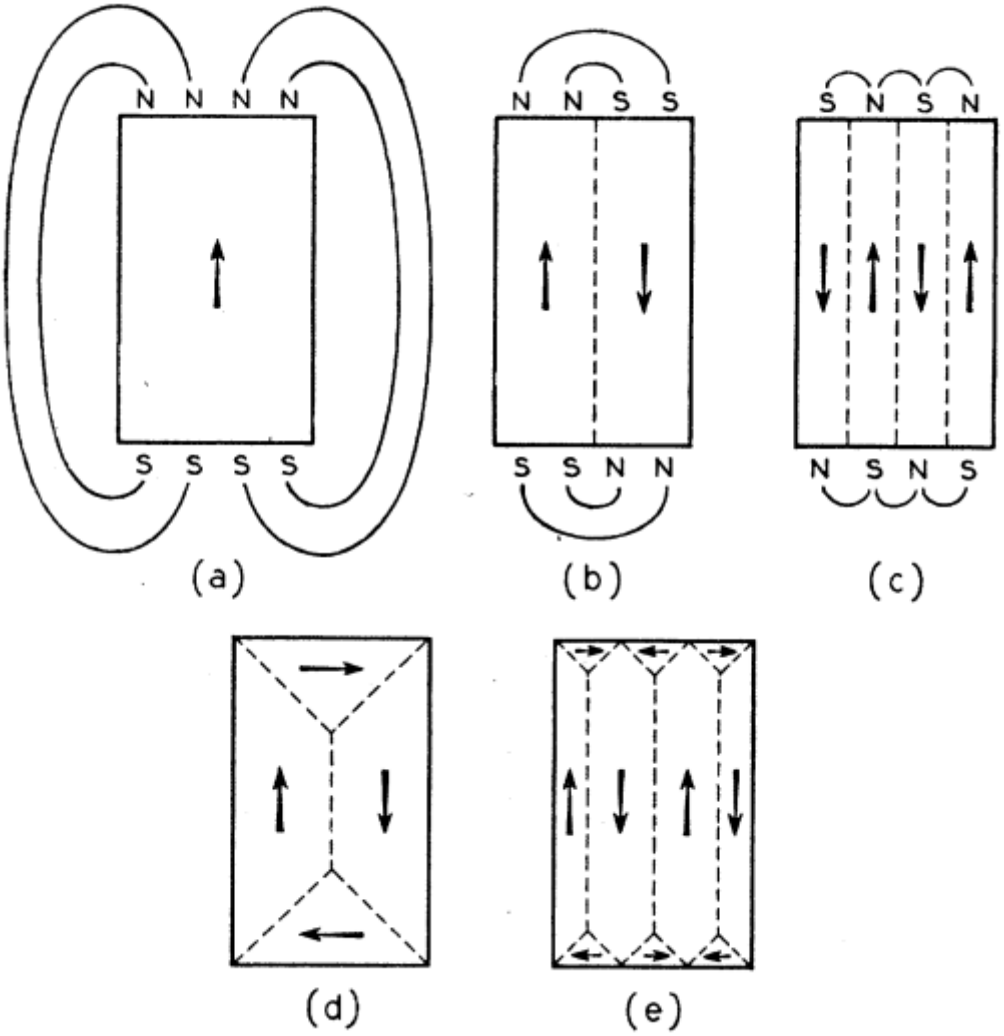

Fig. 1.2. Origin of magnetic domains. When one domain (a) is divided into several smaller domains with opposite magnetizations (b, c), the demagnetizing field generated by the particle decreases. In the event of a so-called closure domains (d, e), this field disappears. The conditions for the appearance of several domains, as well as the type of division into domains, depend on the crystal structure and morphology of the particles. The figure is taken from review [9].

The critical size at which the existence of a single domain becomes energetically unfavorable depends primarily on the substance under study, as well as on the crystal structure and morphology of its particles. In the case of metallic cobalt that is mainly considered in this manuscript, the critical size of a single-domain spherical particle is estimated as 70 nm, and can be much larger if the particle shape is strongly anisotropic [10].

Due to the presence of an exchange interaction, which leads to alignment of the electronic magnetic moments, an abrupt boundary between the domains with different magnetization directions is impossible, since the formation energy of such a transition would be much greater than the energy of the demagnetizing field. Instead, there are regions between the domains in which the magnetization changes its direction smoothly – the domain walls. It is the balance between the energy of the exchange interaction (the magnetic moments of electrons tend to line up in parallel), the energy of the magnetocrystalline anisotropy (the magnetic moments tend to line up along a certain axis of easy magnetization), and the energy of the demagnetizing field, that determines the conditions for the emergence of magnetic domains. Usually, two models of domain walls are considered (for convenience, we consider the boundary between domains with strictly antiparallel magnetizations): with a rotation of the magnetization in a plane parallel to the plane separating the domains - the Bloch model; with a rotation of the magnetization in the plane orthogonal to the boundary between the domains – the Neel model. These models are depicted in Figure 1.3.

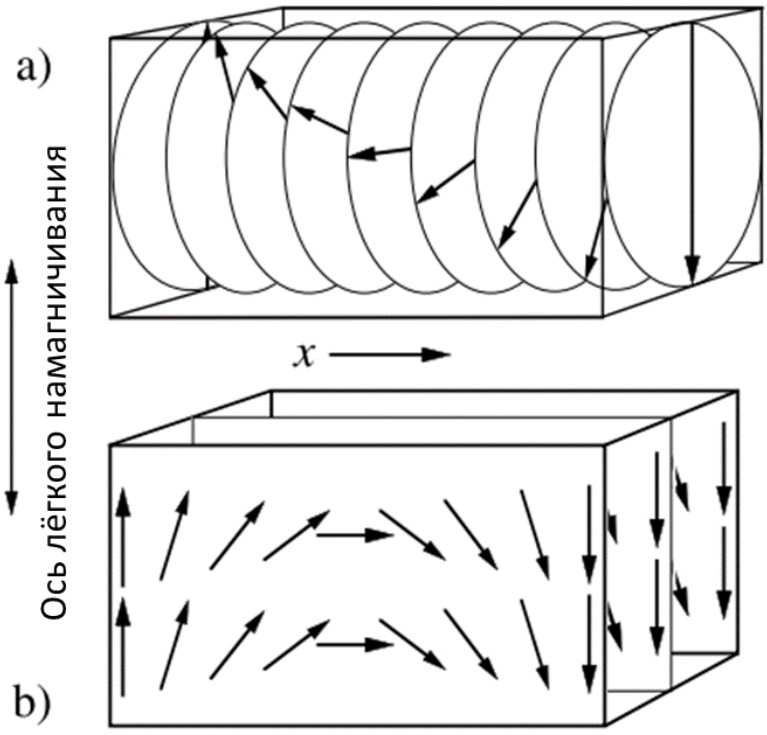

Fig. 1.3. Different models of walls between two domains with a 180° relative rotation. The Bloch model (a) shows the optimal way to rotate the magnetization, while the Neel model (b) is less energetically favorable, but can be found in thin films. Figure is adapted from review [11].

In the absence of an external magnetic field, a multidomain ferromagnetic particle tends to have zero overall magnetization, thereby minimizing the energy of the demagnetizing field. Under the influence of an external magnetic field, a ferromagnet acquires a total magnetization directed along the applied magnetic field. Magnetization can arise either due to the rotation of the magnetizations of individual domains in the direction of the external field (through the direct interaction between the magnetic moment and magnetic field), or due to the growth of domains whose magnetization was directed in this direction at the expense of other domains. The latter mechanism is considered to be more energetically favorable, especially in materials with high magnetic anisotropy [9]. For clarity, let's illustrate it with a simple example of a particle consisting of two antiparallel domains, which was placed in a magnetic field parallel to one of the domains (Figure 1.4).

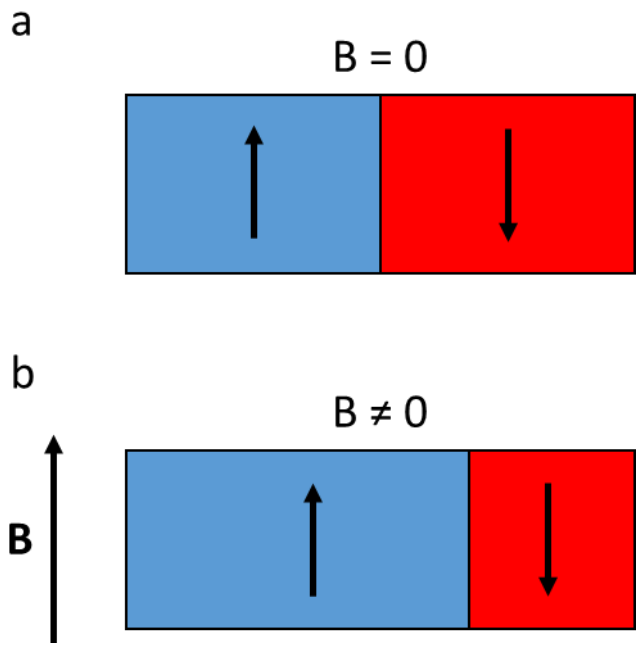

Fig. 1.4. A simple depiction of the magnetization mechanism in a two-domain ferromagnetic particle. In the absence of magnetic field (a), the domain wall is located in such a way that the demagnetizing fields of the domains compensate each other. In the presence of an external magnetic field **B**(b), the domain wall shifts in such a way that the total magnetization of the particle is directed along the magnetic field.

The growth of one of the domains results in a motion of its domain walls and this motion has a strong effect when an external RF field is applied as when during an NMR experiment. While the deviation of the magnetization from the equilibrium state under the action of the RF field is relatively small inside the domain, the displacement of the domain wall causes the deviation of the magnetization

by an arbitrary angle up to 180°. In this case, the transverse magnetic field acting on the nuclear moments can reach the value of $\mathbf{B_{hf}}$ itself:

$$B_{hf}^{\perp}(d.w.) \propto B_{hf} \tag{1.18}$$

Thus, if we apply the definition of the enhancement factor (the ratio between the transverse magnetic field acting on the nucleus and the applied RF magnetic field) to the case of domain walls, we obtain a much higher value compared to the magnetic domains:

$$\eta\,(domain\,walls) = \frac{B_{hf}^{\perp}}{B_1} \approx \frac{B_{hf}}{B_1} \gg \frac{B_{hf}}{B_a} = \eta\,(domains) \tag{1.19}$$

This effect can be illustrated in the same way on a simple two-domain particle (Figure 1.5).

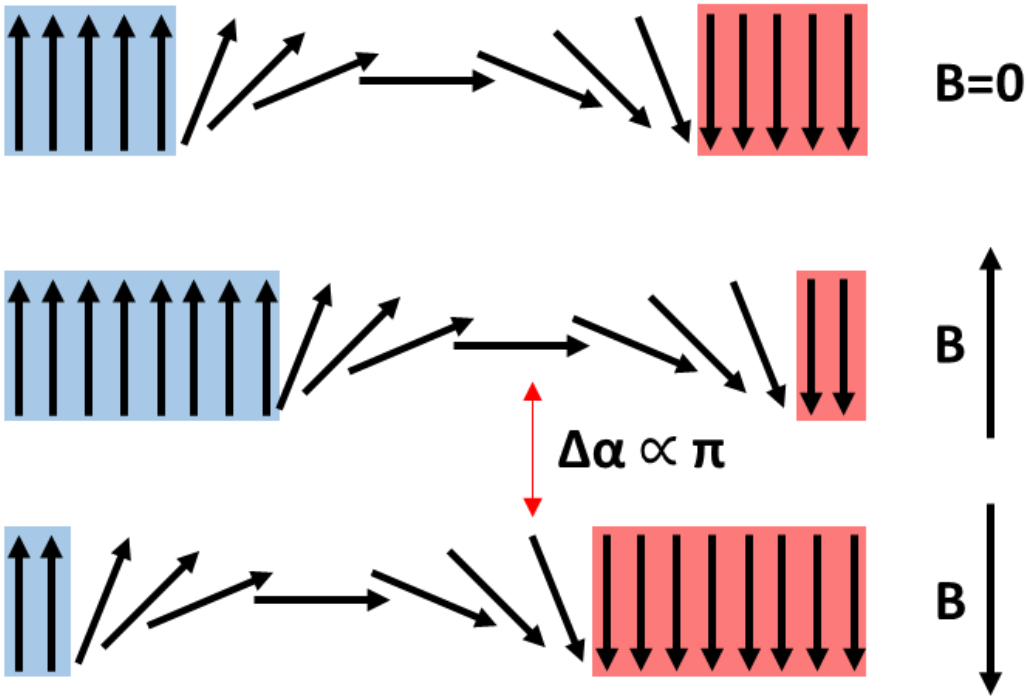

Fig. 1.5. Illustration of the electronic magnetic moment rotation during the domain wall motion in a two-domain particle. It can be seen that the deviation of the electronic magnetic moment (and with it the local magnetic field) in this case can no longer be considered small compared to the case of the magnetic domain.

In an NMR experiment, the application of the external radio-frequency magnetic field causes a periodic motion of the domain walls and thus significant oscillations of the local electron field at the

RF frequency, which leads to the absorption of radio-frequency radiation, the power of which can be written using Equation (1.15). In this case, we only need to replace the enhancement factor η of the domains by the enhancement factor of the domain walls, which, according to experimental data, ranges within (1-2)*10^3 in the case of metallic cobalt [3]. In the same work, the authors estimate theoretically the value of the domain walls enhancement factor based on the geometric and magnetic parameters of the domain wall as:

$$\eta \cong \frac{\pi D H_{hf}}{NM\delta} \tag{1.20}$$

where D is the characteristic size of the domain; H_{hf} is the hyperfine field; N is the demagnetizing factor, a dimensionless coefficient that connects the demagnetizing field and the magnetization of the particle and depends solely on its shape; M is the equilibrium electron magnetization, and δ is the thickness of the domain wall. The authors obtained a value close to the experimental one, but in practice, it is difficult to use this formula because the geometric parameters D and δ are hard to estimate in each individual case.

Based on the molecular field theory, it is thus possible in first approximation to determine the dependence of the NMR frequency in ferromagnetic materials on the hyperfine field, and to obtain the dependence of the absorbed power of radio frequency radiation on the enhancement factor - two main theoretical differences between NMR in ferromagnets and classical NMR. Next, one should consider how this understanding can be applied to performing Internal Field NMR experiments, particularly on ^{59}Co nuclei, using modern pulsed Fourier spectrometers.

1.2 Application of the Internal Field NMR spectroscopy technique for ^{59}Co nuclei

The main question related to the practical application of ^{59}Co Internal Field NMR spectroscopy is which information about ferromagnetic samples can be obtained using this method. The frequency of nuclear magnetic resonance in a ferromagnet depends, among other possible contributions, on the hyperfine interaction field experienced by the nucleus. Thus, the NMR frequency recorded in the experiment will reflect the magnitude of the hyperfine field (or its distribution) inside the sample. Therefore, it is important to understand what contributions exist in the hyperfine field and how they are related to the structure of the sample under study. Moreover, in addition to the hyperfine field, the nuclear magnetic moments are also affected by the demagnetizing field generated by the magnetization of the particle, if it has magnetic poles (i.e., in the absence of an external magnetic field, the demagnetizing field is present only in single-domain particles).

1.2.1 Demagnetizing field. Structure of hyperfine field

The resulting magnetic field experienced by the nuclear magnetic moments can be divided into contributions from the hyperfine and the demagnetizing fields:

$$\boldsymbol{B_{total} = B_{dem} + B_{hf}} \tag{1.21}$$

The magnitude of the demagnetizing field can be derived from the classical electrodynamics problem of finding the distribution of the B and H fields for a spherical uniformly magnetized particle (Figure 1.6, [12]). As a result, it turns out that the magnetic field strength $\mathbf{H_i}$ inside the spherical particle is always directed against the magnetization and is equal to:

$$\boldsymbol{H_i = -\frac{4\pi}{3} M = H_{dem} = \frac{B_{dem}}{\mu_0}} \tag{1.22}$$

In the case of a particle with an arbitrary shape, the demagnetizing field is anisotropic and given by:

$$\boldsymbol{B_{dem} = -N_d M} \tag{1.23}$$

where N_d is the so-called demagnetizing factor, which depends solely on the geometry of the particle. As mentioned above, the demagnetizing factor for a perfect sphere is $4\pi/3$, for an infinite cylinder in the transverse direction it is 2π, for an infinite plane it is 4π.

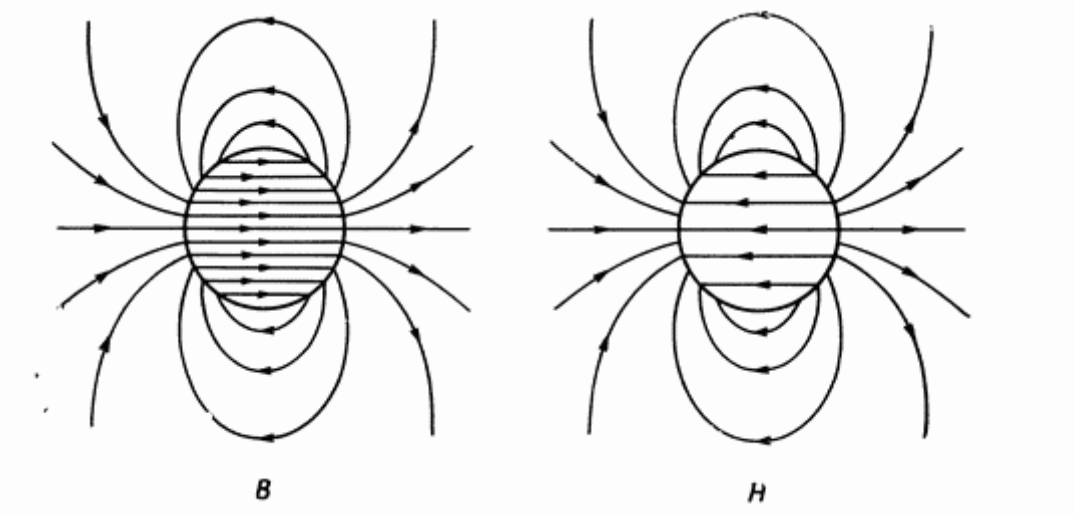

Fig. 1.6. Distribution of B- and H-fields inside a uniformly magnetized spherical particle. The magnetic induction **B** inside the particle is parallel to the magnetization, while the magnetic field strength **H** is antiparallel to the magnetization.

For bulk metallic cobalt, the empirical saturation magnetization M is 1446 G, which leads to a theoretical contribution of the demagnetizing field for a spherical particle of about 6 kG.

Several different contributions can be distinguished in the hyperfine interaction field (interaction of the nuclear magnetic moment with electrons inside one ion), which was previously written as $\lambda_m \mathbf{M}$ in the molecular field approximation (Equation 1.5) [13], [14]:

$$\boldsymbol{B_{hf}} = \boldsymbol{B_{hf,dip}} + \boldsymbol{B_{hf,orb}} + \boldsymbol{B_{hf,con}} \tag{1.24}$$

where $\mathbf{B_{hf,dip}}$ is the contribution due to the dipole interaction of the nuclear spin with 3d-electrons (equal to zero for cubic symmetry); $\mathbf{B_{hf,orb}}$ is the contribution from all unquenched orbital momenta of electrons; $\mathbf{B_{hf,con}}$ is the Fermi contact interaction – an interaction between the nuclear spin and electron dipole magnetic moment, which is present only for s-electrons. The first two contributions are anisotropic, while the Fermi contact interaction is isotropic and can additionally be separated into contributions from different shells of s-electrons. The s-electrons of the inner shells of an atom interact with its remaining electrons, which means their polarization by d-electrons is taken into account; conduction s-electrons can be polarized both by the electron shell of the atom, and by the interaction with the moments of the nearest neighbors of the atom. The latter contribution is very important, since the presence of other atoms in the local environment of the cobalt atom (for example, in the case of solid solutions, alloys, or intermetallic compounds) can significantly change the local field acting on the nuclear magnetic moment.

A detailed consideration of the structure of the hyperfine interaction field $\mathbf{B_{hf}}$ was carried out in pioneering works [1], [14] together with an estimate of magnitudes of various contributions. Without giving detailed formulas for all these interactions, it should be noted that the hyperfine field induction from the Fermi contact interaction $\mathbf{B_{hf,con}}$ makes the largest contribution and amounts to about 200 kG. In addition, the resulting hyperfine interaction field is directed antiparallel to the magnetic moment (i.e., λ_m has a negative sign).

As shown above, the presence of the enhancement factor is an important difference between the ^{59}Co Internal Field NMR technique and classical NMR, and it can vary significantly depending on the domain structure, on the hyperfine interaction fields and on crystal anisotropy. Moreover, in the vast majority of cases, the enhancement factor is an unknown quantity. In such a situation, extracting quantitative information from NMR spectra in the internal field of a sample is a non-trivial task. To take into the account the enhancement factor, Panissod et al. [15] have introduced a technique that includes sweeping over the RF magnetic field amplitude (or, equivalently, over the power of the RF

radiation). In order to better understand the necessity of this approach, we must first consider the implementation of spin echo sequences in ferromagnetic materials.

1.2.2 Spin echo in ferromagnetic materials

In modern NMR spectroscopy, spectra are recorded by the Fourier transform of the so-called free induction decay (FID) signal obtained in time domain. FID occurs immediately after a radio-frequency field pulse at a frequency close to the Larmor frequency is applied to a system of nuclear spins in a magnetic field. Due to the inhomogeneities of the magnetic field, the orthogonal magnetization of an ensemble of nuclei tends to dephase. Unlike the true loss of the transverse magnetization (caused by spin-spin relaxation originating from random processes such as magnetic field fluctuations), this loss due to the static magnetic field inhomogeneities is reversible. Thus, instead of a single pulse deflecting the sample magnetization into a plane orthogonal to the external constant magnetic field, spin echo sequences are used, which make it possible to refocus the magnetization in the orthogonal plane. In the case of solids, where the strong direct dipole interaction between the spins is not averaged to zero by fast molecular motions, this interaction becomes an additional source of spin dephasing. Another type of spin dephasing takes place when the nuclear spin is larger than ½ i. e. when it has an electric quadrupole moment. While the origins of these types of dephasing are quite different, they are somewhat similar to the case of inhomogeneous magnetic field in a sense that their nature is not random and thus a refocusing of the magnetization with some kind of spin manipulation is possible in each case. In fact, a sequence similar to Hahn echo sequence ($\pi/2 - \tau - \pi$) can be used both for direct dipole and quadrupole interaction refocusing, which is called a solid (or quadrupole) echo sequence [16]:

$$\theta - \tau - \theta - \tau - I(t) \tag{1.25}$$

where θ is the angle of deflection of the magnetization from the equilibrium state into the orthogonal plane, τ is the delay between pulses. The recording of the spectrum intensity *I(t)* begins after the 2τ period after the first pulse. In the case of spin ½ (for simplicity), the magnetization deflection angle θ under the action of the RF field with amplitude B_1 during the time t_1 is:

$$\theta = \gamma_N B_1 t_1 \tag{1.26}$$

As shown by Hahn, who was the first to study and describe mathematically solid-state echo, the echo intensity at time 2τ (echo maximum) is [17]:

$$I(2\tau) = I_0 \sin(\gamma_N B_1 t_1) sin^2\left(\frac{\gamma_N B_1 t_1}{2}\right) e^{-2\tau/T_2} \tag{1.27}$$

where T_2 is the transverse relaxation time.

These considerations apply strictly only to diamagnetic materials. However, as shown above, as a first approximation, the case of a ferromagnet can be treated by replacing:

$$B_1 \rightarrow \eta B_1 \tag{1.28}$$

However, on further analysis, the intensity of a solid-state echo in a ferromagnet has a much more complex dependence compared to diamagnetic materials. The main difference is that in the case of classical NMR, the magnetization of the sample in equilibrium is aligned along the external magnetic field (laboratory Z axis) and is irradiated by the RF field in the orthogonal XY plane. In the case of a ferromagnet, the equilibrium magnetization is aligned along the magnetic anisotropy field, which, in the case of an ideal polycrystalline sample, leads to the fact that the equilibrium magnetizations of the particles in the sample have equiprobable directions with respect to laboratory coordinates. It was shown that the experimental dependence of the intensity of the spin echo of a polycrystalline ferromagnetic material on the RF pulse amplitude has a lognormal distribution [18]:

$$I(B_1, \omega) = \eta I_0(\omega) \exp\left(\frac{-log^2\left(B_1 / B_{opt}\right)}{2\sigma^2}\right) \tag{1.29}$$

where $I_0(\omega)$ is the "true" (directly proportional to the amount of nuclei resonating at frequency ω) signal intensity, B_{opt} is the RF field amplitude at which the observed intensity $I(B_1, \omega)$ takes on a maximum value, and σ is the distribution width. In addition, several lognormal modes can occur in this distribution if several types of particles contribute to the signal at this frequency.

Another feature of the NMR spectra of ferromagnetic cobalt compounds is their large width in the frequency range. The maximum frequency sweep width of most modern pulsed NMR spectrometers is 1-2 MHz, which is quite sufficient for recording the spectra of diamagnetic non-conductive compounds and most conductive compounds or compounds with paramagnetic sites. The ^{59}Co NMR spectra of ferromagnetic compounds are usually extended in the 40 MHz range between 200 and 240 MHz, and in the case of alloys or intermetallic compounds, this range can reach 200 MHz. Thus, the ^{59}Co Internal Field NMR are usually recorded in a stepwise fashion with a 0.5-1 MHz change in the carrier frequency at each step.

The lognormal dependence of the intensity of the spin echo in ferromagnets, as well as the large width of the spectra, determine the procedure for recording ^{59}Co Internal Field NMR spectra introduced by Panissod [19]. When recording the intensity of the spectrum at each step along the carrier

frequency, a sweep is also performed in terms of the power of the RF field (which has a quadratic dependence on the amplitude). As mentioned above, the amplitude of the RF field, at which the maximum intensity is reached, is called optimal. At this amplitude, the exponential term in the expression for the intensity of the spectrum becomes unity. In order to obtain the "real" intensity from the observed intensity, it remains to account for the unknown amplification factor. It can be determined from the previously obtained optimal magnetic field, since the field $B_{hf}^{\perp}$ "felt" by the nuclei is η times stronger than the experimentally controlled RF field B_{opt}. Thus, from this two-dimensional experiment, the dependence of the optimal field (enhancement factor) on frequency and the "real" intensity of the NMR spectrum are extracted:

$$I_0(\omega) = \frac{1}{\eta} I\left(B_{opt}, \omega\right) = \frac{B_{opt}}{B_{hf}^{\perp}} I\left(B_{opt}, \omega\right) \tag{1.30}$$

in turn, it is known that the maximum intensity of the spin echo is achieved when the angle of rotation of the nuclear magnetization is π/2, and thus, under the same experimental conditions at each carrier frequency, the field $B_{hf}^{\perp}$ is a constant determined by the experimental conditions:

$$\theta = {}^{\pi}/_{2} = \gamma B_{hf}^{\perp} t \;\rightarrow\; B_{hf}^{\perp} = const \tag{1.31}$$

To summarize the practical consequences of the above considerations, ^{59}Co NMR spin echo experiments performed in the internal field of a sample make it possible to obtain quantitative information about the crystal and magnetic structure of the particles that make up the sample. The magnitude of the local field (directly related to the resonant frequency in the NMR experiment) acting on the nuclear magnetic moment of cobalt depends on several factors, and is primarily determined by the Fermi contact interaction, which sets the base value of about 200 kG. Anisotropic contributions to the hyperfine field make it possible to separate fcc and hcp packing due to large anisotropic contributions in the case of the latter. In the case of the presence of guest atoms in the nearest environment of the cobalt atom, the value of the local Fermi-contact component changes, which makes it possible to study the structure of alloys, solid solutions, and intermetallic compounds. Finally, if a particle is so small that division into magnetic domains becomes energetically unfavorable, it generates its own demagnetizing magnetic field, which leads to a shift in the resonant frequency for single-domain particles. Another important effect, called superparamagnetism, is observed with a further decrease in the size of single-domain particles, when the phenomenon of nuclear magnetic resonance in the internal field of a ferromagnet is not observed at all.

1.2.3 Magnetic anisotropy energy and superparamagnetism

As mentioned above, there are directions along which the orientation of the magnetization in ferromagnetic crystals is energetically favored - the easy magnetization axes. Such behavior is based on the magnetic anisotropy, the sources of which are discussed in detail, for example, in the book [20]. The main contribution to the magnetic anisotropy is the magnetocrystalline anisotropy due to the spin-orbit interaction of electrons. Due to this contribution, the magnetic moments of electrons tend to line up along the easy magnetization axes (there may be several of them). In the simplest case of uniaxial anisotropy, one can introduce the dependence of the magnetic anisotropy energy on the angle between the magnetization and the easy magnetization axis θ:

$$E = V(K_1 sin^2(\theta) + K_2 sin^4(\theta) + \cdots) \quad (1.32)$$

where V is the particle volume and K_i are the magnetic anisotropy constants. Often this expansion is considered up to the term K_2, or even only taking into account the term with constant K_1. hcp cobalt is an important example of an uniaxial magnetic. It has a sixth-order symmetry axis, which is the easy magnetization axis. The value of VK_1 is essentially an energy barrier for the magnetization flip from the state parallel to the easy magnetization axis to the antiparallel state. For the more isotropic cubic structures (such as fcc packing of cobalt), which have a larger number of magnetization axes, the dependence of the magnetic anisotropy energy takes on a much more complex form.

Another contribution to the total magnetic anisotropy comes from the shape anisotropy due to the presence of a demagnetizing field. For a spherical particle, this anisotropy will be obviously equal to zero, while for a strongly elongated particle the magnetization directed along the elongated axis of the particle will create a weaker demagnetizing field compared to the transverse directions [21], [22].

There are other sources of magnetic anisotropy, but they should be considered only in more specific cases. Usually, the effect of magnetic anisotropy in a particle is expressed as some effective energy barrier that must be overcome in order to change the direction of particle magnetization:

$$E = K_{Eff} V \quad (1.33)$$

The presence of such a barrier determines the stability of the magnetization of a ferromagnetic particle, which can persist for a very long time.

However, often such a barrier is not insurmountable, and moreover, the magnetization of a particle can change due to thermal fluctuations. The simplest model of such fluctuations was proposed in the form of the Arrhenius dependence by Neel [23]:

$$\tau = \tau_0 exp\left(\frac{K_{Eff}V}{k_BT}\right) \quad (1.34)$$

where τ is the time between temperature jumps of the magnetization, τ_0 is the characteristic time of magnetization relaxation. τ_0 is not fully known but usually considered to be in the range of 10^{-10}-10^{-12} s. The presence of such fluctuations affects the recording of NMR spectra (as well as other magnetic resonance and magnetic methods).

A ferromagnetic particle will contribute to the ^{59}Co NMR signal only if its magnetization is maintained during the experiment. Otherwise, the signal from a particle undergoing fast random jumps in magnetization will be time-averaged to zero - the particle will become superparamagnetic. This leads to the fact that all particles of the sample can be divided into observable and unobservable at a given temperature, and the critical volume between observable and unobservable particles can be derived from Equation (1.34):

$$V_{crit} = \frac{k_BT}{K_{Eff}} \ln\left(\tau_m/\tau_0\right) \quad (1.35)$$

where the effective magnetic anisotropy constant K_{Eff} is often taken for evaluation as $5*10^6$ erg*cm^{-3} [24], and the characteristic time τ_0 in the case of the NMR experiment is about 20 μs (this duration includes two echo pulses, two echo delays and the signal recording period). In the same way, from Eq. (1.33), one can determine the temperature at which a particle of a given volume will pass from a superparamagnetic to a ferromagnetic state - the so-called blocking temperature T_B:

$$T_B = \frac{VK_{Eff}}{k_B \ln\left(\tau_m/\tau_0\right)} \quad (1.36)$$

The use of the critical volume in this case seems to be more convenient, since the constant K_{Eff} itself depends on the temperature [25], [26]. The behavior of the constant τ_0 with temperature has not been studied in great detail, but it has been shown that it varies with temperature [27]. In practice, the critical linear particle size (diameter of a spherical particle of equivalent volume) is about 10 nm at temperatures of about 77 K [24] in ^{59}Co Internal Field NMR. In the case of studying ferromagnet-superparamagnet transitions, it is always important to take into account the experimental method by which particles are studied and the effect of thermal fluctuations in each specific case. For example, in the case of ferromagnetic resonance spectroscopy, the measurement time is significantly reduced, and the signal from superparamagnetic particles does not disappear, but, on the contrary, is significantly narrowed and enhanced.

In conclusion, theoretically, in the ^{59}Co Internal Field NMR experiments, one can obtain information about the crystal structure of the particles that constitute the sample, as well as information about their magnetic structure (single- or multi-domain) from the value of the resonant frequency. The dependence of the enhancement factor, obtained in a natural way when conducting an experiment with sweeps both in frequency and in amplitude of the RF field, also contains information about the magnetic structure of the sample particles. Finally, the effect of blocking particles into a ferromagnetic state from a superparamagnetic one can help determine the sizes of the particles that contribute to the signal intensity at different temperatures. In the next section, we consider how these dependences and effects were observed in real experimental ^{59}Co Internal Field NMR spectra.

1.3 Experimental observations of the ^{59}Co Internal Field nuclear magnetic resonance

1.3.1 Metallic cobalt

The NMR spectrum on ^{59}Co nuclei in the internal field of the sample was first observed by Gossard and Portis in 1959 [2]. The spectrum was obtained at room temperature for relatively large (5-10 μm in diameter) particles of metallic cobalt with fcc packing. The spectrum was a single line with a width at half maximum of about 0.5 MHz, centered at a frequency of 213.1 MHz (Figure 1.7). This observation made it possible to obtain the first experimental estimate of the local magnetic field at the location of the cobalt nucleus B_{loc} = 213400 G, which quite accurately coincided with the theoretical predictions published by Marshall a year earlier [1].

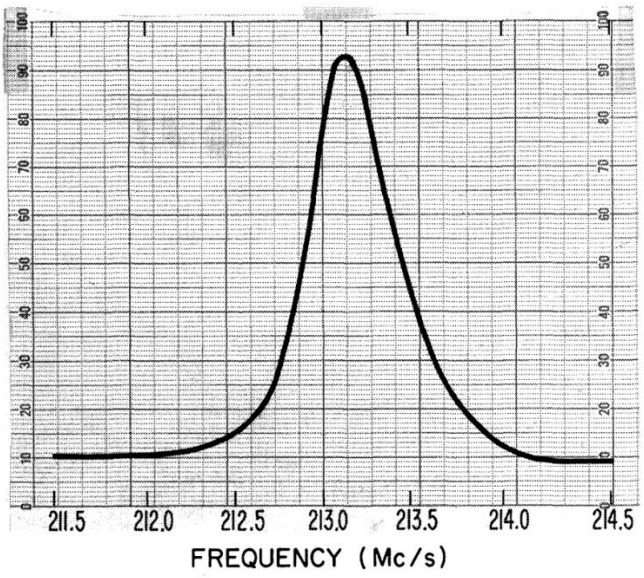

Fig. 1.7. The first ^{59}Co Internal Field NMR spectrum recorded for the cobalt particles with fcc crystal packing. Figure adapted from [2].

Since the size of the studied particles far exceeded the limit of division into domains indicated above (about 70 nm), the signal at 213.1 MHz was attributed to multidomain particles of fcc cobalt, and the main contribution to this signal is made by domain walls due to their large enhancement factor [28]–[34].

Gossard and Portis were also the first to study the temperature dependence of the resonant frequency of the multidomain fcc Co particles signal [3]. As the temperature decreased, the resonant frequency increased with a temperature dependence that approximately coincided with the behavior of the spontaneous magnetization derived by Stoner [35]:

$$\nu(T) = \nu(0)\sqrt{\left(1 - \left(\frac{T}{\theta}\right)^2\right)} \tag{1.37}$$

where θ is the Curie temperature (1400 K for cobalt) and ν(0) = 217.2 MHz is the resonant frequency extrapolated to absolute zero temperature, which in the work of Gossard and Portis gave the best fit to the experimental curve.

In [34], Andreev showed that the above dependence works only at temperatures well below the Curie temperature. At higher temperatures, the behavior of the resonant frequency is much more accurately described in the theory of spin waves [36]:

$$\frac{\nu(0) - \nu(T)}{\nu(0)} = a_{3/2}\left(\frac{T}{\theta}\right)^{3/2} + a_{5/2}\left(\frac{T}{\theta}\right)^{5/2} + \cdots \tag{1.38}$$

which in the first approximation at low temperatures provides the Bloch's law [37].

The signal from the hcp crystal packing of metallic cobalt was first observed in 1960 [38]. At room temperature, the frequency of this resonance was about 221.5 MHz, and the frequency at zero temperature was estimated at 228 MHz. Upon further study of particles of metallic cobalt with hcp packing, a second peak at 214 MHz was found in the spectrum (Fig. 1.8) [39]. The authors showed that the presence of two signals in the spectrum of hcp cobalt is caused by a significant magnetic anisotropy. In this case, the signal at 221.5 MHz is associated with Co atoms located in the center of the domain wall (the electronic magnetization is perpendicular to the easy magnetization axis), and the signal at 214 MHz is caused by atoms at the edge of the domain wall (the magnetization is directed along the easy magnetization axis). These two lines were also observed in other works, where their origin was confirmed [40]–[45]. The temperature behavior of the line corresponding to atoms at the edge of the domain wall demonstrated significant deviations from the Bloch's law even near low

temperatures, associated with the rotation of the easy magnetization axis from the sixth-order axis into the orthogonal plane [46].

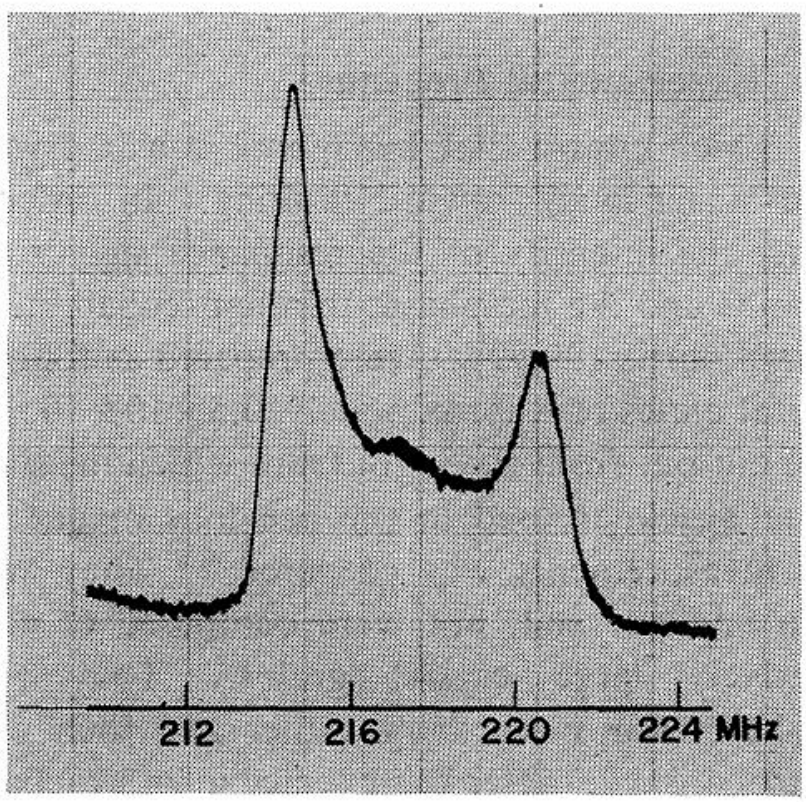

Fig. 1.8. ^{59}Co Internal Field NMR spectrum recorded for metallic Co particles with hcp crystal packing. The signal at 214 MHz corresponds to the domain wall edges, while the signal at 221.5 MHz originates from the atoms located in the center of the domain walls. Figure adapted from [47].

For the first time, the signal from small single-domain fcc Co particles was observed by the same Gossard and Portis [48]. To obtain nanoparticles with a size of 10–15 nm (less than the critical size for the formation of several magnetic domains), they used the method of depositing particles on gamma alumina followed by reduction in a hydrogen stream. For this sample, they observed a single line with a resonant frequency of 216.85 MHz at room temperature. Such an increase in frequency and, consequently, in the local field compared to bulk fcc Co is consistent with the presence of a demagnetizing field in single-domain particles directed against magnetization (that is, parallel to the HFI field). While the theoretically predicted contribution of the demagnetizing field to the local field should be around 6 kG, the actually observed shift was 3.75 kG. The authors explained this discrepancy by the presence of interparticle dipole interactions, which tend to align the magnetic moments of the particles in such a way as to reduce the magnetic energy of the system.

The temperature behavior of single domain fcc Co particles deposited on silicon carbide was studied in [34]. It was shown that with decreasing temperature, the resonant frequency from single-domain Co particles behaves in accordance with the theory of spin waves (Eq. 1.37) up to the $T^{5/2}$ term, with the extrapolated resonance frequency at 0 K being about 220 MHz. In other studies, where single-domain Co particles were studied at low temperatures (4-77 K), the NMR signal in the internal field of the sample was observed in the range of 219-220 MHz [24], [49], [50].

The observation of signals from single-domain particles of metallic Co with hcp packing is difficult compared to single-domain fcc particles, since the fcc structure is experimentally the stable structure at room temperature for nanoparticles with sizes less than 100 nm. In addition, due to the large anisotropy of this structure, the resonance curve from single-domain hcp particles is significantly broadened, which makes it difficult to observe. The accepted reference for the signal from single-domain particles of hcp cobalt is a broad line of irregular shape stretching from 218 to 225 MHz [24], [51], [52].

1.3.2 Binary cobalt compounds

As mentioned above, the term in Eq. (1.23) that depends on the polarization of the conduction electrons by the nearest neighbors of the cobalt atom contributes to the field due to the hyperfine interaction of the cobalt nucleus with electrons. The presence of this term leads to the fact that the replacement of cobalt atoms in the local environment of the studied cobalt nucleus by guest atoms significantly changes the local field on this nucleus. In most cases, the total shift of the resonant frequency upon substitution of several atoms is linearly additive with good accuracy. Substitution of atoms can occur in various binary compounds of cobalt - alloys, solid solutions, intermetallic compounds, multilayer compounds.

From the point of view of ^{59}Co Internal Field NMR, binary systems composed of cobalt and iron are well studied. According to experimental data, the replacement of one cobalt atom by one iron atom leads to a positive shift of the resonant frequency by 10.7 ± 0.5 MHz (Figure 1.9). Among the studied samples were: massive alloys [53]–[60], thin films [19], [61], [62], multilayer films [63]–[65], superlattices [66], and nanoparticles [67]. In the case of samples with a high dilution of cobalt in iron, the main line in the spectrum became the line with a resonant frequency of about 200 MHz, corresponding to the bcc packing of cobalt. Such a packing is unstable for pure cobalt, however, it is often observed in alloys with iron due to the fact that this particular packing is stable in the latter.

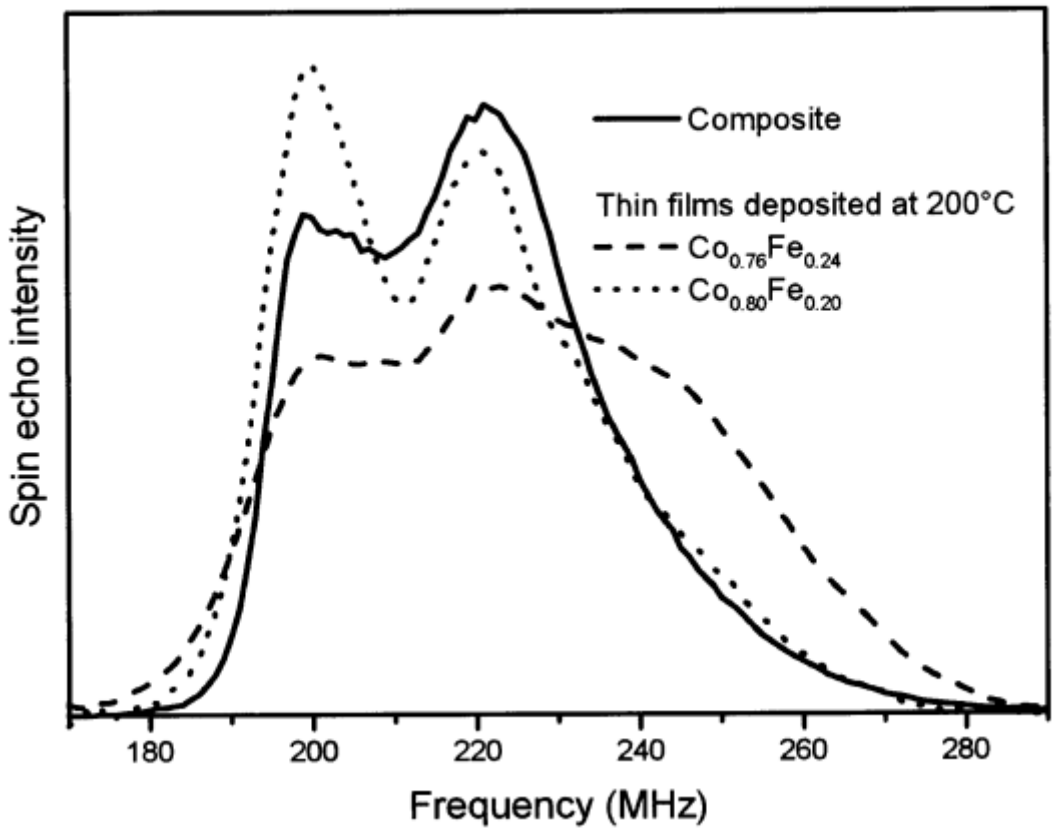

Fig. 1.9. The solid line is the ^{59}Co Internal Field NMR spectrum recorded for the Co-Fe composite obtained by deposition from solution. The dotted and dashed lines show the spectra of thin films obtained by molecular beam deposition with various Co:Fe ratios. The main peak of metallic cobalt with bcc packing is located at a frequency of 200 MHz. The substitution of two cobalt atoms for two iron atoms results in a positive frequency shift of about 20 MHz. Signals are also observed that are stretched into the region of higher frequencies, corresponding to a greater degree of substitution of cobalt for iron. Figure adapted from [68].

In addition to alloys of cobalt with iron, its alloys with other metals, such as: chromium [69]–[74], nickel [73], [75]–[78], manganese [73], [78]–[82], copper [68], [73], [74], [81], [83]–[85], vanadium [77], [78], [82], [86], aluminum [73], [77], [87], [88], titanium [77], [78], [82], etc. were studied. In all these cases, unlike iron, the resonance frequency decreases with the degree of substitution. Thus, in [89], a ^{59}Co NMR spectrum was obtained in the internal field of a cermet with the composition CoAlO/CoAl, where, in addition to the signal from metallic cobalt, signals in the low-frequency region attributed to the cobalt-aluminum alloy were observed (Figure 1.10).

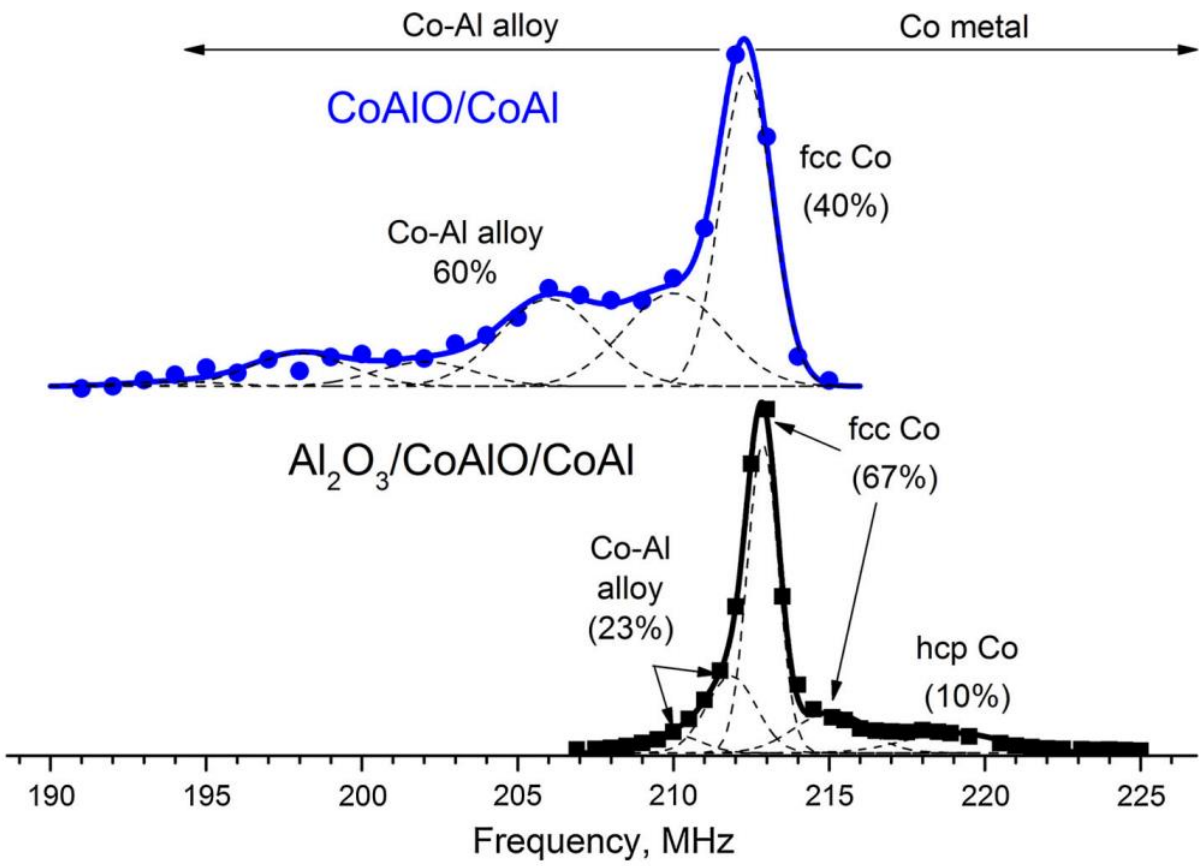

Fig. 1.10. The blue line is the ^{59}Co Internal Field NMR spectrum recorded for the cermet CoAlO/CoAl. The spectrum shows an intense signal in the low-frequency region, indicating the presence of the Co-Al alloy. On the spectrum of the sample obtained with the addition of gibbsite (black), the overall intensity of the lines corresponding to the alloy is much smaller. The figure is adapted from [89].

In addition to binary alloys of cobalt with other metals, more complex alloys (for example, Heusler alloys [90]–[96]), as well as interstitial solution cobalt compounds, such as cobalt carbides [97]–[100], have also been studied. In Heusler alloys, satellite lines are also observed with a resonant frequency depending on the type and number of nearest neighbors replacing cobalt atoms. The introduction of carbon atoms into the cobalt lattice significantly distorts it, reducing the local field on the cobalt nuclei, which leads to a significant decrease in the Larmor frequency and eventually to signals characteristic of cobalt carbides Co_2C and Co_3C.

1.3.3 Superparamagnetic cobalt compounds

When analyzing the ^{59}Co Internal Field NMR spectra of cobalt nanoparticles smaller than 100 nm in size, it is necessary to take into account not only the possible transition from a multidomain to a single domain state, but also the phenomenon of superparamagnetism as explained in Section 1.2.3.

Experimentally, it should manifest itself by an increase in the intensity of the spectrum with decreasing temperature (in addition to an increase in nuclear magnetization according to the Boltzmann law) due to the transition of particles from an unobservable superparamagnetic state to an observable ferromagnetic state. Such an increase in intensity was noted in several works devoted to the study of nanoparticles of metallic cobalt [101]–[103] and was discussed from the point of view of the superparamagnetic transition; however, no estimates of the critical sizes/temperatures were given. It was only in [50] that the temperature limits of blocking cobalt nanoparticles of different sizes into the ferromagnetic state were studied for the first time on Co/SiC samples used as catalysts for the Fischer–Tropsch synthesis. In further publications [24], [104], a more detailed consideration of the dependence of the blocking temperature on particle sizes was given, and theoretical calculations were carried out using the dependence proposed by Neel. The experimental value of the critical particle size at which the transition to the ferromagnetic state occurs was obtained by analyzing the NMR spectra obtained at different temperatures and the distribution of particles along the linear size, obtained using high-resolution TEM. The difference between the theoretically predicted and experimentally found critical sizes was 2.5 times, which showed that the estimation of particle sizes in the entire volume of the sample using the ^{59}Co NMR method in the internal field of the sample is fundamentally possible, but requires additional refinement of the calculated parameters.

Thus, the application of ^{59}Co Internal Field NMR spectroscopy is well described in the literature for samples of bulk metallic cobalt, as well as for binary alloys. The resonant frequencies corresponding to the fcc and hcp packings of cobalt are well known both inside the domains and inside the domain walls. In experiments, resonance frequencies of single-domain cobalt particles shifted by the presence of a demagnetizing field were obtained. The temperature behavior of single domain particles at the limit of the superparamagnetic-ferromagnetic transition has been less studied, primarily because of the lack of suitable samples with a narrow particle size distribution, and also because of the presence of two inaccurately defined parameters in the theoretical model – the effective magnetic anisotropy constant (which also depends the shape of the particles) and the time constant of superparamagnetic relaxation τ_0, which is estimated in a fairly wide range. Other factors affecting the ^{59}Co Internal Field NMR spectra, such as the particle shape factor, interparticle interaction, and electric quadrupole interaction, have been studied much more poorly. The main difficulty in applying this method is the large number of factors affecting the position and shape of the lines, which, in contrast to classical NMR, are much more difficult to eliminate experimentally (for example, dipole interactions are reduced by magic angle spinning in conventional NMR). In this regard, it is necessary to rely on the synthesis of model samples, which help to establish the influence of individual factors.

At the same time, such compounds can constitute models not only for studying the applicability of the method, but also for various functional applications, two of which were considered in this work.

1.4 Functional materials based on cobalt nanoparticles

1.4.1 Fischer-Tropsch catalysts

In the 1920s, German chemists Franz Fischer and Hans Tropsch developed a process for converting a mixture of carbon monoxide and hydrogen into linear alkanes on supported catalysts [105], [106]. The main products of the Fischer-Tropsch synthesis (FTS) - linear alkanes and alkenes - are obtained in carbon chain polymerization reactions:

$$(2n+1)H_2 + nCO \rightarrow C_nH_{2n+2} + nH_2O \quad (1.39)$$

$$2nH_2 + nCO \rightarrow C_nH_{2n} + nH_2O \quad (1.40)$$

These reactions occur at temperatures of 150–250°C (low-temperature FTS) or 250–350°C (high-temperature FTS) at a relatively low reactant pressure (about 1 atm) in the presence of heterogeneous catalysts [107]. Depending on the temperature and the chosen catalyst, the FTS process can produce various synthetic fuels such as gasoline, kerosene or diesel.

Various carbon sources can be used as feedstock to produce a mixture of CO and H_2 (synthesis gas, syngas), such as natural gas (gas-to-liquid process), coal (coal liquefaction process), biomass (biomass-to-liquid process) and others. Recently, the biomass-to-liquid process has been considered as a “green” approach to the use of already existing fuel infrastructure for land and air transport with a zero carbon footprint [108]. To date, more than 10 plants operating on the Fischer-Tropsch process have been opened in the world. The vast majority of these plants are located in Africa (Sasol Company) and in China with natural gas used as the main feedstock, and then coal. Several small-scale commercial and pilot biomass-to-liquid plant are operating across Europe [109].

Supported iron and cobalt particles are most often used as catalysts in practice. Both of these metals show high activity in FTS, which makes iron particles attractive from a financial point of view. Moreover, iron also has high activity in the water gas shift reaction and greater selectivity for lighter hydrocarbons. Thus, the use of iron is preferable for initial mixtures with a low H_2/CO ratio, as well as for the synthesis of light fuels (gasoline). For the synthesis of heavy fuels (kerosene and diesel), cobalt nanoparticles, which do not show activity in the water gas shift reaction are much better suited and also have a high selectivity to C_{5+} hydrocarbons.

The catalytic properties (activity, selectivity, resistance to carburization) of cobalt nanoparticles in FTS depend on many factors. In addition to the basic geometric considerations about the increase in specific activity with an increase in the specific surface of particles (that is, a decrease in their size), one must consider that particles too small in diameter demonstrate very poor FTS performance despite their high specific surface area. A large number of catalytic experiments show that cobalt nanoparticles smaller than 4–10 nm in size (according to various data) exhibit much lower activity, and that their selectivity shifts towards CH_4 [111]–[116]. This effect can be related to the fact that cobalt particles with hcp packing exhibit the highest activity and selectivity to C_{5+} hydrocarbons [117]–[122], while fcc packing is more stable in single domain particles.

The dependence of the catalytic properties of cobalt nanoparticles on their morphology and crystal structure makes ^{59}Co Internal Field NMR spectroscopy a promising method for studying the structure of supported cobalt FTS catalysts. One of the main advantages of this method is that it allows obtaining information about the entire volume of the sample, in contrast to local microscopic methods. At the same time, ^{59}Co NMR spectra potentially contain a vast amount of data on the crystal and magnetic structure of particles, as well as on their morphology. However, a large number of factors affecting the shape and position of the NMR spectrum make it difficult to analyze it, that is, the use of this method requires the development of a systematic approach and the accumulation of data on model samples.

1.5 References

[1] W. Marshall, “Orientation of Nuclei in Ferromagnets,” *Phys. Rev.*, vol. 110, no. 6, pp. 1280–1285, Jun. 1958.

[2] A. C. Gossard and A. M. Portis, “Observation of Nuclear Resonance in a Ferromagnet,” *Phys. Rev. Lett.*, vol. 3, no. 4, pp. 164–166, Aug. 1959.

[3] A. M. Portis and A. C. Gossard, “Nuclear Resonance in Ferromagnetic Cobalt,” *J. Appl. Phys.*, vol. 31, no. 5, pp. S205–S213, May 1960.

[4] A. P. Guimarães, *Magnetism and Magnetic Resonance in Solids*. Wiley-VCH, 1998.

[5] P. G. de Gennes, P. A. Pincus, F. Hartmann-Boutron, and J. M. Winter, “Nuclear Magnetic Resonance Modes in Magnetic Material. I. Theory,” *Phys. Rev.*, vol. 129, no. 3, pp. 1105–1115, Feb. 1963.

[6] G. L. Witt and A. M. Portis, “Nuclear Magnetic Resonance Modes in Magnetic Materials. II. Experiment,” *Phys. Rev.*, vol. 135, no. 6A, pp. A1616–A1618, Sep. 1964.

[7] A. S. Borovik-Romanov, Y. M. Bunkov, B. S. Dumesh, M. I. Kurkin, M. P. Petrov, and V. P. Chekmarev, “The spin echo in systems with a coupled electron-nuclear precession,” *Uspekhi Fiz. Nauk*, vol. 142, no. 4, p. 537, 1984.

[8] С. В. Вонсовский, *Магнетизм. Магнитные свойства диа-, пара-, ферро-, антиферро- и ферримагнетиков*. Москва: Наука, 1971.

[9] C. Kittel, “Physical Theory of Ferromagnetic Domains,” *Rev. Mod. Phys.*, vol. 21, no. 4, pp. 541–583, Oct. 1949.

[10] D. L. Leslie-Pelecky and R. D. Rieke, “Magnetic Properties of Nanostructured Materials,” *Chem. Mater.*, vol. 8, no. 8, pp. 1770–1783, Jan. 1996.

[11] A. Hubert and R. Schäfer, “Domain Theory,” in *Magnetic Domains*, Berlin, Heidelberg: Springer Berlin Heidelberg, pp. 99–335.

[12] Д. Джексон, *Классическая электродинамика*. Москва: Мир, 1965.

[13] P. Panissod, “Structural and Magnetic Investigations of Ferromagnets by NMR. Application to Magnetic Metallic Multilayers,” in *Frontiers in Magnetism of Reduced Dimension Systems*, Dordrecht: Springer Netherlands, 1998, pp. 225–270.

[14] R. E. Watson and A. J. Freeman, “Origin of Effective Fields in Magnetic Materials,” *Phys. Rev.*,

vol. 123, no. 6, pp. 2027–2047, Sep. 1961.

[15] P. Panissod, J. P. Jay, C. Meny, M. Wojcik, and E. Jedryka, “NMR analysis of buried metallic interfaces,” *Hyperfine Interact.*, vol. 97–98, no. 1, pp. 75–98, Dec. 1996.

[16] C. P. Slichter, “Advanced Concepts in Pulsed Magnetic Resonance,” 1990, pp. 367–429.

[17] E. L. Hahn, “Spin Echoes,” *Phys. Rev.*, vol. 80, no. 4, pp. 580–594, Nov. 1950.

[18] J.-P. Jay, “Etude par Resonance Magnetique Nucleaire de l’ordre à courte distance dans le système Cobalt/Fer : De l’alliage massif à la multicouche,” Université Louis Pasteur - Strasbourg I, 1995.

[19] P. Panissod, J. P. Jay, C. Meny, M. Wojcik, and E. Jedryka, “NMR analysis of buried metallic interfaces,” *Hyperfine Interact.*, vol. 97–98, no. 1, pp. 75–98, Dec. 1996.

[20] S. Bedanta, O. Petracic, and W. Kleemann, “Supermagnetism,” 2015, pp. 1–83.

[21] I. L. Prejbeanu, L. D. Buda, U. Ebels, M. Viret, C. Fermon, and K. Ounadjela, “Domain structures in epitaxial (101~0) Co wires,” *IEEE Trans. Magn.*, vol. 37, no. 4, pp. 2108–2110, Jul. 2001.

[22] G. J. Strijkers, J. H. J. Dalderop, M. A. A. Broeksteeg, H. J. M. Swagten, and W. J. M. de Jonge, “Structure and magnetization of arrays of electrodeposited Co wires in anodic alumina,” *J. Appl. Phys.*, vol. 86, no. 9, pp. 5141–5145, Nov. 1999.

[23] L. Neel, “Théorie du traînage magnétique des ferromagnétiques en grains fins avec applications aux terres cuites.,” *Ann. Geofis.*, vol. 5, no. 99, 1949.

[24] Y. Liu *et al.*, “Sampling the structure and chemical order in assemblies of ferromagnetic nanoparticles by nuclear magnetic resonance,” *Nat. Commun.*, vol. 7, no. 1, p. 11532, Sep. 2016.

[25] Y. Barnier, “Contribution à l’étude des propriétés magnétiques du cobalt et des alliages de fer-cobalt (Thèse d’Ingénieur-Docteur),” Université de Grenoble, 1963.

[26] E. P. Wohlfarth, “Chapter 1 Iron, cobalt and nickel,” 1980, pp. 1–70.

[27] M. Respaud *et al.*, “Dynamical properties of non-interacting Co nanoparticles,” *Europhys. Lett.*, vol. 47, no. 1, pp. 122–127, Jul. 1999.

[28] A. S. Andreev, O. B. Lapina, and S. V. Cherepanova, “A New Insight into Cobalt Metal Powder Internal Field 59Co NMR Spectra,” *Appl. Magn. Reson.*, vol. 45, no. 10, pp. 1009–1017, Oct. 2014.

[29] M. Gellesch *et al.*, "Compositional analysis of multi-element magnetic nanoparticles with a combined NMR and TEM approach," *J. Nanoparticle Res.*, vol. 19, no. 9, p. 307, Sep. 2017.

[30] R. Speight, A. Wong, P. Ellis, T. Hyde, P. T. Bishop, and M. E. Smith, "A 59Co NMR study to observe the effects of ball milling on small ferromagnetic cobalt particles," *Solid State Nucl. Magn. Reson.*, vol. 35, no. 2, pp. 67–73, Apr. 2009.

[31] H. K. Choudhary, M. Manjunatha, R. Damle, K. P. Ramesh, and B. Sahoo, "Solvent dependent morphology and 59 Co internal field NMR study of Co-aggregates synthesized by a wet chemical method," *Phys. Chem. Chem. Phys.*, vol. 20, no. 26, pp. 17739–17750, 2018.

[32] P. Panissod and C. Mény, "Nuclear magnetic resonance investigations of the structure and magnetic properties of metallic multilayers and nanocomposites," *Appl. Magn. Reson.*, vol. 19, no. 3–4, pp. 447–460, Jul. 2000.

[33] C. Meny, E. Jedryka, and P. Panissod, "Satellite structure of 59 Co NMR spectra in some Co alloys," *J. Phys. Condens. Matter*, vol. 5, no. 10, pp. 1547–1556, Mar. 1993.

[34] A. S. Andreev, J.-B. D'Espinose De Lacaillerie, O. B. Lapina, and A. Gerashenko, "Thermal stability and hcp-fcc allotropic transformation in supported Co metal catalysts probed near operando by ferromagnetic NMR," *Phys. Chem. Chem. Phys.*, vol. 17, no. 22, 2015.

[35] E. C. Stoner, "Collective electron ferronmagnetism," *Proc. R. Soc. London. Ser. A. Math. Phys. Sci.*, vol. 165, no. 922, pp. 372–414, Apr. 1938.

[36] F. J. Dyson, "Thermodynamic Behavior of an Ideal Ferromagnet," *Phys. Rev.*, vol. 102, no. 5, pp. 1230–1244, Jun. 1956.

[37] F. Bloch, "Zur Theorie des Ferromagnetismus," *Zeitschrift für Phys.*, vol. 61, no. 3–4, pp. 206–219, Mar. 1930.

[38] Y. Kôi, A. Tsujimura, and T. Kushida, "NMR of Co 59 in Ferromagnetic Hexagonal Cobalt Metal," *J. Phys. Soc. Japan*, vol. 15, no. 11, pp. 2100–2100, Nov. 1960.

[39] M. Kawakami, T. Hihara, Y. Kōi, and T. Wakiyama, "The Co 59 Nuclear Magnetic Resonance in Hexagonal Cobalt," *J. Phys. Soc. Japan*, vol. 33, no. 6, pp. 1591–1598, Dec. 1972.

[40] H. Enokiya, "Nuclear Magnetic Resonance and Nuclear Relaxation in hcp Cobalt," *J. Phys. Soc. Japan*, vol. 42, no. 3, pp. 796–804, Mar. 1977.

[41] H. P. Kunkel and C. W. Searle, "Experimental identification of domain-wall-center and domain-

wall-edge NMR resonances in magnetically ordered materials," *Phys. Rev. B*, vol. 23, no. 1, pp. 65–68, Jan. 1981.

[42] H. Brömer and H. L. Huber, "Nuclear magnetic resonance in ferromagnetic HCP and FCC 59cobalt," *J. Magn. Magn. Mater.*, vol. 8, no. 1, pp. 61–64, Mar. 1978.

[43] D. Fekete, H. Boasson, A. Grayevski, V. Zevin, and N. Kaplan, "Anisotropic hyperfine interactions in ferromagnetic hcp Co," *Phys. Rev. B*, vol. 17, no. 1, pp. 347–354, Jan. 1978.

[44] C. W. Searle, H. P. Kunkel, S. Kupca, and I. Maartense, "NMR enhancement of a modulating field due to the anisotropic component of the hyperfine field in hcp Co and Y <math display="inline"> <mrow> <msub> <mrow> <mi mathvariant="normal">Co</mi> </mrow> <mrow> <mn>5</mn> </mrow> </msub> </mrow> </math>," *Phys. Rev. B*, vol. 15, no. 7, pp. 3305–3308, Apr. 1977.

[45] S. G. Bailey, D. C. Creagh, and G. V. H. Wilson, "Domain wall and 'domain' 59Co NMR in hexagonal cobalt," *Phys. Lett. A*, vol. 44, no. 3, pp. 229–230, Jun. 1973.

[46] M. Kawakami and H. Enokiya, "Anomaly in Temperature Dependence of 59 Co NMR Frequency in HCP Co," *J. Phys. Soc. Japan*, vol. 55, no. 11, pp. 4038–4043, Nov. 1986.

[47] M. Kawakami, T. Hihara, Y. Kōi, and T. Wakiyama, "The Co 59 Nuclear Magnetic Resonance in Hexagonal Cobalt," *J. Phys. Soc. Japan*, vol. 33, no. 6, pp. 1591–1598, Dec. 1972.

[48] A. C. Gossard, A. M. Portis, M. Rubinstein, and R. H. Lindquist, "Ferromagnetic Nuclear Resonance of Single-Domain Cobalt Particles," *Phys. Rev.*, vol. 138, no. 5A, pp. A1415–A1421, May 1965.

[49] Y. D. Zhang, J. I. Budnick, W. A. Hines, S. A. Majetich, and E. M. Kirkpatrick, "Microstructure and magnetic behavior of carbon-coated Co nanoparticles studied by nuclear magnetic resonance," *Appl. Phys. Lett.*, vol. 76, no. 1, pp. 94–96, Jan. 2000.

[50] Y. Liu *et al.*, "Titania-Decorated Silicon Carbide-Containing Cobalt Catalyst for Fischer–Tropsch Synthesis," *ACS Catal.*, vol. 3, no. 3, pp. 393–404, Mar. 2013.

[51] V. V. Matveev, D. A. Baranov, G. Y. Yurkov, N. G. Akatiev, I. P. Dotsenko, and S. P. Gubin, "Cobalt nanoparticles with preferential hcp structure: A confirmation by X-ray diffraction and NMR," *Chem. Phys. Lett.*, vol. 422, no. 4–6, pp. 402–405, May 2006.

[52] A. S. Andreev *et al.*, "Magnetic and dielectric properties of carbon nanotubes with embedded cobalt nanoparticles," *Carbon N. Y.*, vol. 114, pp. 39–49, Apr. 2017.

[53] Y. Kôi, A. Tsujimura, T. Hihara, and T. Kushida, “NMR of Co 59 in Ferromagnetic Cobalt Alloys,” *J. Phys. Soc. Japan*, vol. 16, no. 3, pp. 574–574, Mar. 1961.

[54] M. Rubinstein, “Hyperfine Field Spectra of Binary Fe-Co Alloys: Nuclear Magnetic Resonance of <math display="inline"> <mrow> <mmultiscripts> <mrow> <mi mathvariant="normal">Fe</mi> </mrow> <mprescripts/> <mrow/> <mrow> <mn>57</mn> </mrow> <mrow/> <mrow/> </mmultiscripts>,” *Phys. Rev.*, vol. 172, no. 2, pp. 277–283, Aug. 1968.

[55] G. H. Strauss and D. W. Forester, “Short-Range Order Effects on 59 Co NMR Spectra in Equiatomic FeCo,” *J. Appl. Phys.*, vol. 42, no. 4, pp. 1304–1305, Mar. 1971.

[56] G. H. Stauss, “Hyperfine Fields in Dilute Alloys of Co in Fe,” *Phys. Rev. B*, vol. 4, no. 9, pp. 3106–3110, Nov. 1971.

[57] Y. Muraoka, M. Shiga, H. Yasuoka, and Y. Nakamura, “NMR Study of Ordered and Disordered Fe-Co Alloy,” *J. Phys. Soc. Japan*, vol. 40, no. 2, pp. 414–417, Feb. 1976.

[58] V. Pierron-Bohnes, M. C. Cadeville, and F. Gautier, “Magnetism and local order in dilute FeCo alloys,” *J. Phys. F Met. Phys.*, vol. 13, no. 8, pp. 1689–1713, Aug. 1983.

[59] I. G. Shmakov, O. I. Gorbatov, V. V. Serikov, N. M. Kleinerman, O. A. Golovnya, and Y. N. Gornostyrev, “Short-range order formation in Fe-Co alloys: NMR study and first-principles calculations,” *J. Alloys Compd.*, vol. 782, pp. 1008–1014, Apr. 2019.

[60] V. V. Serikov, N. M. Kleinerman, and O. A. Golovnya, “NMR and Mössbauer study of peculiarities of the structure formation in Fe–Co alloys,” *Phys. Met. Metallogr.*, vol. 118, no. 11, pp. 1040–1047, Nov. 2017.

[61] T. Mühge, T. Zeidler, Q. Wang, C. Morawe, N. Metoki, and H. Zabel, “Structural and magnetic studies of Fe x Co 1− x (001) alloy films on MgO(001) substrates,” *J. Appl. Phys.*, vol. 77, no. 3, pp. 1055–1060, Feb. 1995.

[62] M. Wojcik, J. P. Jay, P. Panissod, E. Jedryka, J. Dekoster, and G. Langouche, “New phases and chemical short range order in co-deposited CoFe thin films with bcc structure: an NMR study,” *Zeitschrift für Phys. B Condens. Matter*, vol. 103, no. 1, pp. 5–12, Mar. 1997.

[63] P. Houdy *et al.*, “Magnetic and structural properties of rf-sputtered Co/Fe and Co/Cr multilayers,” *J. Appl. Phys.*, vol. 69, no. 8, pp. 5667–5669, Apr. 1991.

[64] N. A. Lesnik *et al.*, “Local structure in CoFe/Al2O3 multilayers determined by nuclear magnetic

resonance," *J. Magn. Magn. Mater.*, vol. 242–245, pp. 943–945, Apr. 2002.

[65] H. G. Silva *et al.*, "Magnetic and transport properties of diluted granular multilayers," *J. Appl. Phys.*, vol. 106, no. 11, p. 113910, Dec. 2009.

[66] J. Dekoster, E. Jedryka, C. Mény, and G. Langouche, "Epitaxial growth of bcc Co/Fe superlattices," *J. Magn. Magn. Mater.*, vol. 121, no. 1–3, pp. 69–72, Mar. 1993.

[67] A. S. Andreev *et al.*, "Internal field 59Co NMR study of cobalt-iron nanoparticles during the activation of CoFe2/CaO catalyst for carbon nanotube synthesis," *J. Catal.*, vol. 358, pp. 62–70, Feb. 2018.

[68] J. P. Jay, I.-S. Jurca, G. Pourroy, N. Viart, C. Mény, and P. Panissod, "59Co NMR study in Co–Fe alloys/Co magnetite composites," *Solid State Sci.*, vol. 3, no. 3, pp. 301–308, Mar. 2001.

[69] M. Malinowska, C. Mény, E. Jedryka, and P. Panissod, "The anisotropic first-neighbour contribution to the hyperfine field in hexagonal-close-packed Co: a nuclear magnetic resonance study of diluted alloys and multilayers," *J. Phys. Condens. Matter*, vol. 10, no. 22, pp. 4919–4928, Jun. 1998.

[70] M. Kawakami, "Co 59 NMR in Hexagonal Cobalt-Base Dilute Alloys with 3d Transition Metals," *J. Phys. Soc. Japan*, vol. 40, no. 1, pp. 56–62, Jan. 1976.

[71] T. M. Shavishvili and I. G. Kiliptari, "Distribution of hyperfine fields and magnetic perturbation in cobalt alloys with 3d transition metals," *Phys. Status Solidi*, vol. 92, no. 1, pp. 39–47, Mar. 1979.

[72] S. Kobayashi, K. Asayama, and J. Itoh, "Nuclear Magnetic Resonance In Co Alloys," *J. Phys. Soc. Japan*, vol. 21, no. 1, pp. 65–74, Jan. 1966.

[73] Y. Kôi, A. Tsujimura, T. Hihara, and T. Kushida, "NMR of Co 59 in Ferromagnetic Cobalt Alloys," *J. Phys. Soc. Japan*, vol. 16, no. 3, pp. 574–574, Mar. 1961.

[74] C. Meny, E. Jedryka, and P. Panissod, "Satellite structure of 59 Co NMR spectra in some Co alloys," *J. Phys. Condens. Matter*, vol. 5, no. 10, pp. 1547–1556, Mar. 1993.

[75] L. H. Bennett and R. L. Streever, "Internal Magnetic Fields in Nickel-Rich Nickel-Cobalt Alloys," *J. Appl. Phys.*, vol. 33, no. 3, pp. 1093–1094, Mar. 1962.

[76] P. C. Riedi and R. G. Scurlock, "Satellite Lines in the 59 Co Resonance in Cobalt-Nickel Alloys," *J. Appl. Phys.*, vol. 39, no. 2, pp. 1241–1242, Feb. 1968.

[77] S. Kobayashi, K. Asayama, and J. Itoh, “Nuclear Magnetic Resonance In Co Alloys,” *J. Phys. Soc. Japan*, vol. 21, no. 1, pp. 65–74, Jan. 1966.

[78] T. M. Shavishvili and I. G. Kiliptari, “Distribution of hyperfine fields and magnetic perturbation in cobalt alloys with 3d transition metals,” *Phys. Status Solidi*, vol. 92, no. 1, pp. 39–47, Mar. 1979.

[79] T. Thomson, P. C. Riedi, Q. Wang, and H. Zabe, “59Co and 55Mn NMR of CoMn alloys and multilayers,” *J. Appl. Phys.*, vol. 79, no. 8, p. 6300, 1996.

[80] H. Yasuoka, S. Hoshinouchi, Y. Nakamura, M. Matsui, and K. Adachi, “Nuclear Magnetic Resonance of Co59 in Co-Mn Alloys,” *Phys. Status Solidi*, vol. 46, no. 2, pp. K81–K84, Aug. 1971.

[81] M. Malinowska, C. Mény, E. Jedryka, and P. Panissod, “The anisotropic first-neighbour contribution to the hyperfine field in hexagonal-close-packed Co: a nuclear magnetic resonance study of diluted alloys and multilayers,” *J. Phys. Condens. Matter*, vol. 10, no. 22, pp. 4919–4928, Jun. 1998.

[82] M. Kawakami, “Co 59 NMR in Hexagonal Cobalt-Base Dilute Alloys with 3d Transition Metals,” *J. Phys. Soc. Japan*, vol. 40, no. 1, pp. 56–62, Jan. 1976.

[83] E. H. C. . Sinnecker, I. . Oliveira, P. Tiberto, and A. . Guimarães, “Magnetic and structural properties of Cu–Co granular alloys measured with NMR,” *J. Magn. Magn. Mater.*, vol. 218, no. 2–3, pp. 132–136, Aug. 2000.

[84] S. Dhara, R. R. Chowdhury, and B. Bandyopadhyay, “Disorder in Co-Cu granular alloys studied by 59Co NMR,” *J. Magn. Magn. Mater.*, vol. 471, pp. 355–358, Feb. 2019.

[85] M. Malinowska *et al.*, “Identification of magnetic phases in granular Co10Cu90 alloy using NMR method,” *J. Magn. Magn. Mater.*, vol. 198–199, pp. 599–601, Jun. 1999.

[86] M. Kawakami and Y. Aoki, “Phase dependent NMR spectra of Co-rich CoV alloys,” *J. Phys. F Met. Phys.*, vol. 10, no. 9, pp. 2067–2072, Sep. 1980.

[87] A. S. Andreev *et al.*, “Design of Al2O3/CoAlO/CoAl Porous Ceramometal for Multiple Applications as Catalytic Supports,” *Adv. Mater. Res.*, vol. 702, pp. 79–87, May 2013.

[88] S. F. Tikhov *et al.*, “Ceramic matrix composites prepared from CoAl powders,” *J. Mater. Sci.*, vol. 51, no. 23, pp. 10487–10498, Dec. 2016.

[89] S. F. Tikhov *et al.*, “Ceramic matrix composites prepared from CoAl powders,” *J. Mater. Sci.*, vol. 51, no. 23, pp. 10487–10498, Dec. 2016.

[90] S. Wurmehl, J. T. Kohlhepp, H. J. M. Swagten, and B. Koopmans, “59 Co nuclear magnetic resonance study of the local distribution of atoms in the Heusler compound Co 2 FeAl 0.5 Si 0.5,” *J. Appl. Phys.*, vol. 111, no. 4, p. 043903, Feb. 2012.

[91] S. Wurmehl *et al.*, “Electronic structure and spectroscopy of the quaternary Heusler alloy Co 2 Cr 1− x Fe x Al,” *J. Phys. D. Appl. Phys.*, vol. 39, no. 5, pp. 803–815, Mar. 2006.

[92] A. Shinogi, M. Tanaka, and K. Endo, “Positive Contributions to the Hyperfine Fields at Co Nucleus in the Heusler Alloys; Co 2 TiSn and Co 2- x (Ni, Fe) x TiSn,” *J. Phys. Soc. Japan*, vol. 44, no. 3, pp. 774–780, Mar. 1978.

[93] S. Wurmehl *et al.*, “Probing the random distribution of half-metallic Co2Mn1−xFexSi Heusler alloys,” *Appl. Phys. Lett.*, vol. 91, no. 5, p. 052506, Jul. 2007.

[94] A. Shinogi, “The Origin of the Positive Hyperfine Field at 59 Co in a Ferromagnetic Heusler Alloy: Co 2 TiAl,” *J. Phys. Soc. Japan*, vol. 54, no. 1, pp. 400–408, Jan. 1985.

[95] S. Wurmehl *et al.*, “Local formation of a Heusler structure in CoFe–Al alloys,” *Appl. Phys. Lett.*, vol. 98, no. 1, p. 012506, Jan. 2011.

[96] S. Wurmehl *et al.*, “Effects of random distribution of Mn,Fe in Co2Mn1−xFexSi Heusler compounds probed by Mn55 nuclear magnetic resonance,” *J. Appl. Phys.*, vol. 103, no. 7, p. 07D706, Apr. 2008.

[97] G. Han *et al.*, “Extreme Enhancement of Carbon Hydrogasification via Mechanochemistry,” *Angew. Chemie Int. Ed.*, vol. 61, no. 18, Apr. 2022.

[98] K. N. Mikhalev *et al.*, “Magnetic state and phase composition of carbon-encapsulated Co@C nanoparticles according to 59 Co, 13 C NMR data and Raman spectroscopy,” *Mater. Res. Express*, vol. 5, no. 5, p. 055033, May 2018.

[99] K. Hiraoka, A. Oota, and H. Jinushi, “NMR and Magnetic Studies of Mechanically Alloyed Co 75 C 25,” *J. Phys. Soc. Japan*, vol. 77, no. 7, p. 074705, Jul. 2008.

[100] M. C. Cadeville and C. Lerner, “On the electronic structure of interstitial transition-metal based alloys with boron and carbon impurities,” *Philos. Mag.*, vol. 33, no. 5, pp. 801–824, May 1976.

[101] W. Hines, J. Budnick, D. Perry, S. Majetich, R. Booth, and M. Sachan, “Nuclear magnetic

resonance and magnetization study of surfactant-coated epsilon-Co nanoparticles," *Phys. status solidi*, vol. 248, no. 3, pp. 741–747, Mar. 2011.

[102] T. Thomson, P. C. Riedi, S. Sankar, and A. E. Berkowitz, "Nuclear magnetic resonance investigations of Co nanoclusters in a SiO2 thin film matrix," *J. Appl. Phys.*, vol. 81, no. 8, pp. 5549–5551, Apr. 1997.

[103] Y. D. Zhang, J. I. Budnick, W. A. Hines, S. A. Majetich, and E. M. Kirkpatrick, "Microstructure and magnetic behavior of carbon-coated Co nanoparticles studied by nuclear magnetic resonance," *Appl. Phys. Lett.*, vol. 76, no. 1, pp. 94–96, Jan. 2000.

[104] Y. Liu, I. Florea, O. Ersen, C. Pham-Huu, and C. Meny, "Silicon carbide coated with TiO 2 with enhanced cobalt active phase dispersion for Fischer–Tropsch synthesis," *Chem. Commun.*, vol. 51, no. 1, pp. 145–148, 2015.

[105] F. Fischer and H. Tropsch, "The preparation of synthetic oil mixtures (synthol) from carbon monoxide and hydrogen," *Brennstoff-Chem*, vol. 4, pp. 276–285, 1923.

[106] F. Fischer and H. Tropsch, "The synthesis of petroleum at atmospheric pressures from gasification products of coal," *Brennstoff-Chemie*, vol. 7, pp. 97–104, 1926.

[107] Z. Gholami, Z. Tišler, and V. Rubáš, "Recent advances in Fischer-Tropsch synthesis using cobalt-based catalysts: a review on supports, promoters, and reactors," *Catal. Rev.*, vol. 63, no. 3, pp. 512–595, Jul. 2021.

[108] Z. Teimouri, V. B. Borugadda, A. K. Dalai, and N. Abatzoglou, "Application of computational fluid dynamics for modeling of Fischer-Tropsch synthesis as a sustainable energy resource in different reactor configurations: A review," *Renew. Sustain. Energy Rev.*, vol. 160, p. 112287, May 2022.

[109] S. A. Mesfun, "Biomass to Liquids (BtL) via Fischer-Tropsch – A Brief Review," 2022. [Online]. Available: https://etipbioenergy.eu/biomass-to-liquids-btl-via-fischer-tropsch-a-brief-review.

[110] N. E. Tsakoumis, J. C. Walmsley, M. Rønning, W. van Beek, E. Rytter, and A. Holmen, "Evaluation of Reoxidation Thresholds for γ-Al 2 O 3 -Supported Cobalt Catalysts under Fischer–Tropsch Synthesis Conditions," *J. Am. Chem. Soc.*, vol. 139, no. 10, pp. 3706–3715, Mar. 2017.

[111] G. L. Bezemer *et al.*, "Cobalt Particle Size Effects in the Fischer−Tropsch Reaction Studied

with Carbon Nanofiber Supported Catalysts," *J. Am. Chem. Soc.*, vol. 128, no. 12, pp. 3956–3964, Mar. 2006.

[112] A. Barbier, A. Tuel, I. Arcon, A. Kodre, and G. A. Martin, "Characterization and Catalytic Behavior of Co/SiO2 Catalysts: Influence of Dispersion in the Fischer–Tropsch Reaction," *J. Catal.*, vol. 200, no. 1, pp. 106–116, May 2001.

[113] A. Tuxen *et al.*, "Size-Dependent Dissociation of Carbon Monoxide on Cobalt Nanoparticles," *J. Am. Chem. Soc.*, vol. 135, no. 6, pp. 2273–2278, Feb. 2013.

[114] E. Rytter, N. E. Tsakoumis, and A. Holmen, "On the selectivity to higher hydrocarbons in Co-based Fischer–Tropsch synthesis," *Catal. Today*, vol. 261, pp. 3–16, Mar. 2016.

[115] N. E. Tsakoumis, M. Rønning, Ø. Borg, E. Rytter, and A. Holmen, "Deactivation of cobalt based Fischer–Tropsch catalysts: A review," *Catal. Today*, vol. 154, no. 3–4, pp. 162–182, Sep. 2010.

[116] O. Ducreux, B. Rebours, J. Lynch, M. Roy-Auberger, and D. Bazin, "Microstructure of Supported Cobalt Fischer-Tropsch Catalysts," *Oil Gas Sci. Technol. - Rev. l'IFP*, vol. 64, no. 1, pp. 49–62, Jan. 2009.

[117] D. I. Enache, B. Rebours, M. Roy-Auberger, and R. Revel, "In Situ XRD Study of the Influence of Thermal Treatment on the Characteristics and the Catalytic Properties of Cobalt-Based Fischer–Tropsch Catalysts," *J. Catal.*, vol. 205, no. 2, pp. 346–353, Jan. 2002.

[118] H. Karaca *et al.*, "Structure and catalytic performance of Pt-promoted alumina-supported cobalt catalysts under realistic conditions of Fischer–Tropsch synthesis," *J. Catal.*, vol. 277, no. 1, pp. 14–26, Jan. 2011.

[119] M. K. Gnanamani, G. Jacobs, W. D. Shafer, and B. H. Davis, "Fischer–Tropsch synthesis: Activity of metallic phases of cobalt supported on silica," *Catal. Today*, vol. 215, pp. 13–17, Oct. 2013.

[120] S. Lyu *et al.*, "Role of Active Phase in Fischer–Tropsch Synthesis: Experimental Evidence of CO Activation over Single-Phase Cobalt Catalysts," *ACS Catal.*, vol. 8, no. 9, pp. 7787–7798, Sep. 2018.

[121] J.-X. Liu, H.-Y. Su, D.-P. Sun, B.-Y. Zhang, and W.-X. Li, "Crystallographic Dependence of CO Activation on Cobalt Catalysts: HCP versus FCC," *J. Am. Chem. Soc.*, vol. 135, no. 44, pp. 16284–16287, Nov. 2013.

Chapter 2: Experimental methods

2.1 ^{59}Co Internal Field NMR

^{59}Co Internal Field NMR spectra were recorded using a 500 MHz Bruker Avance III pulsed Fourier spectrometer (Bruker, USA) at the Institute of Metal Physics, Ural Branch, Russian Academy of Sciences, Yekaterinburg, Russia. The spectra were recorded outside of the spectrometer magnet in a home-made probe with an operating frequency range of 150–300 MHz. For low-temperature experiments, the probe was placed in a helium cryostat (Oxford Technologies, UK) with the possibility of temperature measurement within 4.2-300 K range with an accuracy of 0.1 K. The schematic diagram of the experimental setup is shown in Figure 2.1. Tuning to the resonant frequency and impedance matching of the probe were carried out using an automated system based on stepper motors, which were controlled using the feedback obtained from a standard Bruker preamplifier/wobbulator unit. The software for automatic probe tuning was developed in the Institute of Metal Physics, Yekaterinburg, Russia.

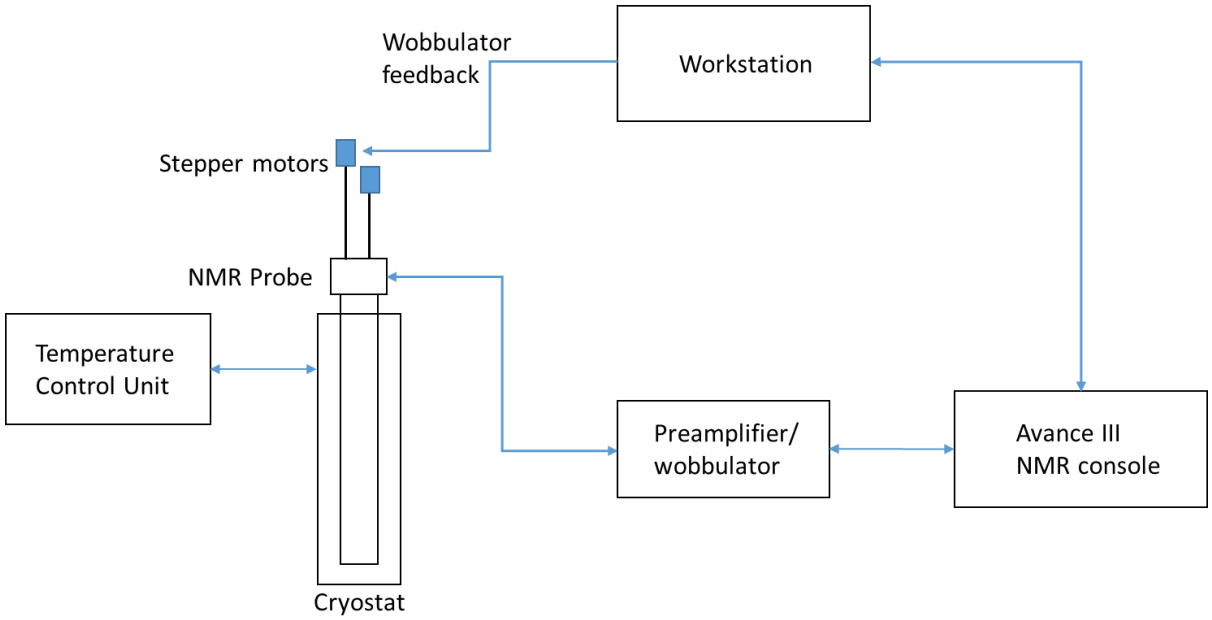

Fig. 2.1. Schematic diagram of the experimental setup. The stepper motors for automatic tuning and matching of the probe are controlled using the wobbulator signal obtained in Topspin 3.1 NMR software (Bruker).

The ^{59}Co Internal Field NMR spectra have a width that is 1–2 orders of magnitude greater than the frequency sweep width available for pulsed NMR spectrometers. There is also a limitation on the shortest possible pulse length, which is necessary for uniform excitation of broad lines. Thus, the spectra were recorded step by step on a set of carrier frequencies covering the range in which the signal amplitude was nonzero. The carrier frequency step for all samples was 0.5 MHz, which made it possible to obtain spectra with sufficient resolution (the width at half maximum of the narrow line of fcc cobalt domain walls usually lies in the range of 2–5 MHz).

The spectra were recorded using a solid echo sequence:

$$\theta - \tau - \theta \tag{2.1}$$

where the length of the radio frequency pulse θ was chosen equal to 0.5 μs for uniform excitation of the spectral line within the 1 MHz frequency sweep of the spectrometer and taking into account the quality factor of the sensor at frequencies of 200–250 MHz. The delay between the pulses τ was 8 μs to observe the echo signal outside the "dead" time of the spectrometer, which is determined by transient oscillatory processes in the radio frequency circuit after the RF pulse is turned off. Since the echo delay and transverse relaxation times T_2 of the magnetization in the samples were of the same order (T_2 usually lies in the range of 10-20 μs at room temperature for ferromagnetic cobalt samples), to obtain a quantitative signal intensity, the relaxation time T_2 was measured at one or more points in each experiment. The short longitudinal relaxation time T_1 (tens of ms) made it possible to record spin echo signals at a frequency of 30 experiments per second.

As mentioned above, the amplitude of the spin echo signal in a ferromagnet is enhanced by a factor of η (Eq. 1.28) compared to the signal from diamagnetic compounds in conventional NMR, and the value of this enhancement factor can vary significantly with frequency depending on the magnetic and crystal structure of the sample. Thus, in order to obtain quantitative information from the NMR spectrum, it is necessary to correct the spectrum for the enhancement factor. For this purpose, the experimental RF irradiation was swept both in frequency and power [19]. The power of the RF pulse at which the maximum amplitude of the spectrum is achieved at each frequency step is called optimal. In turn, this power is proportional to the square of the amplitude of the optimal magnetic field, which is inversely proportional to the enhancement factor:

$$P_{opt} \propto B_{opt}^2 \propto \frac{1}{\eta^2} \tag{2.2}$$

The instrumental parameter *PL* in Topspin (the software driving the Bruker Avance III spectrometer used in this work) is related to the power of RF irradiation by the following logarithmic dependence and is measured in power gain dB:

$$PL = -6 - 10lg\left(\frac{P}{P_0}\right) \tag{2.3}$$

here P_0 is the maximum power output of the RF transmitter and P is the chosen RF power. This and previous expressions allow us to determine the value proportional to the induction of the optimal magnetic field:

$$B_{opt} \propto P_{opt}^{1/2} \propto 10^{-0.05PL_{opt}} \propto \frac{1}{\eta} \tag{2.4}$$

where PL_{opt} is the value of the PL parameter at which the maximum amplitude of the spin echo signal was reached. Thus, to correct the spectrum with respect to the enhancement factor, it suffices to multiply the optimal spectrum by a calibration curve that depends solely on the experimentally controlled parameters. In this work, when recording spectra, the PL parameter was varied within 4–24 dB range with a step of 2 dB, which corresponds to varying the RF radiation power from 10^{-1} to 10^{-3} of the maximum transmitter output.

Because quadrature detection is used when recording NMR spectra, the real and imaginary components of the signal from the receiving coil can be phased such that after the Fourier transform a pure absorption signal is obtained. After obtaining the absorption spectrum from the echo signal at each point of the two-dimensional sweep over the carrier frequency and power, various methods of "assembling" the final spectrum can be applied. After different trials, we retained the method that proved to be the most stable in the presence of line shape distortions and radio frequency interference in the spectra. The absorption signal at a given frequency was integrated in a symmetrical range around its maximum in frequency space, and the value of this integral was assigned as the intensity of the NMR spectrum of the sample under study at that particular frequency and RF power.

In summary, the procedure for a typical ^{59}Co Internal Field NMR experiment was as follows:

1. Recording of the spin echo signals in every sampled frequency and RF power;
2. Obtaining a pure absorption signals in frequency space by Fourier transform, phasing and baseline correction;
3. Integrating the obtained echo spectra in an arbitrary region symmetrical around their maxima;
4. Assembling the optimal spectrum and the $B_1^{opt}(\omega)$ calibration curve;

5. Multiplying the optimal spectrum by the enhancement calibration curve in order to obtain the corrected spectrum;
6. When needed – performing additional corrections of the spectrum for the T_2 relaxation time and Boltzmann factor.

2.2 Additional characterization techniques

To control the morphology of the studied particles, high-resolution transmission electron microscopy (HRTEM) images were recorded. The experiments were performed on a JEM-2010 transmission electron microscope (Jeol, Japan) with an accelerating potential of 200 kV and a spatial resolution of 0.194 nm. TEM images were processed using the FIJI software [125]. The experiments were performed in the Boreskov Institute of Catalysis by A. Ishchenko and V. Zaikovskii.

The elemental mapping and high-angle annular dark-field scanning transmission electron microscopy (HAADF-STEM) images were recorded on a JEM-2200FS scanning transmission electron microscope (Jeol, Japan). The experiments were performed at Novosibirsk State University by V. Zaikovskii.

Specific surface area and porosity of the samples were studied using the Brunauer-Emmett-Teller (BET) adsorption of nitrogen at 77 K on a ASAP-2400 device (Micrometrics, Canada). The experiments were performed in the Boreskov Institute of Catalysis by T. Efimenko.

The chemical composition of the samples was determined using the X-ray fluorescence analysis on the ARL Perform'X device (Thermo Scientific, USA). The experiments were performed in the Boreskov Institute of Catalysis by A. Zhdanov.

Ferromagnetic resonance (FMR) spectra were recorded in the X-band on an EleXsys 500 spectrometer (Bruker, USA) equipped with an ER4114HT high-temperature resonator. The recording was carried out in the continuous sweep mode with modulation with an amplitude of 4 Oe and a frequency of 100 kHz. The sample was placed in a 2 mm quartz tube to reduce the effect of conductivity on the quality factor of the resonator, which made it possible to carry out quantitative measurements. The experiments were performed in the Boreskov Institute of Catalysis by S. Trukhan.

2.3 Sample synthesis

The details of the sample synthesis are provided separately in each chapter.

2.4 References

[1] J. Schindelin *et al.*, "Fiji: an open-source platform for biological-image analysis," *Nat. Methods*, vol. 9, no. 7, pp. 676–682, Jul. 2012.

Chapter 3: Superparamagnetic behavior of Co nanoparticles supported by multi-walled carbon nanotubes

3.1 Introductory comments

The main advantage of the ^{59}Co Internal Field NMR technique is the large the amount of structural and morphological information contained in the spectra. It informs about the crystal structure of the studied particles as well as their magnetic composition. Moreover, ^{59}Co IF NMR spectra reflect the entirety of the ferromagnetic part of the bulk sample providing thus the full distribution of the parameter of interest (particle size, crystalline structure for example), as compared electron microscopy techniques whose responses are statistically limited by their local character.

At the same time, the wealth of potential information contained in an IF NMR spectrum is a mixed blessing since it is difficult to disentangle one effect from the other (hyperfine and demagnetizing fields for example). Indeed, the absence of a principal direction in the experiment (as opposed to the Zeeman $\mathbf{B_0}$ direction in "conventional" NMR experiment) as well as the extremely quick T_1 and T_2 relaxation times, limit to a great extent the possibility to use any kind of sophisticated interactions manipulation both in the physical and in the spin spaces. Consequently, the separation of the different contributions to the ^{59}Co IF NMR spectra is very limited. The most straightforward approach for overcoming this limitation is to displace the difficulty by synthesizing model compounds in which one of the contributions can be considered dominant.

The article presented in this Chapter is thus devoted to the study of a model sample comprised of small cobalt nanoparticles located inside multi-walled carbon nanotubes (MWCNT). The narrow inner diameter of the MWCNTs and small concentration of metallic cobalt led to a relatively narrow particle size distribution with particle sizes close to the limit of ferromagnetic-superparamagnetic transition at room temperature. Thus, this sample may be considered a good candidate for studying the effect of Co particle sizes on the ^{59}Co Internal Field NMR spectra. According to the Néel model of superparamagnetic relaxation (Eq. 1.33), the critical size at which the particle undergoes a superparamagnetic-ferromagnetic transition decreases with the decreasing temperature. Thus, the ^{59}Co NMR experiments in this article were conducted at room temperature and at 30 K in order to compare the spectral intensities and detect superparamagnetic particles. Additional methods such as TEM and ferromagnetic resonance spectroscopy were used to supplement the data obtained by NMR.

3.2 Superparamagnetic behaviour of metallic Co nanoparticles according to variable temperature magnetic resonance

This part of the thesis was published as

Ilya V. Yakovlev et al., "Superparamagnetic Behaviour of Metallic Co Nanoparticles According to Variable Temperature Magnetic Resonance," *Physical Chemistry Chemical Physics* 23, no. 4 (2021): 2723–30.

https://doi.org/10.1039/D0CP05963C.

Ilya V. Yakovlev,[a, b, c] Stanislav S. Yakushkin,[a] Mariya A. Kazakova,[a] Sergey N. Trukhan,[a] Zoya N. Volkova,[d] Alexander P. Gerashchenko,[d] Andrey S. Andreev,[e] Arcady V. Ishchenko,[a] Oleg N. Martyanov,[a] Olga B. Lapina [a, b] and Jean-Baptiste d'Espinose de Lacaillerie [*c]

a. *Boreskov Institute of Catalysis SB RAS, 5 Pr. Lavrentieva, 630090, Novosibirsk, Russia.*
b. *Novosibirsk State University, 1 Pirogova, 630090, Novosibirsk, Russia.*
c. *SIMM, ESPCI Paris, Université PSL, CNRS UMR 7615, 10 Rue Vauquelin, 75005, Paris, France.*
d. *Mikheev Institute of Metal Physics UB RAS, 18 S. Kovalevskoi, 620990, Ekaterinburg, Russia*
e. *Total Research and Technology Feluy (TRTF), Zone Industrielle C, 7181 Feluy, Belgium*

3.2.1 Abstract

Investigating the size distributions of Co nanoparticle ensembles is an important problem, which has no straightforward solution. In this work, we use the combination of ^{59}Co internal field nuclear

magnetic resonance (^{59}Co IF NMR) and ferromagnetic resonance (FMR) spectroscopies on a metallic Co nanoparticle sample with a narrow Co nanoparticle size distribution due to encapsulation within the inner channels of carbon nanotubes. High-resolution transmission electron microscopy (TEM) images showed that the nanoparticles can be represented as prolate spheroids, with the majority of particles having an aspect ratio between 1 and 2. This observation has increased the accuracy of superparamagnetic blocking size calculations from Néel relaxation model by introducing the actual volume of the ellipsoids taken from the image processing. ^{59}Co IF NMR and FMR experiments conducted under different temperatures allowed us to observe the thermal blocking of superparamagnetic particles in full accordance with the TEM particle volume distribution. This proved that these magnetic resonance techniques can be used jointly for characterization of Co nanoparticles in the bulk of the sample.

3.2.2 Introduction

Cobalt nanoparticles and composite materials based on them are extensively studied and have already found applications in various scientific and industrial fields including catalysis[1-5], electromagnetic absorptive materials[6,7], energy storage materials[8-10], and medicine[11,12]. The usage properties of an ensemble of Co nanoparticles depend on their size, morphology, crystalline and magnetic structures, properties that may actually all be connected to each other. They also depend on the particle size distribution of the ensemble and on interparticle interactions[13-15]. Thus, predicting the particles' morphology and crystalline structure in specific synthesis conditions is of crucial importance for their successful application.

The main characterization techniques that can be used for studying Co nanoparticles include X-Ray diffraction (XRD), transmission electron microscopy (TEM), scanning probe microscopies, magnetic resonance techniques (ferromagnetic resonance (FMR)[16,17] and ^{59}Co internal field nuclear magnetic resonance (^{59}Co IF NMR)[18-22]). All these techniques have their advantages and disadvantages. The application of XRD is limited for very small or defective nanoparticles due to diffraction pattern broadening; local microscopic techniques characterize a very small fraction of the sample, which is not always representative of its entirety. FMR and ^{59}Co IF NMR techniques are particularly dependent on the particle size distributions. Small superparamagnetic particles give rise to a very sharp signal in FMR, sometimes making large ferromagnetic particles indistinguishable. On the contrary, ^{59}Co IF NMR provides information only about particles large enough to be ferromagnetic and mostly about the biggest ones due to the volumetric origin of the signal and higher enhancement factor.

Recently, Liu et al.[22] have proposed a technique of temperature differential nuclear ferromagnetic resonance (TDFNR) that allows to "cut out" a narrow part of the distribution and study it separately by subtracting ^{59}Co IF NMR spectra recorded at different temperatures. This technique is based on the thermally induced ferromagnetic to superparamagnetic transition. Above a given temperature, particles smaller than a certain critical size experience thermal "flips" of magnetization during the experimental time and become invisible by ^{59}Co IF NMR. However, to efficiently employ this technique for particles a few nanometers in size one needs to be able to achieve very low temperatures (liquid helium temperature), which may not be achievable with every experimental setup or too expensive due to the high price of liquid helium. Thus, we have turned our attention to another spectroscopic technique – ferromagnetic resonance (FMR). Even though it cannot provide full information on the structure of the particles, its sensitivity can be three orders of magnitude higher, since in this case the electronic spin magnetization is probed directly.

In this work, we have attempted to simultaneously apply ^{59}Co IF NMR and FMR to investigate Co nanoparticles contained inside multi-walled carbon nanotubes (MWCNTs) and establish the application limits of both methods. In our previous works[23,24], factors which affect the formation of Co nanoparticles in the MWCNTs structure such as CNT dimensions, impregnation solution concentration and post-synthetic acidic treatment, were discussed in detail. Herein, we could thus concentrate on Co/MWCNT samples containing metallic Co nanoparticles localized inside the MWCNT channels. ^{59}Co IF NMR experiments performed at room temperature and at 30 K, and FMR experiments performed at elevated temperatures up to 600 K, provided the data on the blocking temperatures from which the critical sizes for superparamagnetic behaviour of encapsulated particles could be estimated. These results were efficiently compared with the particle size distribution obtained using high-resolution TEM.

3.2.3 Experimental

3.2.3.1 Co/MWCNT hybrid material synthesis

Multi-walled carbon nanotubes with specific structural properties and morphology were synthesized using a well-established procedure already described in detail by some of us elsewhere[25]. In brief, the catalytic chemical vapor deposition technique was employed for the growth of nanotubes via pyrolysis of ethylene on the surface of Fe-Co catalyst at 680 °C. The needed morphology of MWCNTs was obtained by using Al_2O_3-supported catalyst with 30 wt.% of the active component. The

catalyst residues were removed by boiling the obtained MWCNTs in a solution of 15% hydrochloric acid for 4 hours with continuous stirring. After that, the MWCNT samples were washed with distilled water until the suspension reached a neutral pH value. The purity of MWCNTs obtained after the acid purification was 99.7% (as determined by X-ray fluorescence analysis). After that, the nanotubes were treated with concentrated nitric acid for 2 hours to create openings and defects on their surface in order to facilitate Co deposition.

According to high-resolution transmission electron microscopy (HRTEM) data (Fig. 3.1), the obtained nanotubes were built up of 5-7 carbon monolayers with the inner and outer diameters (ID and OD, respectively) of the tubes amounting to approximately 3.9 nm and 7.2 nm correspondingly. Using the method of acid-base titration described by Boehm[26] the content of COOH groups in oxidized MWCNT was determined and measured to be 2.7 units per nm^2. The specific surface area of oxidized MWCNTs was 360 m^2/g.

Co nanoparticles were deposited inside the MWCNTs by incipient wetness impregnation with an aqueous solution of $Co(NO_3)_2 \cdot 6H_2O$ (98%, Sigma-Aldrich) and subsequent reduction under H_2 flow. The procedure for preparing of Co/MWCNT samples was described in detail earlier[23,24]. The resulting sample contained 4.2 wt.% of Co (as determined by X-ray fluorescence analysis). For further studies by ^{59}Co IF NMR and FMR, the reduced samples were transferred to ampoules that were sealed without contact with air immediately after the reduction procedure.

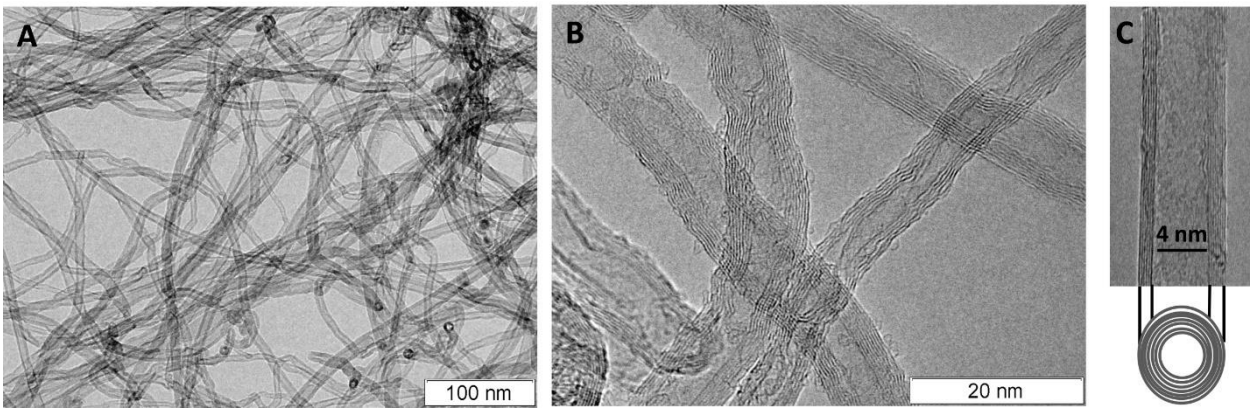

Figure 3.1. HRTEM micrographs of the oxidized carbon nanotubes (A-B) together with a schematic side view (C).

3.2.3.2 Characterization techniques

BET surface area was measured by nitrogen adsorption at 77 K using an ASAP-2400 Micromeritics instrument.

X-ray fluorescent analysis was performed on an ARL Perform'X (Thermo Scientific) equipped with a rhodium anode. Elemental content was estimated using a standardless UniQuant procedure[27].

High-resolution transmission electron micrographs (HRTEM) for statistical analysis were recorded using JEM-2010 microscope (Jeol, Japan) with acceleration voltage of 200 kV and spatial resolution of 0.194 nm. HRTEM data was analyzed using FIJI software package.

^{59}Co Internal Field Nuclear Magnetic Resonance (^{59}Co IF NMR) experiments were performed using a Bruker Avance III spectrometer and a home-built probe in the absence of external magnetic field. The experiments were conducted at 30 K and 300 K to differentiate the signal of the particles according to their blocking temperature[28]. A custom-built auto-tuning device was used to avoid the time-consuming procedures of manual tuning and matching. A θ-τ-θ echo sequence was used for broadband excitation with a θ pulse length of 1 μs and a 6 μs interpulse delay. The echo signals were recorded varying the carrier frequency stepwise each 500 kHz to cover the entire spectral width. After performing Fourier transform, phase and baseline corrections, the real parts of obtained echo signals were integrated. The results of the integration were then assigned as the intensities of the signal at each frequency. The spectra were also recorded with several different power levels of RF irradiation according to the established procedure for obtaining quantitative ^{59}Co IF NMR spectra[29]. The variation of temperature did not cause any significant Q factor change due to the fact that the FWHM of any individual Fourier-transformed echo remained constant between 30 K and 300 K.

Ferromagnetic resonance (FMR) spectra were recorded using an X-band Bruker EleXsys 500 spectrometer equipped with ER 4114HT high-temperature cavity with digital temperature control unit BVT3000. Continuous-wave mode was employed with 4 Oe modulation at frequency of 100 kHz. For the FMR experiments, the sample was sealed in a quartz ampoule with 2 mm inner diameter after the reduction. With this diameter, the Q factor decrease due to conductivity of the sample remains negligible. Heating of the sample also led to a Q factor decrease of less than 5%. Considering this, the precision of quantitative measurements was satisfactory for all measurements.

3.2.4 Results and Discussion

3.2.4.1 High-resolution transmission electron microscopy

Figure 3.2 shows a HRTEM micrograph recorded for the Co/MWCNT hybrid material. Remarkably, all of the Co nanoparticles in the sample were found inside the carbon nanotubes. This means that the acidic treatment of the nanotubes creates enough inner channel openings for efficient Co ion penetration. The fact that the Co nanoparticles are located inside the inner channels implies the presence of strong capillary forces during Co impregnation. Since the particle shapes in the sample are not spherical, we have analysed the micrographs using a bivariate particle size distribution. The resulting distribution of particles over their long axis (C) and their short axis (A) as well as the distribution of their aspect ratios (C/A) is given in Figure 3.3. According to these data, the median aspect ratio of Co nanoparticles was equal to ~1.6. Thus, the particles in the sample were slightly elongated, confirming previous qualitative observations[24].

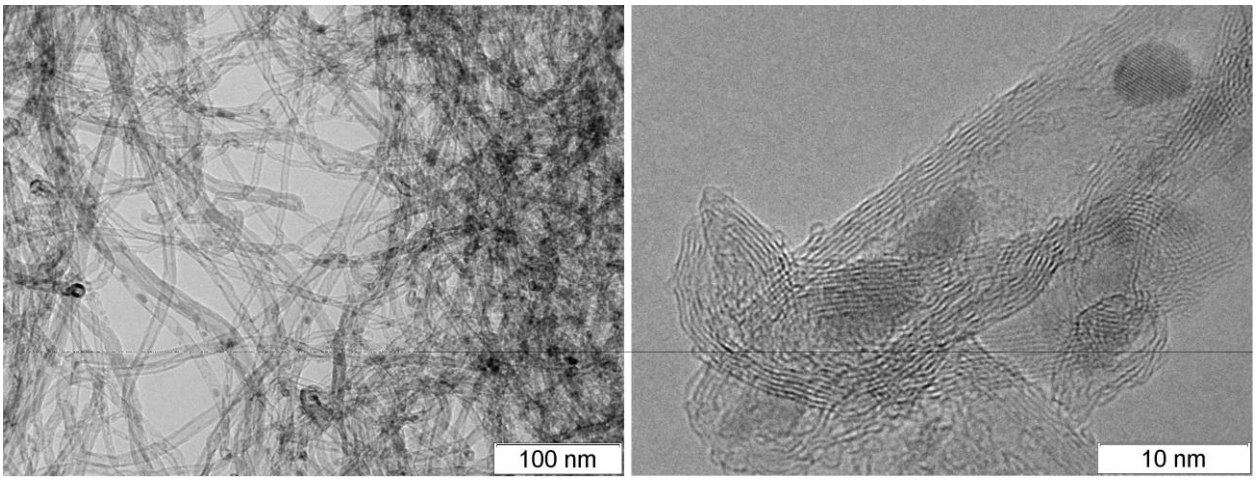

Figure 3.2. HRTEM micrographs of the Co/MWCNT hybrid material taken at different magnifications. Co nanoparticles are visible as dark grey areas.

HRTEM data proved that the Co particles were not spherical, thus we propose using a non-spherical model for the correct determination of particle volumes. Indeed, because of the axial symmetry imposed by the confinement within the carbon nanotubes, they can be represented as prolate spheroids. Taking this into account results in a realistic particle volume distribution (Fig. 3.4), which

is the physically relevant property when considering effects related to magnetic ordering of the material.

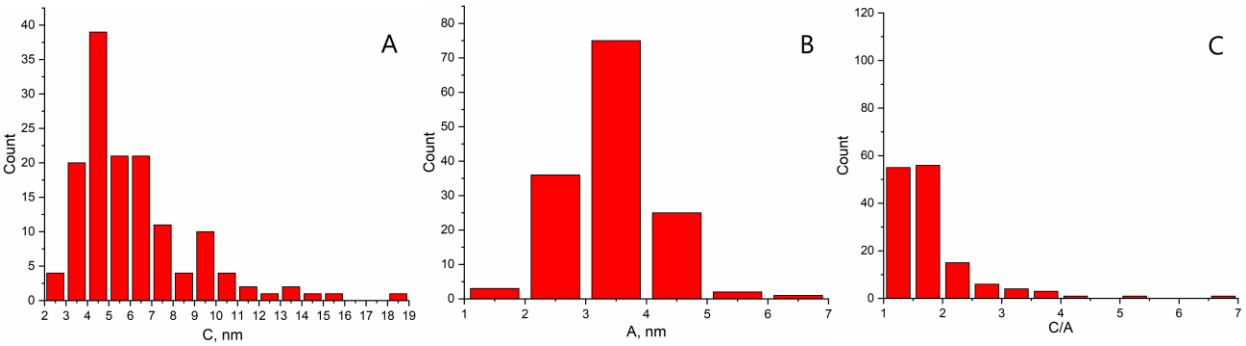

Figure 3.3. Left – distribution of particle long axes (C), middle – distribution of particle short axes (A), right – distribution of particle aspect ratios (C/A).

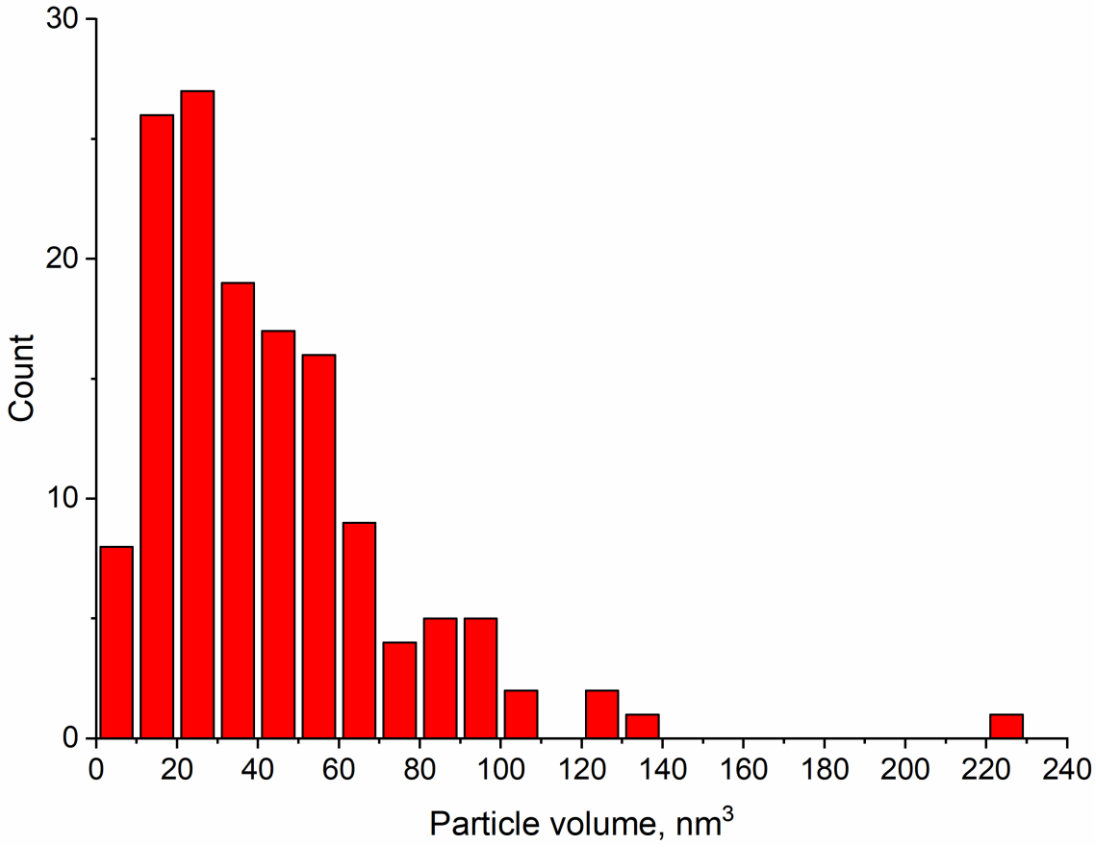

Figure 3.4. Co nanoparticle volume distribution obtained from the experimental A and C axes distributions provided by HRTEM.

3.2.4.2 ^{59}Co IF NMR and FMR

The ^{59}Co IF NMR response of a ferromagnetic particle depends on its size among other factors. In large multi-domain particles, Co nuclei located inside the domains and domain walls experience two different mechanisms of RF field enhancement leading to a drastic increase of the signal originating from and near domain walls[30,31]. When a Co particle is small enough that the energy barrier of domain wall creation becomes too high, the conservation of single magnetic domain becomes more energetically favorable (a commonly reported value for the multi-/single-domain limit at RT is 70 nm for a spherical particle[32]). The resonance frequency of Co inside a single domain particle increases with respect to the one of Co in a multidomain particle, due to the presence of uncompensated demagnetization field, which is aligned parallel to the hyperfine field[18]. Finally, when the size of the particle is small enough that its magnetic anisotropy energy becomes comparable to the thermal energy, the characteristic time of random "flips" of the magnetization that occur due to thermal fluctuations may become smaller than the characteristic time of the experiment (usually tens of microseconds in NMR). That leads to a complete loss of NMR signal, since the spin quantum states at the start of the experiment and at its end are different (thus averaging the magnetization to zero during the time of experiment). Such state of particles is called superparamagnetic, and the critical volume V of the particle, above which its magnetization becomes "blocked" during the experimental observation time at a given temperature T_B is described by the Arrhenius-type Equation (3.1) originally proposed by Néel[33]:

$$KV = k_B T_B ln\left(\tau_m / \tau_0\right) \qquad (3.1)$$

here k_B is the Boltzmann constant, K is the anisotropy constant of the material ($5*10^6$ erg*cm^{-3} for hcp Co), τ_m is the characteristic measurement time, and τ_0 is the characteristic "flipping attempt" time (usually considered to be between 10^{-9} and 10^{-12} s)[34]. The volume dependence of the blocking temperature expressed in Eq (3.1) is the basic principle underlying the determination of particle size distribution by ^{59}Co IF NMR. Any given temperature corresponds to a critical volume above which particles are ferromagnetic. ^{59}Co IF NMR signal intensity at a given temperature is thus proportional to the total volume of particles larger than the corresponding critical volume among other factors. Consequently, collecting the ^{59}Co IF NMR spectra at different temperatures allows reconstructing in principle a volume size distribution. This procedure is based on the assumption that Equation (3.1) derived for spherical particles constitutes a valid approximation when the particles aspect ratio is not too high (as opposed for example to particles in [24], where their high aspect ratio provides for a considerable magnetic shape anisotropy).

The fact that ^{59}Co IF NMR depends on particle sizes can be illustrated by comparing the room temperature ^{59}Co IF NMR spectra of three samples with similar Co content but different particle sizes (Fig. S2). In the sample of the present study (ID ≈ 4 nm nm, OD ≈ 7 nm), the Co nanoparticles are located inside carbon nanotube channels and are thus limited in size. The nanotubes of higher OD (9 and 18 nm) contained the bigger Co nanoparticles located inside the inner channels (Id ≈ 4 and 7 nm, respectively) and on the outer surface. For the smallest OD = 7 nm, the majority of the Co particles were undetectable by ^{59}Co IF NMR as their state is superparamagnetic at RT and at the NMR timescale. The NMR intensity was thus considerably smaller than for the ones in MWCNT of bigger OD. Indeed, in the approximation of spherical particles in the absence of substantial magnetic shape anisotropy using a characteristic time for ^{59}Co IF NMR experiment of about 20 μs and τ_0 of 10^{-10} s, we can estimate from Eq. 3.1 the room temperature superparamagnetic limit (critical diameter of a spherical particle corresponding to the blocking volume V) to be D_{crit} = 5.8 nm.

The ^{59}Co IF NMR spectrum taken at 30 K displays a much higher intensity and was shifted toward higher frequencies compared to the room temperature spectrum (Fig. 3.5). Bloch's law for spontaneous magnetization explains such increase of resonance frequency, while the intensity increased according to Boltzmann distribution. However, after taking both of these factors together with the change of T_2 relaxation time (for more information on T_2 measurement see Supplementary) into account for a quantitative comparison of signal intensities, the amplitude of the 30 K spectrum at 216.5 MHz (resonant frequency of single-domain fcc Co particles) remained about 40 times higher (Fig. 3.5, red). This can be explained by the additional superparamagnetic Co particles that have undergone blocking into ferromagnetic state with the decrease in temperature.

At 30 K, the estimate of the critical particle size given by Eq. 1 is 10 nm^3. However, the actual critical volume may be somewhat bigger than estimated from Eq. (3.1) due to magnetic anisotropy associated with the slight non-sphericity of the particles and surface effects. To account for these morphological effects, Liu et al.[22] have used an empirical 2.5 multiplier on the diameter for the critical blocking size predictions in order to match them to TEM observations.

However, in our work, the critical size limits seemed to coincide well with the results for particle size distribution obtained by TEM, i.e. the particles with volumes between 10 and 100 nm^3 (which should become "blocked" in ^{59}Co IF NMR experiment with decrease in temperature from 300 K to 30 K) correspond to the major part of cobalt volume determined from the HRTEM data. Therefore, we assumed that the increase of signal intensity did indeed arise from magnetic blocking of the majority

of nanoparticles in the sample. Thus, for the considered aspect ratios (Fig. 3.3), the spherical assumption remained valid.

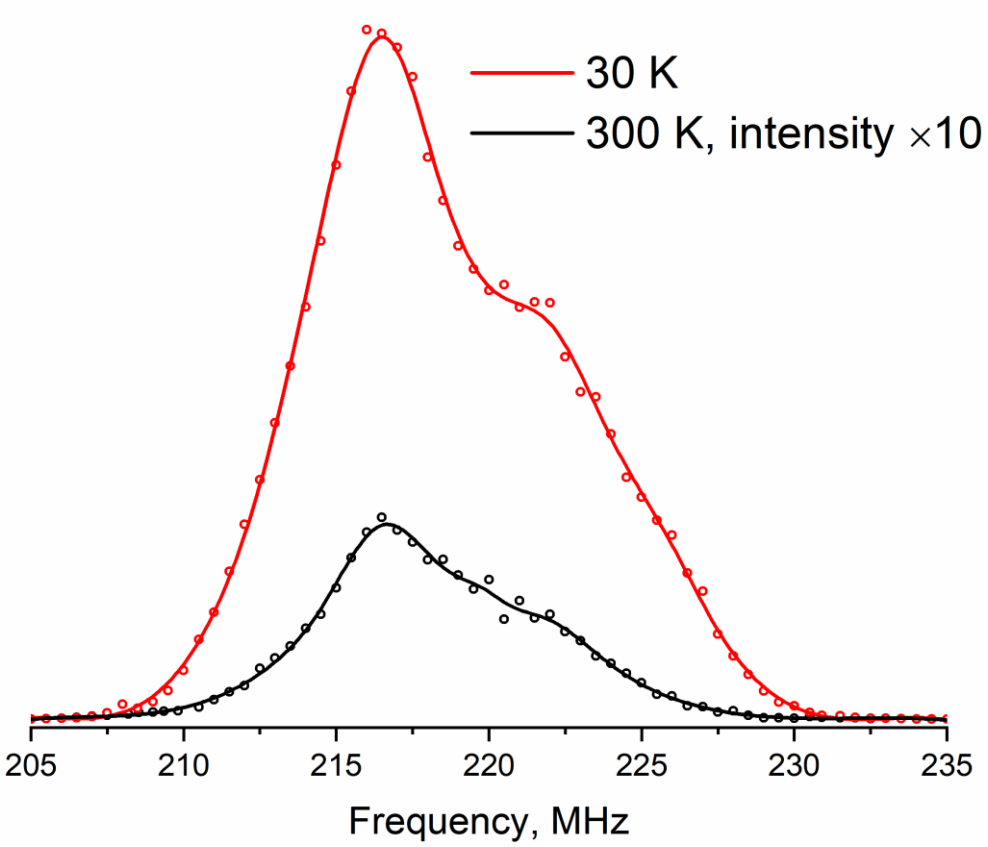

Figure 3.5. ^{59}Co IF NMR spectra of Co/MWCNT material recorded at room temperature (black, intensity multiplied by a factor of 10 for clarity) and 30 K (red) corrected for the temperature dependence of resonance frequency and amplitude. Experimental points are depicted with circles; interpolated lines are drawn for clarity. The 30 K spectrum is shifted into the lower frequency by about 5 MHz to account for the resonance frequency shift caused by the increase of the spontaneous magnetization according to the Bloch's law. The spectral intensities were corrected to account for Curie's law and relaxation time difference.

Apart from particle size considerations given by the analysis of spectra intensity, ^{59}Co IF NMR also provides the information on the magnetic and crystalline structures of the particles. In line with previously published assignments[21], the spectrum recorded at 30 K exhibited a typical line shape, consisting of a Pseudo-Voigt profile at 216.5 MHz that corresponds to single-domain fcc-Co particles and a complex line shape corresponding to hcp-Co phase (219-225 MHz). The latter line could also

correspond to stacking faults in fcc-Co packing since they are indistinguishable from hcp-Co. This together with the magnetocrystalline anisotropy makes the line corresponding to hcp-Co much wider compared to fcc-Co[35,36]. No well-defined resonances at 213 MHz corresponding to domain walls occurring in multi-domain Co particles were present in the spectrum, which is not surprising considering the particle size distribution. A decomposition of the spectrum into a Pseudo-Voigt line corresponding to fcc-Co and the remaining signal obtained by subtracting the fcc-Co line from the spectrum resulted in roughly 60% fcc-Co content. The spectrum recorded at RT displayed a much weaker intensity resulting in a less reliable decomposition (possible decompositions are shown in Fig. S3). Nonetheless, the fcc-Co intensity was visibly lower compared to the 30 K spectrum, which is consistent with the fact that hcp packing stability increases with the nanoparticle size increase[37].

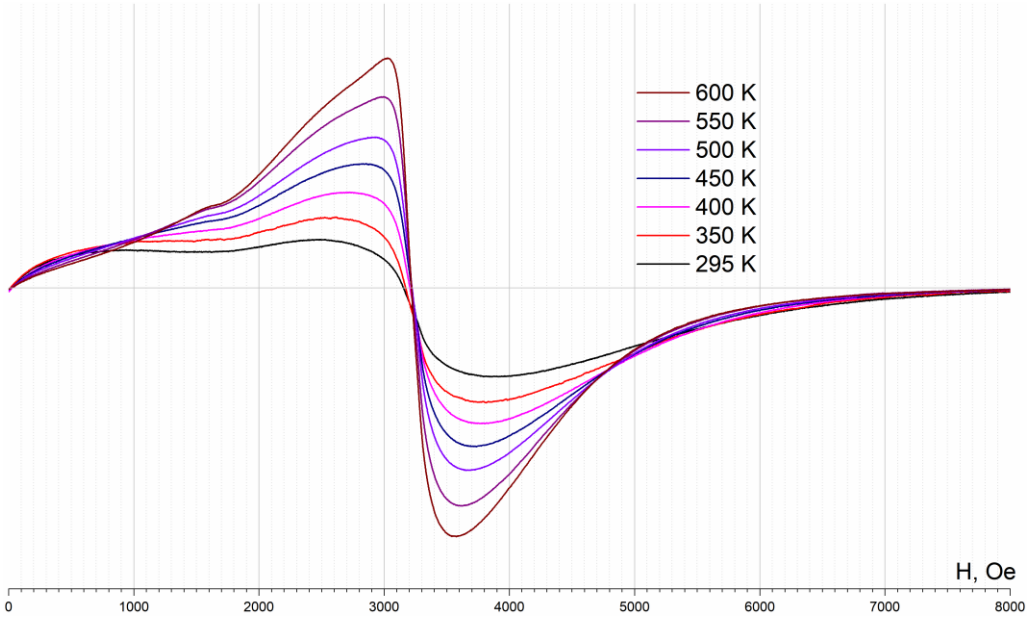

Figure 3.6. FMR spectra of Co/MWCNT hybrid material taken at various temperatures. The intensity of the resonant components of the signal grows due to gradual unblocking of ferromagnetic particles and due to narrowing of the signal caused by temperature increase.

In order to further investigate superparamagnetic particles in the sample, a series of ferromagnetic resonance (FMR) spectra at room and elevated temperatures were recorded (Fig. 3.6). At room temperature, there was a broad asymmetric signal in FMR spectrum, with two notable features. The absorption in the high-field region (2000-5000 Oe) can be attributed to the single-domain ferromagnetic nanoparticles interacting with the microwave radiation. The absorption by

ferromagnetic particles in the low-field region (0-1000 Oe) is often considered non-resonant. Thus, the origin of that part of the signal is rather complex and difficult to simulate.

With the temperature increase, both the low-field and high-field signals changed. A narrow intense line appeared in the high-field region at 3200 Oe starting from 400 K. When the temperature rose, the high-field line narrowed, followed by a low-field signal intensity decrease. These effects resulted from the superparamagnetic behaviour of Co nanoparticles: with the temperature increase, more nanoparticles exhibited superparamagnetic behaviour resulting in the increase of the narrow component. Simultaneously, the signal in the low-field region decreased since temperature fluctuations unblocked the magnetic moments of nanoparticles.

To analyze the superparamagnetic transition of the Co nanoparticles with the temperature change, the high-field part of the signal was simulated (Fig. 3.7) as a superposition of two Lorentzian-shape absorption lines: a narrow one, corresponding to ”unblocked” nanoparticles (the double integral is called $I_{unblocked}$), and a broad one corresponding to “blocked” nanoparticles (the double integral is called $I_{blocked}$). The double integral of the narrow component is growing together with the temperature increase, supporting the idea of superparamagnetic nature of the signal (Fig. S4).

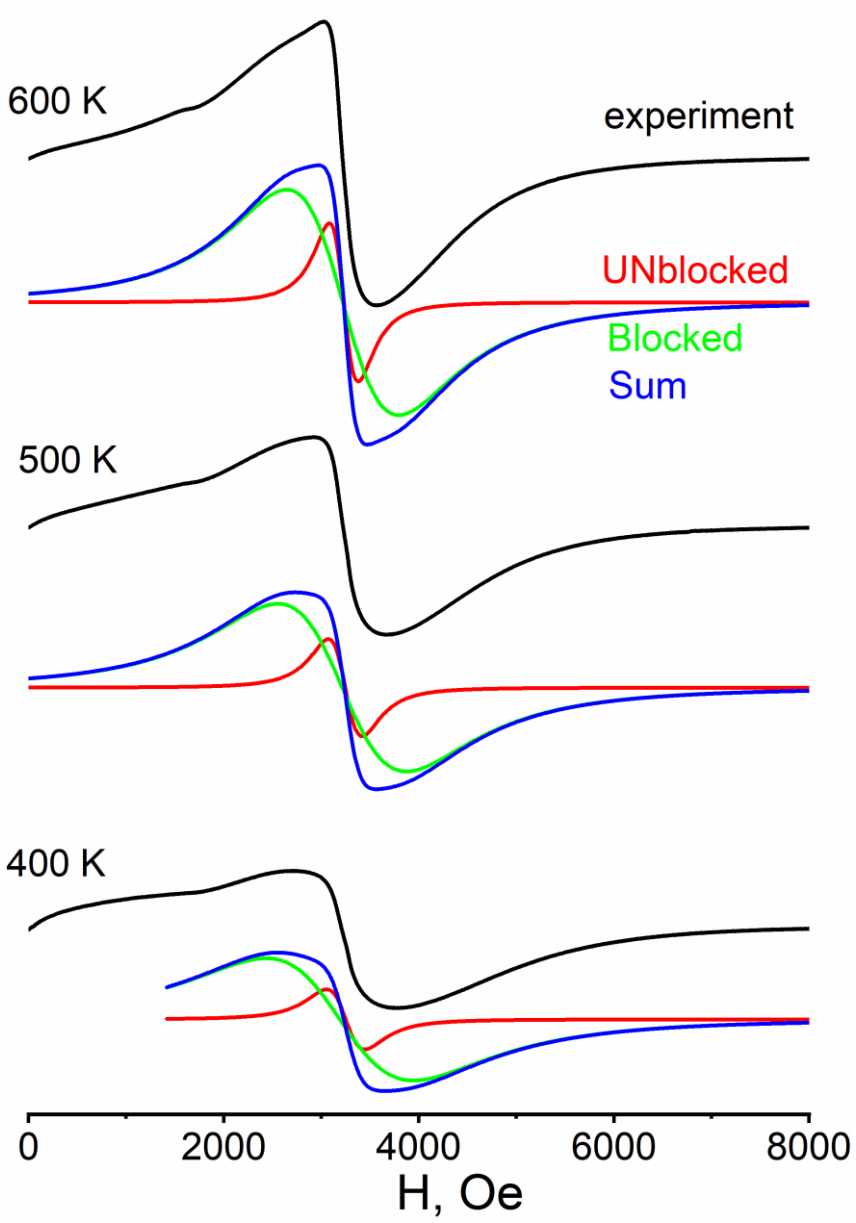

Figure 3.7. Experimental FMR spectra (black) at several chosen temperatures along with the simulated lines (shown in color). Red line represents the unblocked superparamagnetic nanoparticles; green line represents the blocked ferromagnetic particles; blue line is the sum of two simulated lines.

3.2.4.3 Critical size calculations

Based on the $I_{unblocked}/I_{blocked}$ ratio from the experimental FMR spectra, it is possible to choose the cut-off volume *(x)* such that the ratio between the total volumes of particles with $V < x$ and of particles with $V > x$ is equal to $I_{unblocked}/I_{blocked} = 0.05$, the ratio observed in FMR at 600 K. The obtained value of x in this case is 17 nm^3. Thus, the critical volume V of a Co nanoparticle for FMR spectroscopy

at 600 K is 17 nm^3. Since the FMR experiments were performed using X-band spectrometer, the characteristic measuring time τ_m can be estimated as 10^{-10} s. These experimental values provided an estimate of the thermal relaxation time τ_0 using the Neel equation (Eq. 3.1) as:

$$\tau_0 = \tau_m(FMR) * \exp\left(\frac{-KV}{k_B T_B}\right) = 3.55 * 10^{-11} s$$

which is in reasonable agreement with the commonly reported values of 10^{-9} to 10^{-12} s[34].

Furthermore, this value of the critical volume of 17 nm^3 observed at 600 K (FMR, 600K) allowed us to predict using Néel equation (Eq. 3.1) the value of the critical volume at 300 K (FMR, 300 K) as:

$$V(FMR, 300\ K) = \mathrm{V}(FMR, 600\ K) * \left(\frac{300\ K}{600\ K}\right) = 9\ nm^3$$

Then, following the same logic using (Eq. 3.1) and using the thermal relaxation time τ_0 obtained by FMR, we can estimate the critical volumes for ^{59}Co IF NMR spectroscopy at 300 K V(NMR, 300 K) and 30 K V(NMR, 30 K) as follows:

$$V(NMR, 300\ K) = \mathrm{V}(FMR, 300\ K)\left(\frac{ln\left(\tau_{NMR}/\tau_0\right)}{ln\left(\tau_{FMR}/\tau_0\right)}\right) = 220\ nm^3$$

$$V(NMR, 30\ K) = V(NMR, 300\ K) * \left(\frac{30\ K}{300\ K}\right) = 22\ nm^3$$

The obtained values of V_{crit} for NMR spectroscopy differ from the predictions made earlier (10 nm^3 at 30 K and 100 nm^2 at 300 K) by a factor of about 2, but nonetheless, this range still covers the major part of the sample volume as determined from the cumulative volume graph (Fig. 3.8). According to these values, particles corresponding to 89% of total Co volume become thermally blocked in the 30 K - 300 K temperature range, which is consistent with the significant intensity increase on the ^{59}Co IF NMR spectra.

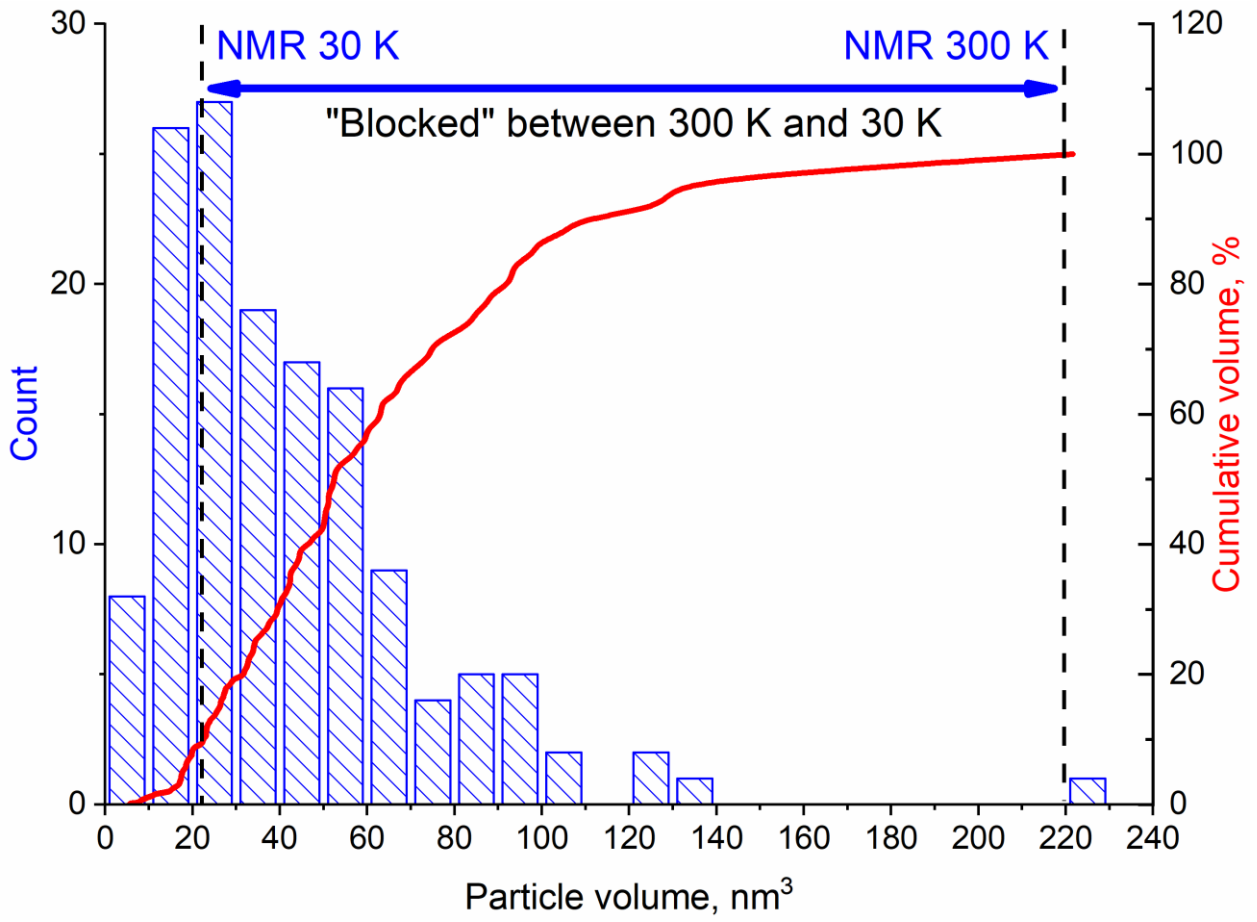

Figure 3.8. Depiction of particle blocking range for IF NMR between 300 K and 30 K. Blue bars represent the HRTEM volume distribution. Solid red line is the cumulative volume graph.

While for magnetic properties the physically relevant size is the particle volume, for most nanoparticle applications, for example supported heterogeneous catalysis, the size of interest is the linear size or the particle diameter. We thus also derived from the HRTEM data an effective spherical diameter distribution (Fig. 3.9) using:

$$D_{Eff} = \sqrt[3]{A^2 C}$$

Obviously, the particle volume varies as the cube of the effective diameter so that the later parameter is much less sensitive and the discrepancy of a factor 2 in the volumes translates in a difference of only 25% in the effective diameters. This value was significantly lower than the 250% factor used by Liu et al. on Fischer–Tropsch catalysts[22]. In our case, the combination of FMR and ^{59}Co IF NMR performed thus satisfactorily to characterize all Co particles from the linear size distribution

given by HRTEM images analysis. This might be due to the better defined spheroidal geometry of the particles under consideration.

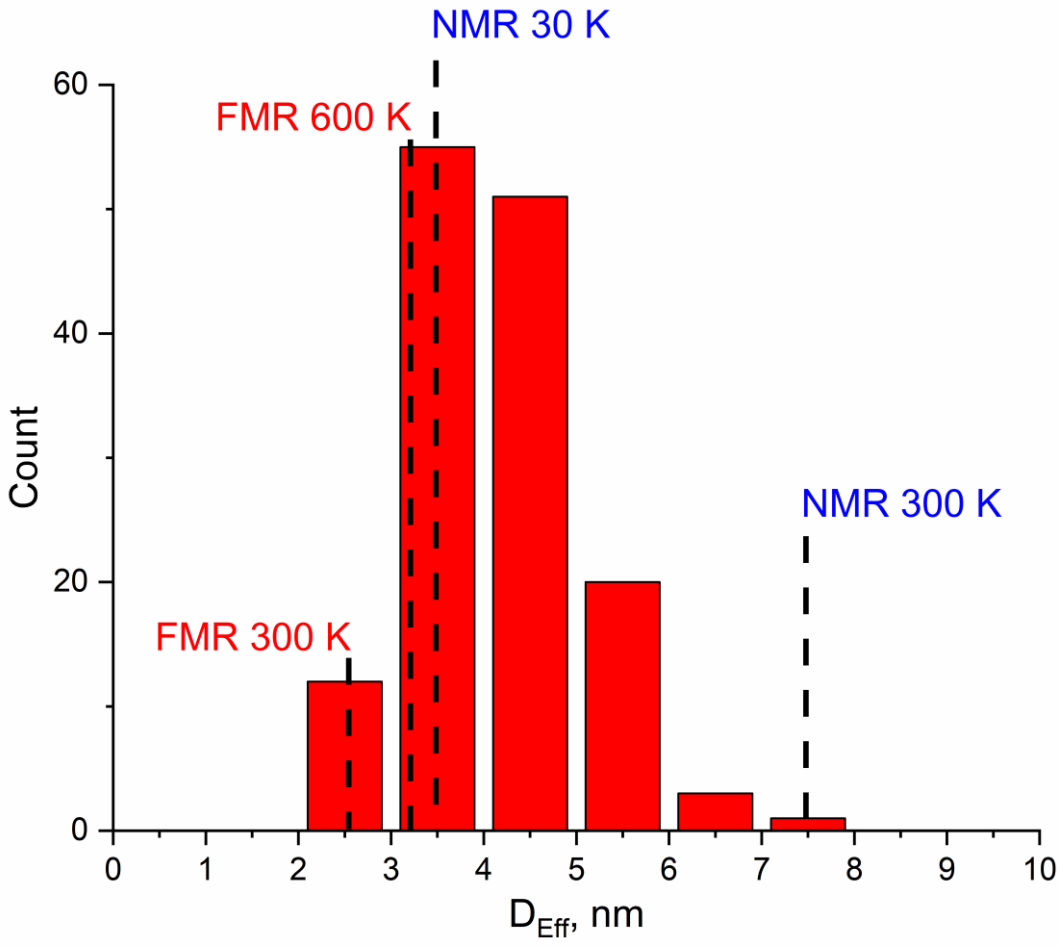

Figure 3.9. Recalculated spherical model Co nanoparticle D_{Eff} size distribution obtained from the experimental A and C axes distributions provided by HRTEM. Dashed lines represent the critical particle sizes for FMR and ^{59}Co IF NMR calculated from the obtained critical volumes.

At first glance, ^{59}Co IF NMR and FMR provide very similar information on the Co nanoparticles in the sample. However, these techniques are very different by their nature. ^{59}Co IF NMR allows observation of particles solely in ferromagnetic state, and its operational range is limited to temperatures below room temperature due to inherently low sensitivity and long experimental time. This means that all spherical particles bigger than approximately 6-7 nm contribute to the ^{59}Co IF NMR spectrum taken at room temperature. The main advantage of this technique is its capacity not only to analyze particle sizes, but also to probe the crystalline and magnetic structure of the particles.

On the other hand, both ferromagnetic and superparamagnetic particles give rise to FMR signal making this technique less particle size selective. However, distinguishing the signals in FMR is not obvious. Moreover, an imprecision of thermal relaxation time τ_0 determination at different temperatures may cause the discrepancy between the predicted and experimentally determined values of blocking sizes for ^{59}Co IF NMR. Nevertheless, the sensitivity of FMR can be three orders higher compared to ^{59}Co IF NMR since it is the spin magnetization that is probed in this case. This facilitates doing FMR experiments at elevated temperatures, which extends the range of reachable critical blocking sizes to some extent. The probed blocking size range is indeed the main obstacle for these techniques due to a very weak dependency of the linear blocking size on the temperature (cubic root) and even weaker dependency on the measurement time (cubic root of logarithm).

3.2.5 Conclusions

Based on the image analysis by HRTEM, Co/MWCNT hybrid material possesses a relatively narrow size distribution of metallic Co nanoparticles with most of the particles being less than 6 nm in effective diameter. This was the result of particle confinement inside the channels of nanotubes that was observed on HRTEM micrographs. According to the difference between ^{59}Co IF NMR spectra recorded at 30 K and 300 K, fcc crystal structure is stabilized in Co nanoparticles smaller than 6 nm.

Using this sample, we have demonstrated that despite some experimental drawbacks, ^{59}Co IF NMR and FMR are two complementary techniques that in combination provide a very powerful and, most importantly, bulk-averaged method for structural characterization of a large range of Co particle volume distributions based on HRTEM data analysis. Due to its high sensitivity, FMR can be used for particle size distribution investigation even at elevated temperatures, which increases the number of particles in superparamagnetic state. At the same time, ^{59}Co IF NMR is a technique that provides unique information on the crystalline and magnetic structure of the particles. Moreover, the relatively long experimental time in ^{59}Co IF NMR allows putting Co nanoparticles into superparamagnetic state in a much wider size range compared to FMR. However, these techniques possess drawbacks that limit the accuracy of critical blocking size determination, namely, very low signal-to-noise ratio in ^{59}Co IF NMR and presence of non-resonant absorption signal in FMR spectra that leads to somewhat inaccurate decomposition of spectra. Furthermore, because the blocking temperature does not depend only on size but also on shape, caution must be used when discussing particle sizes using ^{59}Co IF NMR and FMR without using supplementary non-bulk techniques such as HRTEM.

3.3 Supplementary materials

T_2 measurement in IF NMR.

To account for all possible sources of intensity change due to the temperature variation we have also measured the T_2 relaxation constant for fcc-Co line at both temperatures (line located at ~216 MHz at 300 K and ~221 MHz at 30 K), as it was the most prominent line in both spectra. The T_2 constant measurement was done in a usual way by plotting the intensity of the spectrum against the varied echo delay and fitting this plot with a single mode exponential decay function. The measured T_2 constants were 15.5 μs and 23.3 μs at 300 K and 30 K correspondingly (Fig. S1). Such values make the T_2 relaxation term $e^{-2\tau/T_2}$ significant with the echo delay τ of 6 μs.

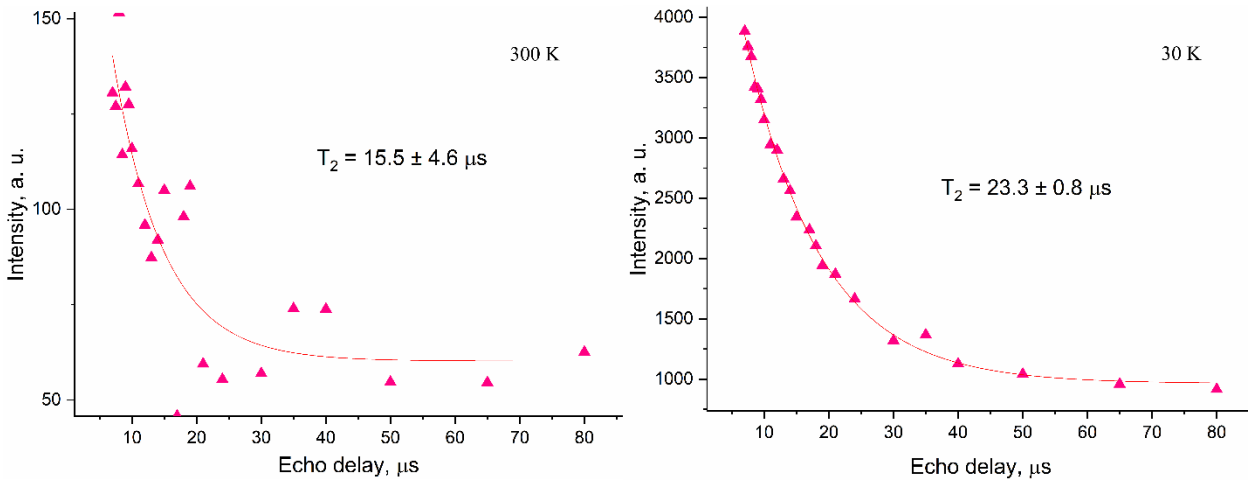

Figure S1. T_2 relaxation constant measurement results for 300 K (left) and 30 K (right) experiments. Experimental points are shown with symbols; the exponential decay approximation results are shown with solid red lines.

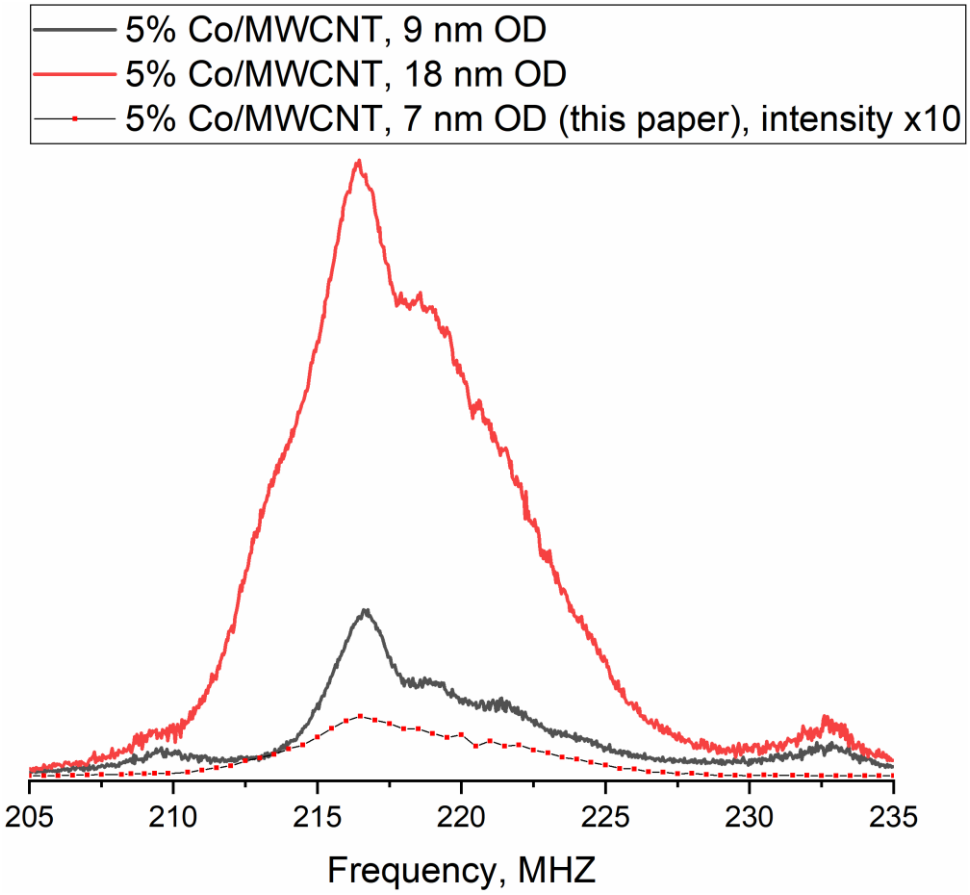

Figure S2. Comparison between room-temperature ^{59}Co IF NMR spectra of Co/MWCNT composites with similar Co weight content supported on nanotubes with different morphology (outer diameter of nanotubes is shown in the legend)

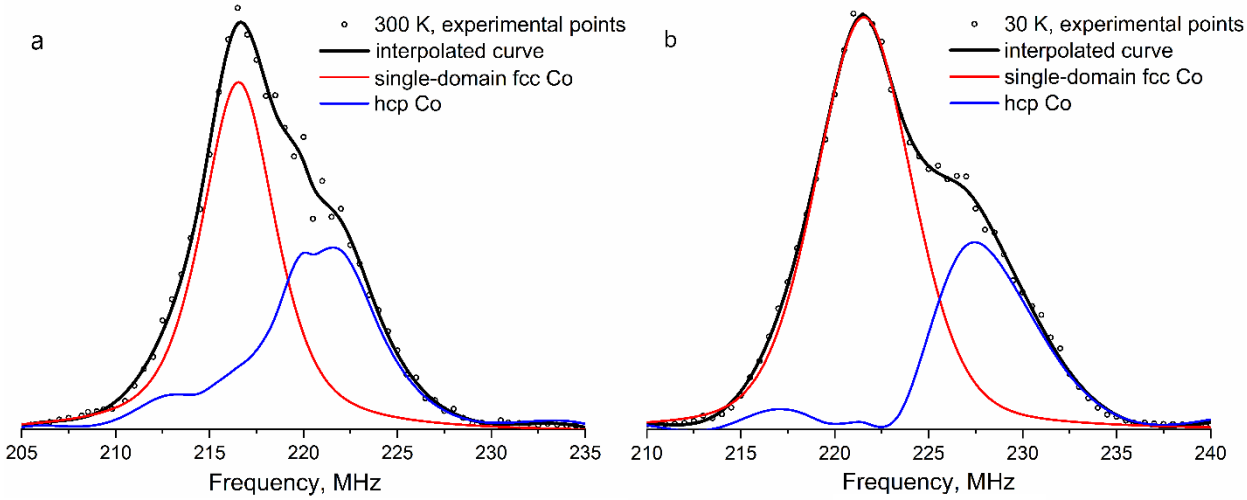

Figure S3. Possible decompositions of the experimental ^{59}Co IF NMR spectra (circles – experimental points, black line – cubic spline interpolation of the experimental points) at 300 K (a) and 30 K (b). A pseudo-Voigt profile corresponding to single-domain fcc Co is shown with red line; the blue line corresponding to hcp Co is obtained by subtracting the single-domain fcc line from the experimental spectrum.

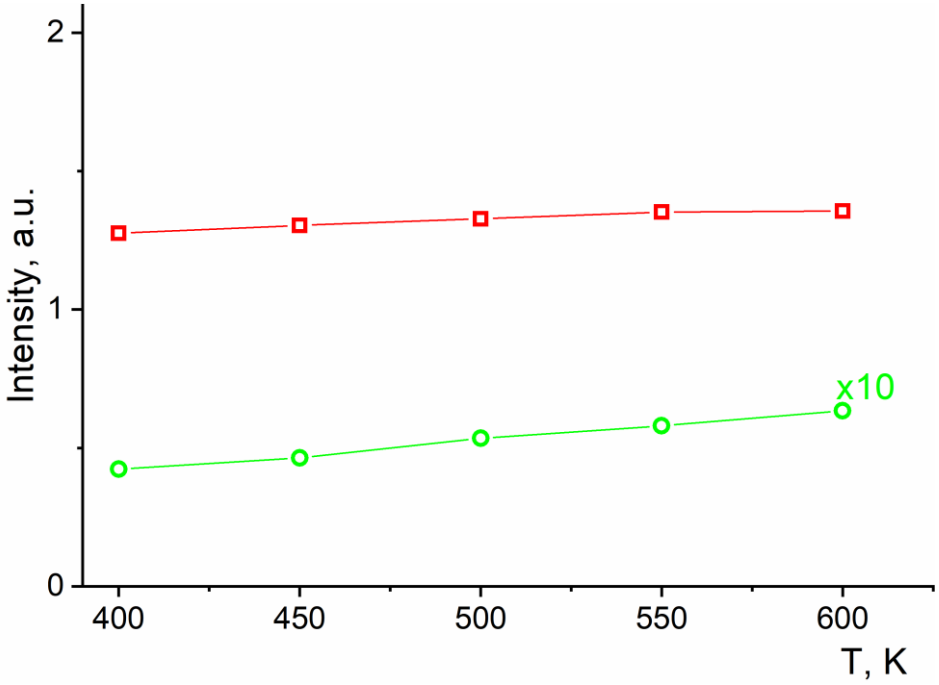

Figure S4. Intensities of the broad (red squares) and narrow (x10) (green squares) components of the FMR high-field signal depending from temperature.

3.4 Conclusion

In this Chapter, we have presented the study of cobalt nanoparticles located inside the channels of multi-walled carbon nanotubes (MWCNTs). Such a structures resulted of a careful choice of the nanotubes used as the support for Co nanoparticles. Due to the small inner and outer diameters of the employed MWCNTs as well as very low content of metallic Co, the overwhelming majority of Co nanoparticles were located inside the inner channels of the nanotubes as was evidenced using transmission electron microscopy (TEM). A detailed analysis of TEM images allowed us to build a particle volume distribution with the particles represented as prolate spheroids (such a representation was justified due to the confinement of Co nanoparticles inside the channels of the nanotubes).

The ^{59}Co Internal Filed NMR spectra of this model sample recorded at 30 K and room temperature demonstrated a significant increase of the intensity at lower temperature even after all the relevant corrections were made. This observation led us to the conclusion that a large amount of Co nanoparticles had undergone a transition from the superparamagnetic (at room temperature) to the ferromagnetic (at 30 K) state, which made them observable by NMR. In order to analyze the sizes of

the particles blocked into the ferromagnetic state, we have employed the Arrhenius-type model for superparamagnetic relaxation originally proposed by Néel.

This model contains the parameter for characteristic time of "superparamagnetic relaxation attempt" τ_0 that has a poorly determined value, and thus we tried to clarify this value by using the supplementary technique of ferromagnetic resonance (FMR). Unlike ^{59}Co IF NMR, this technique is extremely sensitive to the particles in superparamagnetic state. By decomposition of the FMR spectra into contributions from the superparamagnetic and ferromagnetic particles and comparing this data to particle volume distribution obtained by TEM we have established the value of τ_0 equal to $3.55*10^{-11}$ s. Finally, this allowed us to analyze the ^{59}Co IF NMR spectra and compare the experimentally obtained volume of the "blocked" nanoparticles to the prediction made using the Néel model on the base of TEM measurements. The resulting agreement between theory and experiment was much more precise compared to results reported earlier in literature and demonstrated that the ^{59}Co Internal Filed NMR technique can be used to analyze the particle size distribution in Co containing samples.

The work presented in this Chapter has also demonstrated the limitations of this technique. Despite its bulk character (the ability to analyze the entirety of the sample), the interpretation of ^{59}Co IF NMR spectra still rely heavily on such local techniques as electron microscopy due to inaccuracies inherent to NMR such as, for example, low signal-to-noise ratio. The results of this study have also drawn our attention to the consideration that if the sample contains a relatively wide distribution of particle sizes, the structural information obtained from the spectra must be treated with special care since, for example, the signal intensities from a 10 nm particle and 100 nm particle differ by a factor of 1000. Thus, the major part of the ^{59}Co IF NMR spectrum will reflect only a minority of large particles. This is a problem that may be resolved by using the variable temperature NMR experiment and analyzing the differential spectra that would relate to certain size intervals in particle size distribution. At the same time, for samples with very low Co content, a single temperature point may suffice for a reliable structural analysis due to the naturally narrow size distribution, as was in the case of model Fischer-Tropsch catalysts presented in **Chapter 4**.

3.5 References

1 M. O. Kazakov, M. A. Kazakova, Y. V. Vatutina, T. V. Larina, Y. A. Chesalov, E. Y. Gerasimov, I. P. Prosvirin, O. V. Klimov and A. S. Noskov, *Catal. Today*, , DOI:10.1016/j.cattod.2019.03.051.

2 R. V. Jagadeesh, K. Murugesan, A. S. Alshammari, H. Neumann, M.-M. Pohl, J. Radnik and M. Beller, *Science (80-.).*, 2017, **358**, 326–332.

3 V. Iablokov, S. A. Alekseev, S. Gryn, I. Bezverkhyy, V. Zaitsev, L. Kovarik, T. Visart de Bocarme and N. Kruse, *J. Catal.*, 2020, **383**, 297–303.

4 F. Michalek, A. Lagunas, C. Jimeno and M. A. Pericàs, *J. Mater. Chem.*, 2008, **18**, 4692.

5 X. Li, C. Zeng, J. Jiang and L. Ai, *J. Mater. Chem. A*, 2016, **4**, 7476–7482.

6 M. A. Kazakova, N. V. Semikolenova, E. Y. Korovin, S. I. Moseenkov, A. S. Andreev, A. S. Kachalov, V. L. Kuznetsov, V. I. Suslyaev, M. A. Mats'ko and V. A. Zakharov, *Russ. J. Appl. Chem.*, 2018, **91**, 127–135.

7 D. Zhang, F. Xu, J. Lin, Z. Yang and M. Zhang, *Carbon N. Y.*, 2014, **80**, 103–111.

8 M. A. Kazakova, D. M. Morales, C. Andronescu, K. Elumeeva, A. G. Selyutin, A. V. Ishchenko, G. V. Golubtsov, S. Dieckhöfer, W. Schuhmann and J. Masa, *Catal. Today*, , DOI:10.1016/j.cattod.2019.02.047.

9 R. Wang, Q. Dong, H. Wang, S. Ji, X. Wang and V. Linkov, *Chem. – A Eur. J.*, 2020, chem.201905268.

10 Z. Yan, Q. Hu, G. Yan, H. Li, K. Shih, Z. Yang, X. Li, Z. Wang and J. Wang, *Chem. Eng. J.*, 2017, **321**, 495–501.

11 P. Lukanov, V. K. Anuganti, Y. Krupskaya, A.-M. Galibert, B. Soula, C. Tilmaciu, A. H. Velders, R. Klingeler, B. Büchner and E. Flahaut, *Adv. Funct. Mater.*, 2011, **21**, 3583–3588.

12 Y. Xu, M. Mahmood, Z. Li, E. Dervishi, S. Trigwell, V. P. Zharov, N. Ali, V. Saini, A. R. Biris, D. Lupu, D. Boldor and A. S. Biris, *Nanotechnology*, 2008, **19**, 435102.

13 O. N. Martyanov, V. F. Yudanov, R. N. Lee, S. A. Nepijko, H. J. Elmers, C. M. Schneider and G. Schönhense, *Appl. Phys. A*, 2005, **81**, 679–683.

14 Y. V. Knyazev, A. I. Chumakov, A. A. Dubrovskiy, S. V. Semenov, I. Sergueev, S. S. Yakushkin, V. L. Kirillov, O. N. Martyanov and D. A. Balaev, *Phys. Rev. B*, 2020, **101**, 094408.

15 A. A. Dubrovskiy, D. A. Balaev, K. A. Shaykhutdinov, O. A. Bayukov, O. N. Pletnev, S. S. Yakushkin, G. A. Bukhtiyarova and O. N. Martyanov, *J. Appl. Phys.*, 2015, **118**, 213901.

16 S. N. Sidorov, L. M. Bronstein, V. A. Davankov, M. P. Tsyurupa, S. P. Solodovnikov, P. M. Valetsky, E. A. Wilder and R. J. Spontak, *Chem. Mater.*, 1999, **11**, 3210–3215.

17 I. S. Edelman, E. A. Petrakovskaja, D. A. Petrov, S. M. Zharkov, R. I. Khaibullin, V. I. Nuzhdin and A. L. Stepanov, *Appl. Magn. Reson.*, 2011, **40**, 363–375.

18 A. C. Gossard, A. M. Portis, M. Rubinstein and R. H. Lindquist, *Phys. Rev.*, 1965, **138**, A1415–A1421.

19 V. V. Matveev, D. A. Baranov, G. Y. Yurkov, N. G. Akatiev, I. P. Dotsenko and S. P. Gubin, *Chem. Phys. Lett.*, 2006, **422**, 402–405.

20 A. S. Andreev, O. B. Lapina and S. V. Cherepanova, *Appl. Magn. Reson.*, 2014, **45**, 1009–1017.

21 A. S. Andreev, J.-B. D'Espinose De Lacaillerie, O. B. Lapina and A. Gerashenko, *Phys. Chem. Chem. Phys.*, , DOI:10.1039/c4cp05327c.

22 Y. Liu, J. Luo, Y. Shin, S. Moldovan, O. Ersen, A. Hébraud, G. Schlatter, C. Pham-Huu and C. Meny, *Nat. Commun.*, 2016, **7**, 11532.

23 M. A. Kazakova, A. S. Andreev, A. G. Selyutin, A. V. Ishchenko, A. V. Shuvaev, V. L. Kuznetsov, O. B. Lapina and J.-B. d'Espinose de Lacaillerie, *Appl. Surf. Sci.*, 2018, **456**, 657–665.

24 A. S. Andreev, M. A. Kazakova, A. V. Ishchenko, A. G. Selyutin, O. B. Lapina, V. L. Kuznetsov and J.-B. d'Espinose de Lacaillerie, *Carbon N. Y.*, 2017, **114**, 39–49.

25 M. A. Kazakova, V. L. Kuznetsov, S. N. Bokova-Sirosh, D. V. Krasnikov, G. V. Golubtsov, A. I. Romanenko, I. P. Prosvirin, A. V. Ishchenko, A. S. Orekhov, A. L. Chuvilin and E. D. Obraztsova, *Phys. status solidi*, 2018, **255**, 1700260.

26 H. P. Boehm, *Carbon N. Y.*, 1994, **32**, 759–769.

27 A. Zhdanov and M. Kazakova (Shuvaeva), *J. Anal. Chem.*, 2020, **75**, 239–247.

28 Y. Liu, B. de Tymowski, F. Vigneron, I. Florea, O. Ersen, C. Meny, P. Nguyen, C. Pham, F. Luck and C. Pham-Huu, *ACS Catal.*, 2013, **3**, 393–404.

29 P. Panissod, J. P. Jay, C. Meny, M. Wojcik and E. Jedryka, *Hyperfine Interact.*, 1996, **97**–**98**, 75–98.

30 I. S. Oliveira and A. P. Guimarães, *J. Magn. Magn. Mater.*, 1997, **170**, 277–284.

31 M. B. Stearns, *Phys. Rev.*, 1967, **162**, 496–509.

32 D. L. Leslie-Pelecky and R. D. Rieke, *Chem. Mater.*, 1996, **8**, 1770–1783.

33 L. Neel, *Ann. Geofis.*

34 L. M. Liz-Marzán, M. Giersig and N. A. T. O. S. A. Division, Springer Netherlands, 2003.

35 R. M. Bozorth, *Phys. Rev.*, 1954, **96**, 311–316.

36 D. S. Rodbell, *Phys. Phys. Fiz.*, 1965, **1**, 279–305.

37 S. Ram, *Mater. Sci. Eng. A*, 2001, **304**–**306**, 923–927.

Chapter 4: Influence of alumina crystal planes on the structure of Co nanoparticles in model Fischer-Tropsch catalysts

4.1 Introductory comments

Crystal structure of Co nanoparticles plays an important role in their efficiency in heterogeneous catalysis. One of the industrially important processes where according to many experimental observations the crystal structure of Co nanoparticles plays a crucial role is Fischer-Tropsch synthesis (FTS) – the process for obtaining linear hydrocarbons from the mixture of CO and H_2. Supported Co metal nanoparticles are widely accepted as an efficient catalyst for this process that demonstrates high activity and selectivity to long linear hydrocarbons that constitute diesel fuel; however, the influence of size and crystal structure of these particles on their catalytic activity is not yet fully understood. Moreover, these two factors are very strongly interconnected since the most stable Co structure is size dependent: *fcc* crystal packing is the most stable structure in nanoparticles smaller than 10-15 nm. At the same time, studies demonstrate that *hcp* is the more catalytically active phase in FTS. Thus, synthesis of Co nanoparticles with the desirable size and crystal structure is a difficult task that is further complicated by their interaction with the surface of the support, which can affect the crystal structure of the nanoparticles through epitaxy.

In the presented article we study the influence of surfaces of two metastable alumina phases, namely γ-Al_2O_3 and χ-Al_2O_3, on the structure of supported Co nanoparticles using the ^{59}Co Internal Field NMR technique that have proven to be very informative in determination of the crystal structures of Co in bulk.[1,2] These two metastable alumina phases possess similar specific areas and porosities; however their surfaces are dominated by different crystal planes from which they are built. Such characteristics made these two metastable alumina phases interesting for investigation due to the possible difference in their reactivity toward aqueous Co precursors. Such a dependence of the surface affinity of Co^{2+} cations was demonstrated recently both theoretically and experimentally for various alumina surfaces at the initial stage of Co deposition. Consequently, the work presented below was aimed at investigating the connection between the structure of the reduced metallic Co nanoparticles and the structure of the alumina surface.

4.2 Crystal plane dependent dispersion of cobalt metal on metastable aluminas

This part of the thesis is under review for publication in *Materials Today Nano*.

Ilya V. Yakovlev,[a, b, c] Vladimir I. Zaikovskii,[b] Mariya A. Kazakova,[b] Evgeniy S. Papulovskiy,[b] Olga B. Lapina,[a, b] and Jean-Baptiste d'Espinose de Lacaillerie[c, *]

[a] Novosibirsk State University, Pirogova Street 1, 630090 Novosibirsk, Russia

[b] Boreskov Institute of Catalysis SB RAS, Prospekt Lavrentieva 5, 630090, Novosibirsk, Russia

[c] SIMM, UMR CNRS 7615, ESPCI Paris, Université PSL, Sorbonne Université, 10 Rue Vauquelin, 75005 Paris, France

4.2.1 Abstract

Metallic Co nanoparticles, widely used and studied as supported heterogeneous catalysts for Fischer-Tropsch synthesis (FTS), display catalytic properties that can vary significantly depending on their size and crystal structure. In this work, we used ^{59}Co Internal Field NMR (^{59}Co IF NMR) complemented by high-resolution transmission electron microscopy (HRTEM) to demonstrate the influence of strong metal-support interaction on two noticeably different metastable alumina phases - γ-Al_2O_3 and χ-Al_2O_3. According to ^{59}Co IF NMR and HRTEM, the metallic particles supported on χ-Al_2O_3 were larger and displayed a significantly higher content of *hcp* Co phase, which are known to be more active and selective to C_{5+} in FTS. DFT calculations of ^{1}H NMR chemical shifts of hydroxyl groups, anchored to the (110) and (111) spinel crystal planes, revealed that the hydroxyl coverage of γ-Al_2O_3 facilitates the dispersion of Co precursor over the surface of the support. This ultimately leads to the formation of smaller metal Co nanoparticles on γ-Al_2O_3, than on χ-Al_2O_3.

4.2.2 Introduction

The catalytic properties of nanoparticles (NPs) strongly depend on their size, crystal structure and morphology – factors that have a complex interconnection with each other but that are, to some extent, controllable by adjusting the synthesis conditions. An important case study is metallic cobalt supported on oxides whose catalytic behavior depends strongly on the metal-support interaction in ways that are not yet fully understood.[3] In Fischer-Tropsch synthesis (FTS) for example, the choice of the support as well as possible decorations with various noble metal promoters are used to control the morphology and crystal structure of cobalt NPs in order to obtain the desired catalytic properties. The influence of these two properties of Co NPs on activity and selectivity towards C_{5+} hydrocarbons has been extensively studied in the recent decades resulting in some generally agreed-upon requirements. First, vast experimental data [4-9] indicate that, between the two most common structures met in metallic cobalt, the hexagonal close-packed (*hcp*) crystal structure is more active and selective towards C_{5+} than the face-centered cubic (*fcc*) one. Second, experimental data and theoretical calculations show that below a certain size (between 4 and 10 nm according to different sources) Co NPs become much less active in FTS and their selectivity shifts to CH_4 [10-15]. However, in many instances, how the desired cobalt size and structure are tailored by the support remains an open question.

During the preparation step, how the support directs the speciation of Co(II) ions and complexes from the precursor has been efficiently investigated by spectroscopic means (noticeably UV-visible spectroscopy[16] and EXAFS[17]), rationalized through coordination chemistry[18] and modeled by DFT.[19] Nevertheless, the interaction with the support of the larger Co nanoparticles obtained after reduction is paradoxically more difficult to characterize or model.[20]

Co nanoparticles can be characterized by a variety of physical methods: X-Ray diffraction (XRD), electron microscopy techniques (transmission, scanning, or scanning transmission), magnetometry, magnetic resonance techniques (electronic ferromagnetic resonance - FMR, ^{59}Co Internal Field nuclear magnetic resonance – IF NMR). All of these techniques have their own experimental limitations and provide different kinds of structural information. In this work, we rely on a combination of ^{59}Co Internal Field NMR (^{59}Co IF NMR) and high-resolution transmission electron microscopy (HRTEM), a combination that proved effective in some of our previous works.[21-24] HRTEM is an indispensable technique providing unique information on the morphology of the particles close to the single-atom scale. However, the intrinsic limitation of this technique is its local character, making it necessary to extrapolate the data obtained from a limited set of micrographs. ^{59}Co IF NMR, on the contrary, is a bulk technique that was shown to provide information on the crystal and

magnetic structures of Co nanoparticles [21,22,25-28] as well as on their size distribution,[23,29] even though it is limited by the intrinsically low intensity of the NMR signal and the difficulty of spectral analysis.

We focus here on the role of two low-temperature metastable alumina phases, γ-Al_2O_3 and χ-Al_2O_3, in directing the dispersion and structure of Co nanoparticles. γ-Al_2O_3 is a well-studied and widely employed support in Co FTS catalysts. It has a high specific surface area and demonstrates good stability under usual reaction conditions when stabilized by metal oxides. χ-Al_2O_3 is the lowest temperature form of alumina in the gibbsite alumina series; the use of this metastable phase as a catalyst support has been investigated to a much lesser extent, even though it also demonstrates a relatively high specific surface area and thermal stability. Pansanga et al. have demonstrated that the use of a mixed χ-Al_2O_3 + γ-Al_2O_3 support led to increased Co dispersion at high Co loadings, but this effect could be mostly due to the morphology of the particles and not necessarily to their surfaces structures [30]. The crystal structure as well as crystallite stacking of χ-Al_2O_3 still remain an open question with several equally feasible viewpoint (see for instance a recent mini-review by Prins [31]). Nevertheless, regardless of the preferred theory on the structure of bulk γ-Al_2O_3 and χ-Al_2O_3, an important difference between these alumina phases lies in the different crystal faces that dominate the surface of the particles. [32,33] As a result, χ-Al_2O_3 differs from γ-Al_2O_3 by the type and density of defect surface sites [34] and by having a higher surface density of weak Lewis acid sites.[35,36] These differences have been suggested to explain different metal sintering behavior.[37] Regarding specifically Co, the presence of χ-phase in γ-Al_2O_3 resulted in higher dispersion of Co as well as higher CO hydrogenation activities of the Co/Al_2O_3 catalysts compared to pure Co/γ-Al_2O_3 samples. In samples of high Co loadings, the spherical-shape-like morphology of the χ-phase Al_2O_3 provides a better stability of the Co particles.[38]

This brief summary of the literature concerning Co nanoparticles on γ-Al_2O_3 and χ-Al_2O_3 reveals the importance of the nanoparticle-support interactions[10,19] that result from an interplay between the support surface structure and its morphology. Here, we show that HRTEM and ^{59}Co IF NMR reveal significant structural differences between the Co NPs supported on γ-Al_2O_3 and χ-Al_2O_3. Finally, building on indirect DFT calculations, we link these differences to the differences in initial distribution of Co precursors on the catalyst surface.

4.2.3 Experimental

4.2.3.1 Synthesis of Co/γ-Al_2O_3 and Co/χ-Al_2O_3 supported samples

Low-temperature metastable alumina phases were used as the supports for the studied samples. γ-Al_2O_3 was obtained by calcination of pseudoboehmite (Pural SB1, Condea Chemie, Hamburg, Germany) in air at 923 K for 6 h (1.5 K/min heating rate). The same procedure was used to obtain χ-Al_2O_3 from gibbsite (Sigma-Aldrich, Merck, Darmstadt, Germany). XRD and ^{27}Al solid-state NMR techniques (see Supplementary Materials) were used to confirm the purity of the obtained powders as in our previous works [39,40]. The resulting BET (Brunauer-Emmett-Teller) specific surface areas of γ-Al_2O_3 and χ-Al_2O_3 were roughly 175 m^2/g and 150 m^2/g respectively.

In order to determine the moisture capacity of the obtained supports, they were dried at a temperature of 383 K overnight. Then, droplets of distilled water were added to 1 g of alumina under continuous stirring until the sample appeared uniformly wet. The resulting values of moisture capacity were 0.91 ml/g for γ-Al_2O_3 and 0.50 ml/g for χ-Al_2O_3.

Two series of Co/Al_2O_3 supported samples with different metallic Co content were obtained using incipient wetness impregnation with an aqueous solution of $Co(NO_3)_2 \cdot 6H_2O$ (98%, Sigma-Aldrich). The higher moisture capacity of γ-Al_2O_3 allowed introducing up to 10 wt.% of Co into the sample with a single impregnation, while χ-Al_2O_3 was able to take only up to 5 wt.% Co in a single impregnation step. Thus, to obtain comparable samples with similar impregnation protocols (meaning having the same Co content obtained by following identical impregnation protocols), 5 wt.% was chosen as the target Co content that could be obtained for both supports in a single impregnation step. The samples were impregnated with the Co nitrate solution, then dried at 383 K for 4 hours and calcined in an Ar flow at 623 K for 4 hours. Finally, the samples were reduced in a H_2 stream (50 ml/min) at 673 K for 4 hours (3 K/min ramping rate), purged with Ar for 20 min and sealed in airtight glass ampoules to avoid oxidation. The resulting samples were denoted as **5% Co/(γ-Al_2O_3 or χ-Al_2O_3).**

4.2.3.2 Characterization techniques

The morphology of the Co nanoparticles was controlled using high-resolution transmission electron microscopy (HRTEM) experiments conducted on a JEM-2010 electron microscope (Jeol, Japan) with acceleration voltage of 200 kV and 0.194 nm spatial resolution. High-angle annular dark field scanning transmission electron microscopy (HAADF-STEM) and elemental mapping images

were recorded with 200 kV acceleration voltage using a JEM-2200FS electron microscope (Jeol, Japan) equipped with a Cs corrector. Particle sizes were analyzed using FIJI software.

^{59}Co internal field NMR (^{59}Co IF NMR) spectra were recorded at 30 K on an AVANCE III 500 Fourier NMR spectrometer (Bruker, USA) using a laboratory-made solid-state probe designed for low-temperature (liquid helium cooling) IF NMR experiments. The probe was operated outside the magnet since IF NMR does not require an external static field. A solid-echo pulse sequence θ-τ-θ was used, with a θ pulse length of 1 μs and an interpulse delay τ of 8 μs. Due to the intrinsically short T_1 nuclear spin relaxation time in ferromagnetic materials, a 33 ms delay between the echo sequences was used. In order to cover the entire frequency range, the spectra were recorded stepwise with 500 kHz carrier frequency steps. A custom automatic tuning and matching device was used to retain a constant quality factor over the entire recording range. In order to determine the intensity of the spectrum at a chosen frequency, the echo signal recorded at this frequency was Fourier-transformed with adequate phase and baseline corrections such that a purely absorption spectrum was obtained. Then, the obtained signal was integrated over a roughly 400 kHz frequency range centered at the carrier frequency, after which the value of the integral was assigned as the intensity of the spectrum at said frequency. Radiofrequency irradiation power was varied at each frequency step to be able to account for the differences of enhancement factors between the bulk of the magnetic domains and the domain walls according to the method originally described by Panissod et al. [41]

^{1}H NMR spectra of the alumina supports were recorded at room temperature using a pulsed NMR spectrometer Bruker Avance 400 with a constant magnetic field of 9.4 T (400.13 MHz ^{1}H Larmor frequency). Prior to the ^{1}H NMR experiments, the samples were dehydrated for 4 hours at 450 °C and sealed inside glass ampoules to avoid rehydration from air. The samples were transferred into standard 4 mm ZrO_2 rotors under argon atmosphere right before the experiment. The spectra were recorded under magic angle spinning condition (MAS, 10 kHz rotation frequency) using a single π/2 pulse (5 μs pulse length). 1024 scans were accumulated with a 5 second delay. Tetramethylsilane was used as an external reference with a chemical shift of 0 ppm.

4.2.3.3 Theoretical calculation details

To characterize the hydroxyl coverage of the alumina surfaces, we have conducted DFT calculations of ^{1}H NMR chemical shifts of hydroxyl groups on the two most prominent crystal planes dominating the surfaces of γ-Al_2O_3 (the (110) plane) and χ-Al_2O_3 (the (111) plane) according to the cubic spinel model of the metastable alumina building blocks.

All calculations were performed using the CASTEP program.[42] The interactions between the core ions and the valence electrons were described using the projector augmented wave (PAW) pseudopotentials.[43] The geometry calculations were performed at Γ point with the exchange-correlation functional PW91.[44] A plane wave basis set cut-off energy of 450 eV with the self-consistent field threshold of 10^{-6} eV was used. The geometry calculations used the BFGS (Broyden–Fletcher–Goldfarb–Shanno) algorithm.[45]

To mimic a flat alumina surface, a layer of alumina was created from the spinel structure with the lattice parameter *a* of 8.08534 Å. A model bulk crystal cell was cleaved along the (110) and the (111) crystallographic planes. The (110) cell dimensions were 22.8688 × 16.1706 Å, while the (111) cell was 19.8048 × 11.4344 Å. The slab thickness was varied from cell to cell, from 3.5 to 8 Å, with vacuum spans of more than 10 Å to prevent periodic interaction. No additional restrictions were imposed during the structural relaxation. Extra hydroxyl groups were added to the surface Al sites in order to avoid dangling bonds and maintain electroneutrality.

The ^{1}H NMR parameters were computed by the GIPAW method [46] with cutoff energy of 600 eV and PBE (Perdew-Burke-Ernzerhof) functional.[47] The ultrasoft pseudopotentials are the ones supplied with CASTEP [48].

4.2.4 Results

4.2.4.1 High-resolution transmission electron microscopy and EDS

Figure 4.1 (**a, b**) displays typical HRTEM images of the sample 5% Co/γ-Al_2O_3 at different magnifications. According to the micrographs, the γ-Al_2O_3 support consists of large (1 μm) agglomerates of randomly oriented alumina nanocrystallites that are slightly elongated along the [100] axis. Cobalt nanoparticles (shown with white arrows in Fig. 4.1**b**) are poorly distinguished on the micrographs due to their relatively small size (5.5 nm mean diameter according to HRTEM image analysis). Several Bragg diffraction spots, corresponding to metallic Co crystallites, are clearly visible on the Fourier transform of Fig. 4.1**b** (Fig. 4.1**c**) along with the annular diffractions from the randomly oriented crystallites of γ-Al_2O_3. Interplanar distances in *fcc* and *hcp* Co are quite close, which makes the distinction between these crystal structures almost impossible here despite the presence of clearly defined diffraction spots.

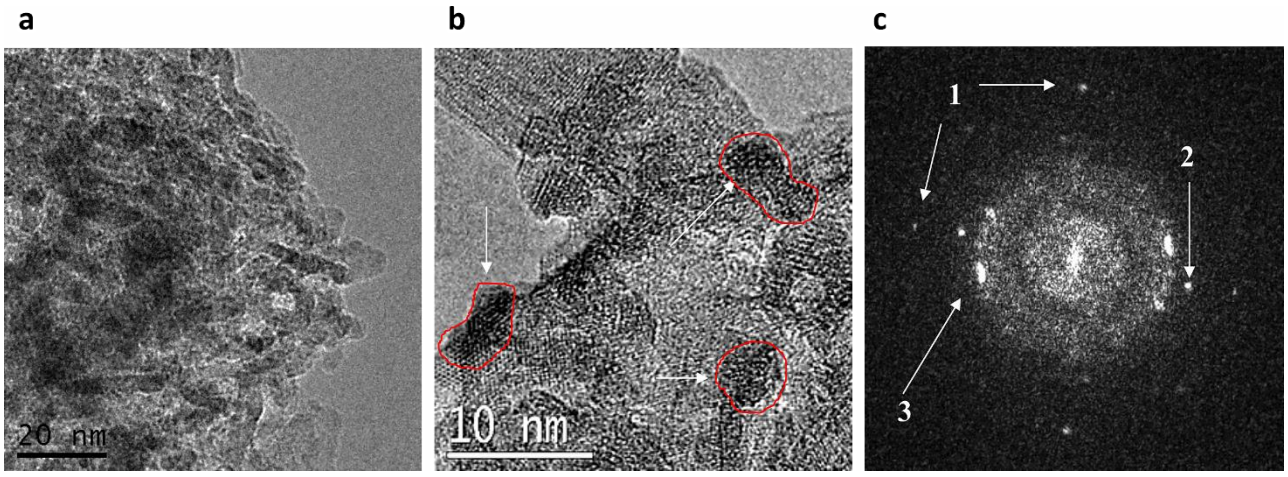

Fig. 4.1. (**a)** and (**b)**: HRTEM images of the 5% Co/γ-Al_2O_3 sample at different magnifications. Metallic Co nanoparticles are visible as dense dark areas (additionally highlighted with white arrows on **b**). (**c**): spatial Fourier transform of **b)**, Diffraction spots shown with arrows 1 and 2 correspond to cobalt nanoparticles while the annular diffractions from γ-Al_2O_3 are shown with arrow 3.

A better visualization of distribution of Co nanoparticles on the surface of the support can be obtained from the energy-dispersive mapping images recorded using HAADF-STEM technique (Fig. 4.2). In the corresponding EDS maps, areas where the Co $K_{\alpha 1}$ line (6.930 keV) emerges from the background noise are figured in red, while those where the Al $K_{\alpha 1/2}$ line (1.486 keV) emerges are in blue. Accordingly, Co appears evenly distributed on the surface of the support at the spatial resolution of the HAADF-STEM image (about 1 nm) and no Co particles can be evidenced by this method.

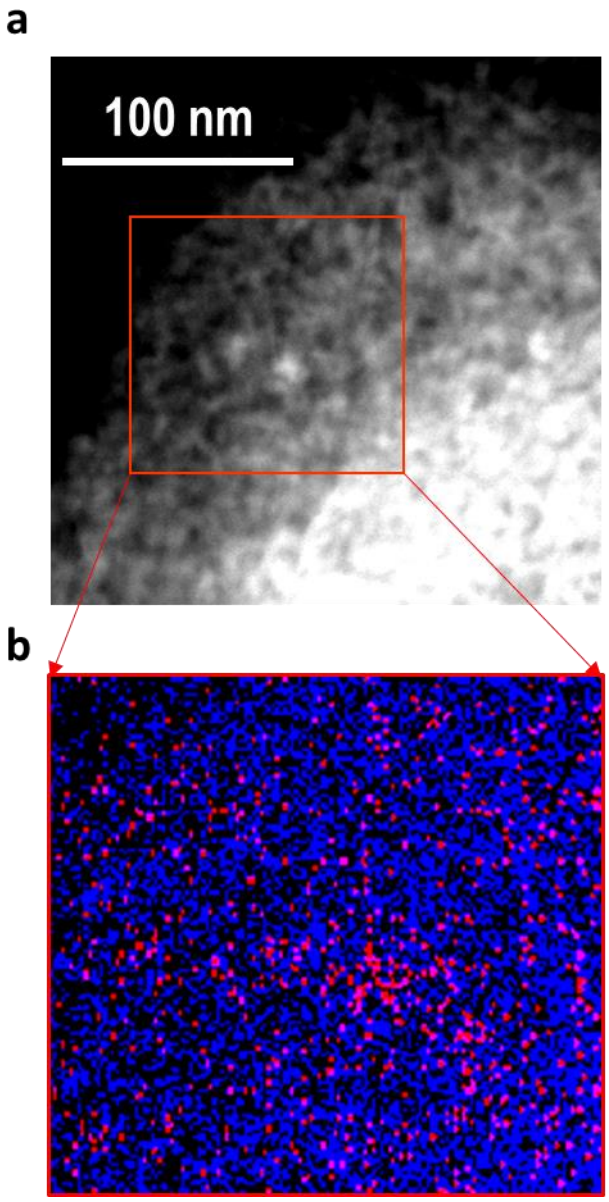

Fig. 4.2. HAADF-STEM image of the 5% Co/γ-Al_2O_3 sample (**a**) and the elemental mapping of the area in the red box obtained with EDS (**b**). Al signals are shown in blue, Co signals are shown in red.

A significantly different picture can be seen on the HRTEM micrographs of the 5% Co/χ-Al_2O_3 sample (Fig. 4.3). In this case, the χ-Al_2O_3 support consists in large 0.5 μm platelets (a clear example can be seen in the HRTEM image at low magnification, Fig.S1 in Supplementary Materials). The platelets are built from nanocrystalline domains (about 10x10 nm^2) oriented in the same direction and separated by 3-5 nm-sized pores. On this support, dark areas reveal Co nanocrystallites with sizes of about 5-10 nm. Moreover, EDS images (Fig. 4.4b) demonstrate that Co is not evenly distributed on the surface of the support. Higher Co densities areas sized up to 100 nm are visible and coincide with

the brighter areas in the HAADF-STEM images of Figure 4.4a. Combining these observations leads to the conclusion that Co forms assemblies of ~100 nm consisting of ~10 Co nanocrystallites with sizes of about 5-10 nm. In addition, the spatial Fourier transform image of the micrograph containing the cobalt nanoparticles (Fig. 4.3**d**) clearly demonstrates a near-overlap of the diffraction spots corresponding to the interplanar distances of the support and of the metallic Co. In this FFT image the diffraction spot of Co metal (d = 0.191 nm, $P6_3/mmc$ space group, PDF №050727) is very close to the brighter diffraction spot that corresponds to χ-Al_2O_3 (d = 0.212 nm). Together with a moiré pattern visible in the supported Co nanoparticles (Fig. 4.3**c**), this signs an orientation coincidence of the Co nanocrystallite with the alumina crystal domains forming the support surface. This means that both the orientation of growth and the interplanar distance value coincide suggesting an epitaxial relation between the Co particles and the χ-Al_2O_3 surface.

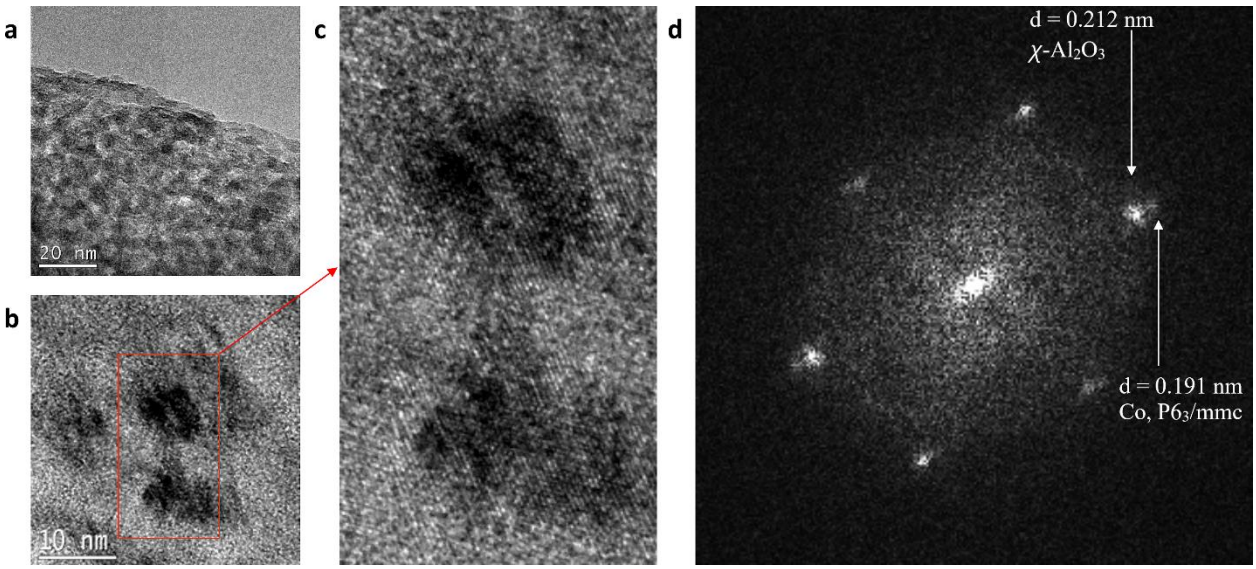

Fig. 4.3. (**a)** and (**b)**: HRTEM images of the 5% Co/χ-Al_2O_3 sample at different magnifications. Metallic Co nanoparticles are visible as dense dark areas. **(c):** Magnification of the area inside the red box of b). **(d):** Spatial Fourier transform of **b**). The diffraction spots corresponding to the Co metal and χ-Al_2O_3 are denoted with white arrows. Such a close arrangement of diffraction spots in distance and angle suggests epitaxy between the Co nanoparticle and the surface of the support.

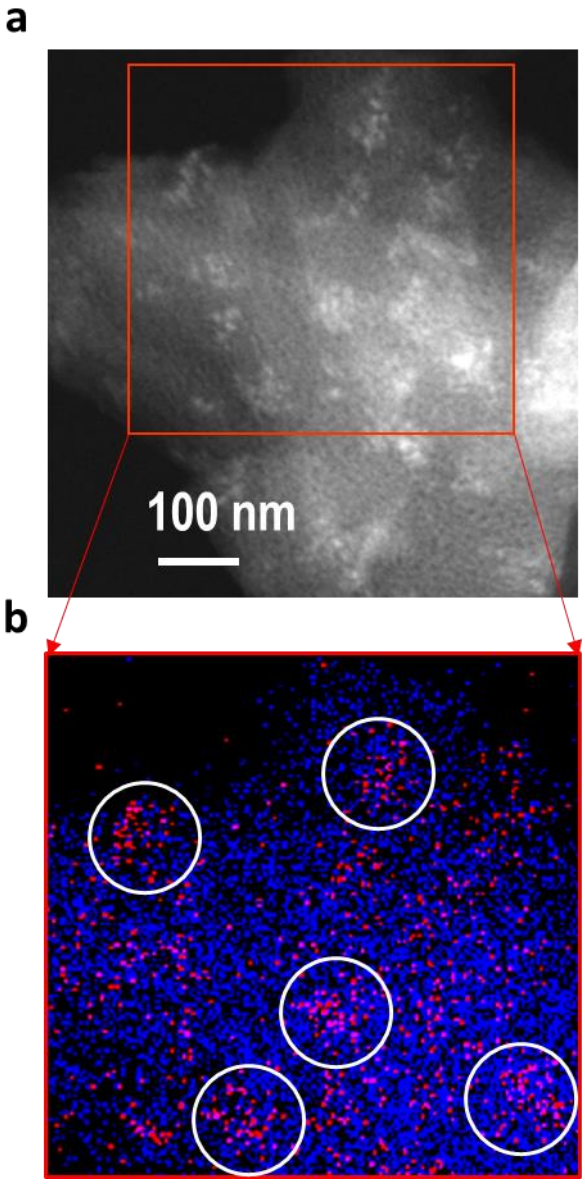

Fig. 4.4. HAADF-STEM image of the 5% Co/χ-Al_2O_3 sample (**a**) and the elemental mapping of the area in the red box obtained with EDS (**b**), Al signals are shown in blue, Co signals are shown in red. White circles in (b) are used to locate the large Co NP assemblies identified as brighter areas in (a). Individual points on the EDS elemental maps do not indicate the presence of Co with certainty, because their appearance may be connected with the background noise in the EDX spectra. However, since noise is expected to be randomly distributed on the elemental maps, the areas that contain larger densities of points (shown with the white circles in Fig. 4.4**b**) can be associated with Co particles and do indeed coincide with the brighter areas of the HAADF-STEM image (Fig. 4.4a).

Thus, HRTEM and HAADF-STEM techniques demonstrate that, at 5% Co loading, the χ-Al_2O_3 surface appeared much more ordered than the one of γ-Al_2O_3 and that the Co nanoparticles were oriented in epitaxial relation with the χ-Al_2O_3 surface. At the same time, elemental mapping images show that cobalt was more homogeneously dispersed over the surface of γ-Al_2O_3 in the form of small (5 nm and less) nanocrystallites, while larger Co nanocrystallites (5-10 nm) tended to associate on the surface of χ-Al_2O_3.

Electron microscopy techniques revealed the morphology and structure of the samples, but due to their strictly local character, these methods are not optimal for studying the crystal structure of Co nanoparticles in the entire volume of the sample. In contrast, ^{59}Co internal field NMR (^{59}Co IF NMR) is a technique able to discern between different types of crystal structure of metallic Co in the bulk – something that is more likely to relate to the overall efficiency of the catalyst.

4.2.4.2 ^{59}Co internal field nuclear magnetic resonance

^{59}Co IF NMR spectra reflect both the crystal and the magnetic structures of Co nanoparticles, which affect the hyperfine magnetic field at the location of the nucleus. It can be observed only in ferromagnetic particles. In superparamagnetic ones, the internal field fluctuates rapidly at the timescale of the NMR experiments and no signal is generated. Consequently, we have demonstrated earlier that the size of Co nanoparticles is an equally important factor affecting the ^{59}Co IF NMR spectra, when particles below the nominal critical superparamagnetic size are present in the sample. The critical size below which particles isolated from each other are superparamagnetic (and thus are undetectable in IF NMR) at room temperature was shown to be equal to roughly 7.5 nm in diameter for isolated particles.[23] However, in non-isolated particles, magnetic ordering of the particles due to interparticle magnetic interactions (dipolar and exchange) affects the critical size for superparamagnetic/ferromagnetic transition in a way that is difficult to predict quantitatively. In practice, we can consider the particles to be isolated when the energy of dipolar interaction between the particles is much smaller compared to magnetic anisotropy energy [49], which is the case for cobalt particles about 5 nm in diameter and separated by at least the same distance. From these considerations, according to the electron microscopy data, a significant fraction of Co nanoparticles in the 5% Co/γ-Al_2O_3 and 5% Co/χ-Al_2O_3 samples could be superparamagnetic and undetectable by ^{59}Co IF NMR at room temperature. Therefore, we conducted the ^{59}Co IF NMR experiments at 30 K where the critical particle size for superparamagnetic transition decreases to 3.5 nm. It can then be safely assumed that almost all Co particles in the studied samples are in a ferromagnetic state and contribute to the ^{59}Co IF NMR spectra.

As stated in the experimental section and according to a now well-established procedure,[23] the spectra were recorded at different radiofrequency powers in order to discern between the multi domain and single domain ferromagnetic particles. The distribution of optimal radiofrequency power (power at which the spectral intensity at the chosen frequency is maximum) for all spectra was practically uniform meaning that we have not detected any multi domain Co particles. This is in complete agreement with the observations made using HRTEM since multiple magnetic domains are not expected to occur in particles smaller than 70 nm.[50] Therefore, all of the obtained spectra were analyzed from the standpoint of single domain particles.

^{59}Co IF NMR spectra of the studied samples recorded at 30 K are shown in Fig. 4.5. The spectrum of the sample supported on γ-Al_2O_3 (bottom) displays a dominant line centered at 222 MHz that corresponds to single domain particles with *fcc* structure [28]. The relatively weak wide shoulder stretched from 224 MHz to 235 MHz indicates the minor occurrence of particles with *hcp* structure[28]. The *hcp* crystal structure is the stable form of bulk Co at, and below, room temperature (the *hcp*– *fcc* transition is known to happen at roughly 700 K). However, according to many experimental observations, the decrease of the size of Co nanoparticles leads to the stabilization of the *fcc* crystal phase to the extent that, for relatively small nanoparticles, this phase becomes dominant, as observed here.[51,52] Thus, the obtained spectrum further corroborates the electron microscopy observations that Co was present as highly dispersed small nanoparticles over the surface of the support in the case of γ-Al_2O_3. Tsakoumis et al. have shown using HRTEM that even at a 20 wt.% Co loading, Co nanoparticles supported on the surface of γ-Al_2O_3 have an average size of 5.2 nm with no particles larger than 14 nm in diameter.[10] This is consistent with the observed prevalence of the *fcc* Co signal in the ^{59}Co IF NMR spectrum of the sample supported on γ-Al_2O_3 that is reported here.

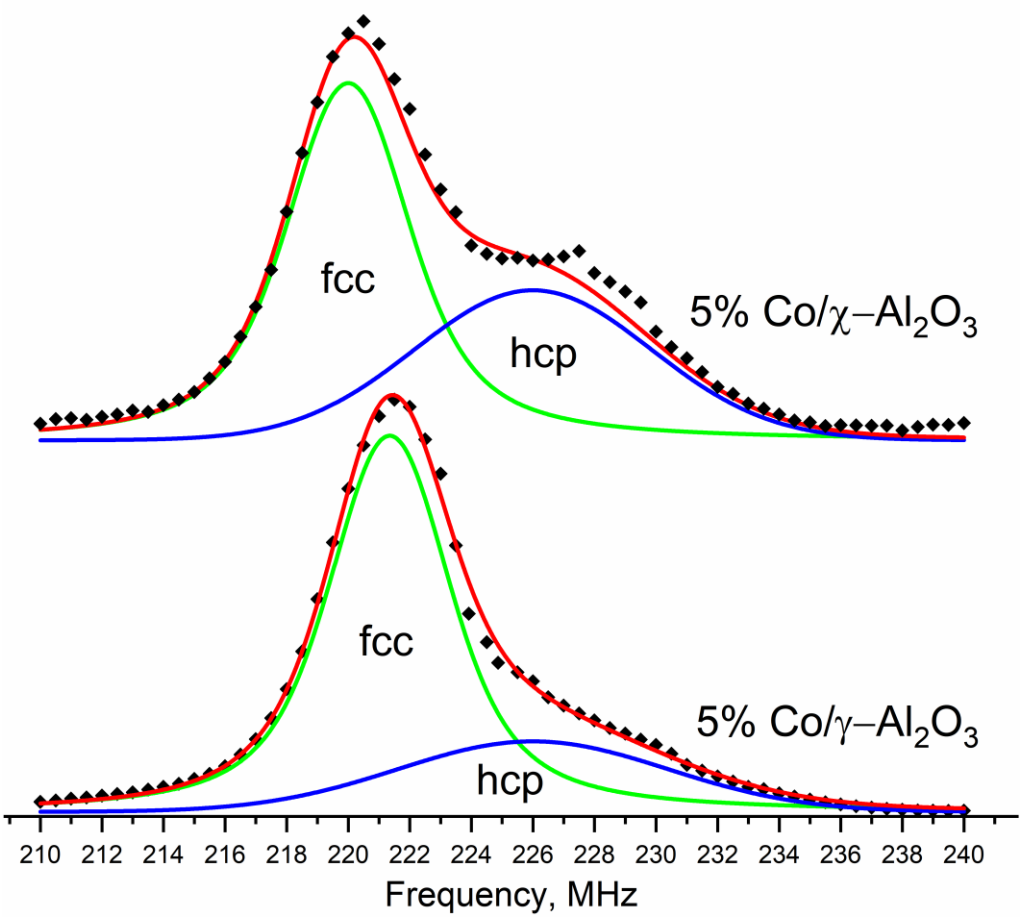

Fig. 4.5. ^{59}Co IF NMR spectra of the 5% Co/γ-Al_2O_3 (bottom) and 5% Co/χ-Al_2O_3 (top) samples. T = 30 K. Spectra are normalized to the same maximal intensity. Echo measurement points are shown with symbols, while the lines show the result spectral decomposition into two Pseudo-Voigt profiles for *fcc* Co (green) and *hcp* Co (blue). The sum of these two profiles is shown in red.

In the spectrum of the 5% Co/χ-Al_2O_3 sample (Fig 4.5, top), one can observe a similar line shape consisting of two broad signals corresponding to single domain *fcc* and *hcp* phases of Co, with the *fcc* line undergoing a 1 MHz frequency shift compared to the 5% Co/γ-Al_2O_3 sample. The quantitative analysis of the *fcc* and *hcp* fractions in the samples can be made by decomposition of the experimental spectra into two broad peaks. The signal from the *fcc* and *hcp* packed Co can be represented as two Pseudo-Voigt profiles centered around 220 MHz and 227 MHz respectively, with the line for *hcp* Co being much broader than the line of *fcc* Co due to stronger magnetic anisotropy in the former case [53]. The end results of such decomposition (shown as colored lines in Fig. 4.5), namely the relative intensities of the *fcc* and *hcp* signals, reflect the relative contents of these crystal phases in the samples, which were 24% of *hcp* Co for γ-Al_2O_3 and 39% *hcp* Co for χ-Al_2O_3. Those

values constitute a lower estimate. Indeed, very small fcc Co particles being superparametic might not contribute to the IF NMR spectra.

4.2.4.3 Experimental and predicted ^{1}H chemical shifts

The initial stage in the formation of Co nanoparticles on the surface of the support is the anchoring of Co(II), from the precursor ions, on the available vacant sites. Using EXAFS and *ab initio* calculations of the adsorption energy of Co on different surfaces of α-Al_2O_3, Chizallet et al. [54] have recently demonstrated that the hydroxyl coverage of the surface and the location of the surface vacancies greatly influence the interaction energy of Co(II) with the alumina surface.

Determining *ab initio* the hydroxyls on the alumina surface susceptible to interaction with different amounts of Co(II) is obviously very informative but requires lengthy computations involving large sets of models with different types of alumina surfaces together with the necessary water to coordinate and stabilize the dangling groups. We tried instead a semi empirical approach based on correlating of the experimentally observed and theoretically predicted ^{1}H NMR shifts.

To that aim, the first step is to choose a reliable structural model of of γ-Al_2O_3 and χ-Al_2O_3 surfaces. While modelling the surface of the stable trigonal α-alumina is relatively straightforward due to its completely refined crystal structure, the structures of metastable alumina remain disputed. In particular, the low temperature γ-Al_2O_3 metastable phase has attracted the highest attention due to its relevance as a heterogeneous catalyst and catalyst support. γ-Al_2O_3 is been generally considered to have a cubic spinel structure [31,55], even though the stoichiometry of Al_2O_3 does not directly correspond to a spinel AB_2O_4. Such structural disparity led to different models describing the distribution of Al ions and vacancies in the spinel cationic sublattice [31]. Despite the differences of these models, the majority of researchers agree that the bulk structure of γ-Al_2O_3 particles belongs to the cubic spinel type. On the other hand, the surfaces structure and bonding scheme of these particles remain debated and a brief discussion of existing models is necessary before proceeding further.

The most widely used models of metastable alumina surfaces were proposed by Knözinger and Ratnasamy [56]. It consists of bulk spinel structure cleavages along (100), (110) and (111) crystal planes. The reactivity of such surfaces in hydrated conditions then mainly depends on the hydroxyl coverage obtained by addition of protons and hydroxyls to compensate for the charge and coordination symmetry of surface Al and O sites [57,58]. Further improvements upon this model include reconsiderations of the bulk alumina structure to non-spinel models [59], as well as accounting for the finite size effect [60,61] and for stacking faults of individual alumina crystallites [32].

The first implication of the finite size of an alumina crystallite is the presence of edges between its surfaces that lead to the occurrence of unique hydroxyl sites that are not hydrogen-bonded to other hydroxyl groups and remain highly reactive to chlorination as was shown by ^{1}H NMR and *ab initio* calculations by Batista et al. [58]. The second important effect of the finite particle size is also connected to the synthetic routes used to obtain the metastable aluminas. Most frequently, aluminum oxides are obtained through dehydration of corresponding hydrates as was experimentally demonstrated by Stumpf et al [62]. In this case, the restructuring of individual particles is governed by topotactic transformations during which the structural features of the initial particles are conserved. Due to the layered nature of the alumina hydrates, the topotactic transitions result in differences of alumina surfaces that formally belong to one crystal plane family (e. g. (110) cubic spinel plane) depending on basal/lateral position in the initial particle as was demonstrated using DFT calculations in the recent paper by Pigeon et al. [61].

At the same time, metastable aluminas are intrinsically nanostructured materials, thus the description of their structures requires to account for the defectiveness and stacking of the individual crystallites that also play an important role on formation of the particle surfaces. The approach developed by Tsybulya et al. accounts for the connectivity of individual spinel crystallites through planar defects lying in the (100), (110) and (111) crystal planes of cubic spinel [32]. This technique allowed modeling the structures of low-temperature aluminas as well as demonstrating the effect of abundant shearing planar defects that allow the existence of a cubic spinel material with a non-spinel stoichiometry. Later, this approach was also used by Pakharukova et al. to create 3D nanostructured models of γ-Al_2O_3 particles and simulate the XRD patterns, which coincided with the experimental XRD patterns and allowed to explain the diffuse nature of several peaks [63].

Both the topotactic transition and crystallite stacking approaches do not contradict each other, but provide a complementary description of both the bulk and the surface of metastable alumina nanoparticles. Importantly, both of these approaches coincide in their prediction of the crystal planes that form the surface of γ-Al_2O_3 nanoparticles, namely (100) and (110) crystal planes with the minor presence of the (111) plane.

The much less investigated structure of the metastable χ-Al_2O_3 obtained through dehydration of aluminum trihydroxide gibbsite remains an open question without any commonly accepted viewpoint. The source of this controversy lies in the presence of the diffuse scattering peak at $2\theta = 43°$ in its XRD pattern that does not belong to the cubic spinel structure, even though the rest of the XRD pattern corresponds to the said structure. Additionally, the ^{27}Al NMR spectra reveal an $Al^{[6]}$:$Al^{[4]}$ equal

to roughly 3:1, that also does not correspond to the spinel structure, for which this ratio is expected to be 2:1 (as observed in ^{27}Al NMR spectra of γ-Al_2O_3) [64]. However, recently, Yatsenko et al. [65] have shown using the "crystallite stacking" approach that the non-spinel diffuse scattering peak of χ-Al_2O_3 may appear due to planar defects of the anion sublattice of cubic spinel structure (the O^{2-} sublattice in ratioAB_2O_4 spinel follows a regular *fcc* pattern, while such planar defects change its local ordering to *hcp*). This observation allows one to consider the particles of χ-Al_2O_3 as having the cubic spinel structure when trying to model its surface in the same way as it was done for γ-Al_2O_3. With this consideration, the surface of χ-Al_2O_3 is mostly represented by the (111) spinel crystal plane as was shown in [32]. Moreover, if we apply the same logic of topotactic transitions to the well-refined structure of gibbsite just as it was done for boehmite in the case of γ-Al_2O_3, the result for the most exposed crystal plane will be the same. Indeed, the hexagonally symmetric particles of gibbsite have a layered structure with the layers of aluminum octahedral separated by hydrogen-bonded hydroxyl layers in the direction perpendicular to [001] axis. Thus, the (001) crystal plane that has a hexagonal symmetry is the most prevalent for the gibbsite particles [66,67]. According to Mitsui et al. [68], gibbsite particles retain their morphology during the dehydration into χ-Al_2O_3 including the hexagonal symmetry of the (001) basal planes. Therefore, the retention of the particle morphology and the surface prevalence of the hexagonally symmetric planes (001) in the case of gibbsite and (111) in the case of χ-Al_2O_3 allow us to assume that the (001) basal planes of gibbsite undergo a transition into the (111) planes of the dehydrated alumina.

In summary, the surface of metastable aluminas can be accurately described in terms of spinel crystal planes, mainly (100) and (110) with the minor presence of the (111) for γ-Al_2O_3 nanoparticles, and (111) for χ-Al_2O_3.

Accordingly, the γ- and χ-Al_2O_3 surfaces (Fig. 4.6) were modeled by cleaving the crystal structure along the directions of the (110) of (111) crystal planes. We also note that such a representation of the particle surface as infinite slab cannot possibly account for the edges formed between the crystallite surfaces or for the subtle features of the crystal planes formed during the topotactic transition. Nevertheless, such approach can still be feasible and useful for the prediction of the general behavior of the alumina surface towards the hydrated Co ions in the precursor solution. By using the similar infinite slab model, Larmier et al. [19] have demonstrated the so-called structural recognition of Co^{2+} ions on the (100) and (110) surfaces of a cubic spinel model of γ-Al_2O_3. They have shown that the most energetically favorable mode of adsorption of Co^{2+} ions is the one during which octahedral complexes including one or two bonds between Co^{2+} and lattice oxygen are formed.

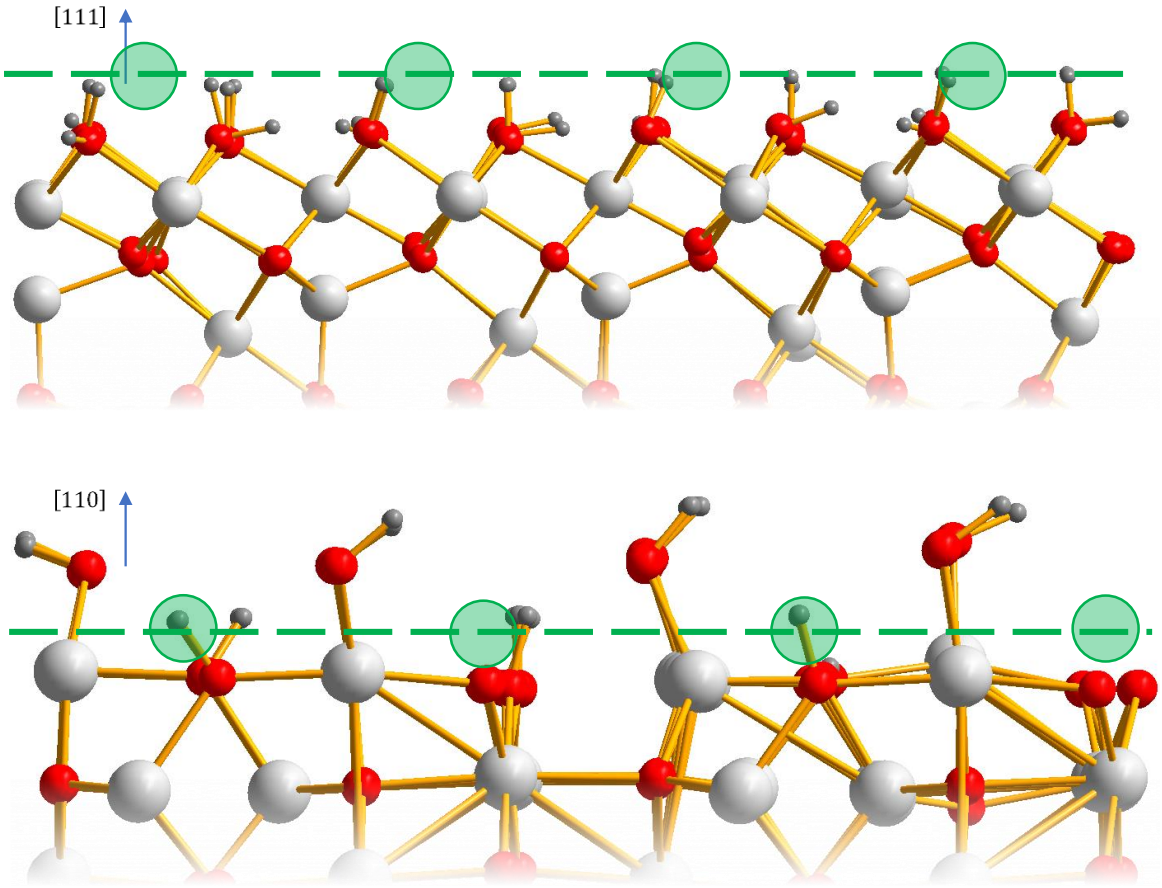

Fig. 4.6. Models of the (111) (top) and (110) (bottom) crystal planes of the spinel structure of crystallites forming metastable alumina phases. Al atoms are shown in silver, O atoms are shown in red, H atoms are shown in black. Green circles and lines denote the positions of the Al atoms that are missing from the next layer. Such sites can form vacancies available to Co^{2+} ions.

The hydroxyl groups were added to the spinel slabs to compensate for the charge and any dangling bonds that were formed during the cleavage (more details can be found in the Experimental section). After the relaxation of the structures without any additional constraints, we calculated the ^{1}H chemical shifts of all the hydroxyl groups now present on these model surfaces. The resulting sets of calculated chemical shifts ascribed to the (110) and (111) surfaces, as well as their comparison with the experimental ^{1}H NMR spectra, can be found in Fig. 4.7 (calculated spectra are shown with colored lines, while the experimental data are shown in black). Both the calculated sets of chemical shifts and the experimental ^{1}H 10 kHz MAS NMR spectra displayed a significant difference in the spectral intensity in the 5-10 ppm region. Namely, the intensity in this region was zero for the (111) plane model, which agreed well with the low relative intensity observed in the same region of the experimental spectrum of χ-Al_2O_3. Furthermore, edges between the spinel surfaces are present in both

samples, resulting in additional terminal hydroxyl groups that give rise to a distinct line at 0 ppm in the experimental spectra (blue line in Fig. 4.7**a, b**) as was predicted by Batista et al. [60]. These hydroxyl groups were obviously missing from the perfect plane models and thus, had to be added to the decomposition of the experimental spectra manually. The experimental spectra were decomposed into the theoretical spectra for (111) and (110) planes as well as the line corresponding to surface edges until the best match was achieved. The resulting relative intensities of the theoretical spectra of crystal planes excluding the surface edges were: 50% (111) plane and 50% (110) plane for χ-Al_2O_3; 30% (111) plane and 70% (110) plane for γ-Al_2O_3. Thus, the ^{1}H NMR data demonstrate that the surface of γ-Al_2O_3 is mostly represented by the (110) crystal plane, while an equal mixture of (111) and (110) spinel crystal planes makes up the surface of χ-Al_2O_3. The difference between the compositions of these surfaces can play an important role during their interaction with the Co impregnation solution since hydroxyl coverages of the spinel crystal planes differ significantly: the hydration of the (111) spinel plane gives rise exclusively to bridging (μ_2- and μ_3-OH) groups, while the (110) spinel plane contains a mixture of terminal (μ_1-OH) and bridging (μ_2-OH) groups.

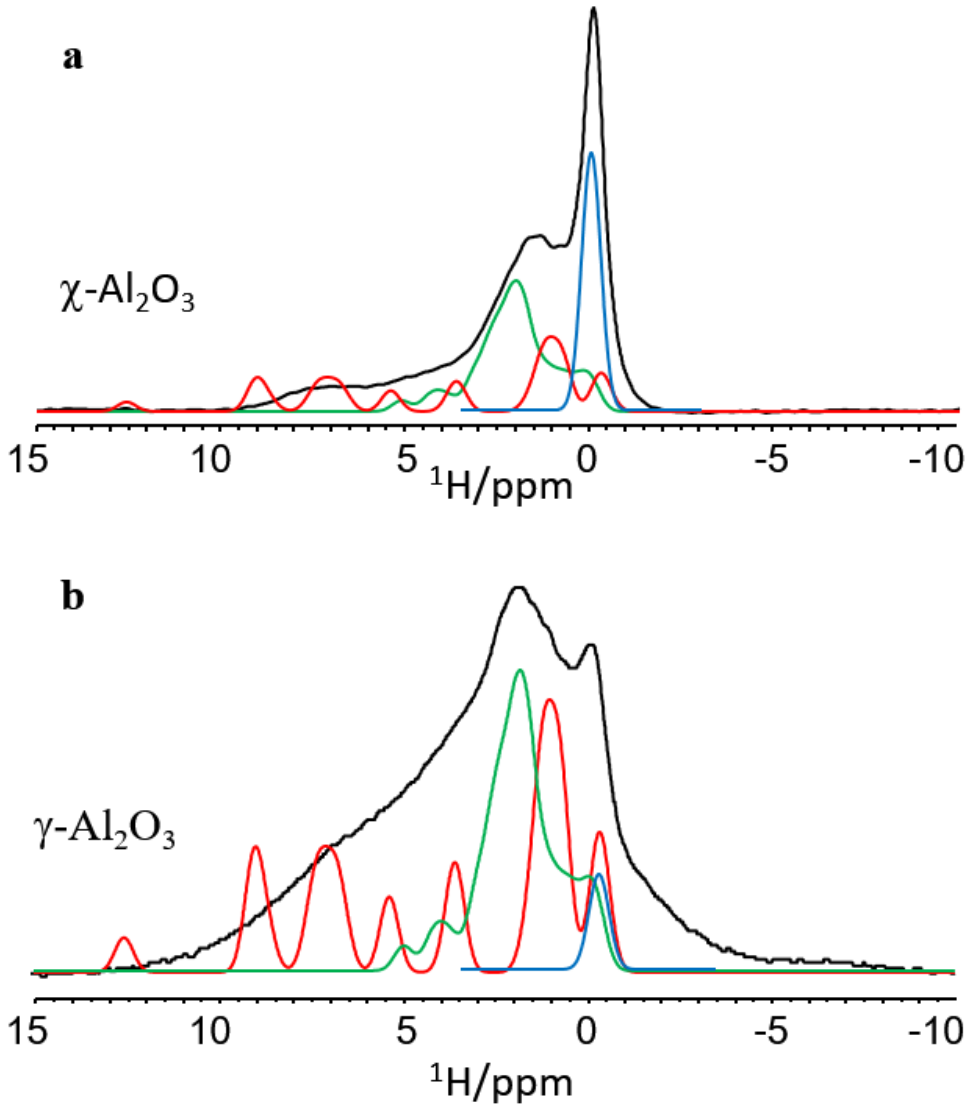

Fig. 4.7. Decomposition of the experimental 10 kHz MAS ^{1}H NMR spectra of dehydrated χ-Al_2O_3 (**a**, black line) and γ-Al_2O_3 (**b**, black line) into the theoretically calculated spectra for (110) and (111) spinel planes (red and green lines, correspondingly) and the separate line corresponding to hydroxyl groups supported on the edges between the crystallite surfaces according to ref. [60] (blue line). The relative contributions of the (111) and (110) planes to the spectra excluding the signal at 0 ppm, were: 50% (111) plane and 50% (110) plane in the case of χ-Al_2O_3; 30% (111) plane and 70% (110) plane in the case of γ-Al_2O_3. Note, that the given values reflect the surface densities of the OH groups and correspond directly to the surface areas represented by these planes in the samples.

4.2.5 Discussion

Larmier et al. have shown, using DFT calculations, that epitaxial interaction of aqueous cobalt precursor with the surface of γ-Al_2O_3 (modelled as (100) and (110) infinite cleaved slabs) is energetically favorable during the impregnation and drying stages of FTS catalyst synthesis.[19] This interaction was linked to the formation of the mixed cobalt-aluminum oxide layer at the interface between the support surface and Co nanoparticle through structural recognition. Simply put, Co^{2+} ions from the impregnation solution tend to occupy the vacancies created by removal of the octahedral Al^{3+} sites, which leads to creation of stable octahedral Co^{2+} complexes and dispersion of Co over the surface of the support. This, in turn, may lead to the deactivation of small (less than 5.3 nm in diameter) Co nanoparticles during the onset of FTS or a complete inactivity of the sample in the extreme case of very small (less than 3 wt.%) Co loading [10].

The epitaxial relation between the reduced Co nanoparticles and the surface of χ-Al_2O_3 that we observed by HRTEM in the reduced sample was necessarily a direct consequence of a strong particle-support interaction at some stage of the synthesis. However, the effects of this interaction were strikingly different in the cases of γ- and χ-Al_2O_3. The key differences between these supports lie firstly in the crystal planes dominating their surface and secondly in the morphology of the particles.

As apparent from our semi empirical modelling of alumina surfaces, γ- and χ-Al_2O_3 differ by the nature of crystal planes at their surface thus leading to completely different types of hydroxyl coverage. The hydroxyl coverage of (111) plane (and correspondingly χ-Al_2O_3, Fig. 4.6 top) consists exclusively of bridging hydroxyl groups located under the potential vacancies (missing Al^{3+} sites, shown with green circles in Fig. 4.6, top), thus preventing them from stabilizing any adsorbed ion. For the (110) plane (dominating the surface of γ-Al_2O_3, Fig. 4.6 bottom) we observe a picture strongly resembling the C-μ_1-μ_2 model presented by Chizallet et al. [54], with the main similarity being the mixed terminal-bridging hydroxyl coverage. This, in turn, is connected with the presence a plane below the level of terminal hydroxyl where vacancies for octahedral complexes can form and provide direct anchoring to the lattice O^{2-} (Fig. 4.6, bottom). According to DFT calculations made by Chizallet et al., these vacancies provide a large gain in the absorption energy during the onset of $Co(OH)_2$ formation. Such increased strength of interaction between the metallic Co precursor and the surface of the support would inevitably lead to strong dispersion of Co^{2+} ions over the surface of γ-All_2O_3 that would in turn result in a large amount of hard-to-reduce Co species and a decrease of the metallic Co particle size. A prominent signal at 0 ppm in the ^1H NMR spectrum of χ-Al_2O_3 is also worth noting because

according to work by Batista [60] this chemical shift range corresponds to the hydroxyl groups supported on the edge between the crystallite surfaces of the particle. Thus, even though the relative content of these hydroxyl groups is high, they do not facilitate the anchoring of the Co^{2+} ions due to their location. Indeed, the edges contain undercoordinated sites and cannot provide a suitable vacancy for an octahedral Co^{2+} complex.

Thus, the modeling of the hydroxyl coverage helps rationalize the observations made using HRTEM and ^{59}Co IF NMR; namely, the smaller particle size and the prevalence of *fcc* metallic Co in the sample supported on γ-Al_2O_3 after calcination and reduction, when compared to the sample supported on χ-Al_2O_3. The same rationalization may also be made for the difference in moisture capacities that we observed during the sample preparation while the specific surface areas of the powders were very close. The role of surface hydroxyl coverage during surface wetting has been studied for many oxide materials including Al_2O_3 [69,70]. Dangling hydroxyl groups available for the formation of H-bonds with the water molecules were shown to facilitate the formation of a liquid water layer on the surface of all of the studied oxides. Thus, the higher moisture capacity of γ-Al_2O_3 can also be ascribed to the presence of terminal hydroxyl groups on (110) plane representing the majority of its surface.

Furthermore, the remarkable coincidence of the structural parameters of the metallic Co particles and the surface of χ-Al_2O_3 cannot be ignored here. The hexagonally symmetric pattern of its surface (Fig. 4.8) may be directly rationalized through topotactic transformations of gibbsite particles as was mentioned above. This direct observation of the prominent (111) crystal plane in HRTEM images of χ-Al_2O_3 serves as a further proof for the spinel-based models of its crystal structure and may shed light on what can be called structural recognition in this case. In the view of the (111) surface model presented in the preceding section, it can be inferred that the missing Al atoms (possible vacant sites for Co^{2+} anchoring) also follow a hexagonal pattern. Moreover, the morphology of χ-Al_2O_3 particles that includes relatively large and oriented crystallites would favor the formation of larger and well-ordered metal particles. However, the distance between any two closest "vacancies" (approximately 4.5 Å) is much larger than the Co-Co distance in the metallic cobalt (approximately 2.5 Å). Consequently, we cannot say that this simple vacancy model determines the way in which the Co nanoparticles are formed after reduction. Nevertheless, it is reasonable to assume that the hexagonal symmetry of the surface of χ-Al_2O_3 promotes the *hcp* phase formation who appeared favored from the experimental NMR observations.

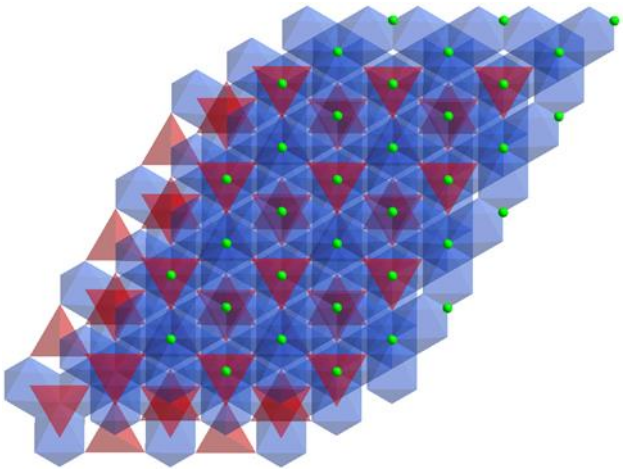

Fig. 4.8. View on the (111) plane from the above. Tetrahedral Al sites are depicted with red, octahedral Al sites are depicted with blue. Green dots represent the possible vacancies.

4.2.6 Conclusions

Rational design of supported cobalt catalysts requires an efficient way to predict the catalytic properties of Co nanoparticles based on their structural and morphological properties. Such predictions are made possible by the extensive studies on the influence of Co NP sizes and crystalline structures on their activity and selectivity. In this work, the application of a non-local technique such as ^{59}Co Internal Field NMR spectroscopy in combination with local electron microscopic techniques proved to be very efficient. It provided an efficient way to investigate the structure and size (partially through the dependence on the stability of different crystal structures on the size of the nanoparticles) of the cobalt nanoparticles on the surface of the sample.

In particular, we have demonstrated that χ-Al_2O_3 makes more favorable the *hcp* structure for supported Co metal nanoparticles, which is related to the presence of larger particles when compared to the ones supported on γ-Al_2O_3, as revealed by 30 K ^{59}Co NMR experiments. Correspondingly, the elemental mapping performed during the STEM experiments revealed the presence of 5-10 nm metallic Co particles assembled into patches on the surface of χ-Al_2O_3 in contrast to highly dispersed Co on the surface of γ-Al_2O_3. Such a difference between these metastable alumina phases could be attributed to the alumina particle morphologies observed in HRTEM micrographs. γ-Al_2O_3 formed aggregates of small randomly oriented nanocrystallites, while the χ-Al_2O_3 sample consisted of larger micron-sized plates oriented in the same crystalline direction that gave rise to a hexagonal pattern of diffraction spots in the Fourier transform analysis. Such particle morphologies, together with the

slightly smaller specific surface area of χ-Al_2O_3, would naturally lead to larger Co particles reduced on this support. Additionally, in agreement with the works by Chizallet et al.[54] and Larmier et al. [19], the hydroxyl coverage of Al_2O_3 plays an important role in the formation of Co particles by creating vacant sites that can accommodate an octahedral Co^{2+} complex anchored directly to the O^{2-} sublattice.

According to the approach developed by Tsybulya, different metastable aluminas consist of similar spinel blocks but stacked in different ways, the crystal planes most prominent on the surface of their particles also differ. This allowed us to create simple models of χ-Al_2O_3 and γ-Al_2O_3 surfaces, and in particular of their hydroxyl coverages. As we confirmed using ^{1}H MAS solid-state NMR and *ab initio* DFT calculations of ^{1}H chemical shifts, the (111) crystal plane representing the surface of χ-Al_2O_3 contained exclusively bridging hydroxyl groups, while the (110) crystal plane prominent in γ-Al_2O_3 contained a mixture of bridging and terminal hydroxyls. According to the literature, the presence of both types of hydroxyl groups facilitates both the wetting of the surface and the dispersion of Co cations over the surface of the support. This, in turn, would facilitate the dispersion of metallic Co apparent in 5% Co/γ-Al_2O_3 sample.

This is in complete agreement with our experimental observations by HRTEM and IF NMR of larger hcp Co particles on χ-Al_2O_3. The structure and particle morphology of χ-Al_2O_3 led to the formation of larger Co nanoparticles with higher *hcp* Co content as compared to γ-Al_2O_3. The hcp Co structure is further stabilized by the hexagonal symmetry of the (111) spinel crystal plane. Thus, the type of the surface of the alumina support can influence the size and crystal structure of the supported Co nanoparticles, which provides further possibility for fabrication of Co nanoparticles with the desired catalytic properties.

4.3 Supplementary materials

Figure S1 demonstrates a clear HRTEM image of a typical particle comprising the 5% Co/χ-Al_2O_3 sample. Metallic Co nanoparticles are visible as darker spots supported on a roughly 0.5x0.5 μm^2 platelet of χ-Al_2O_3.

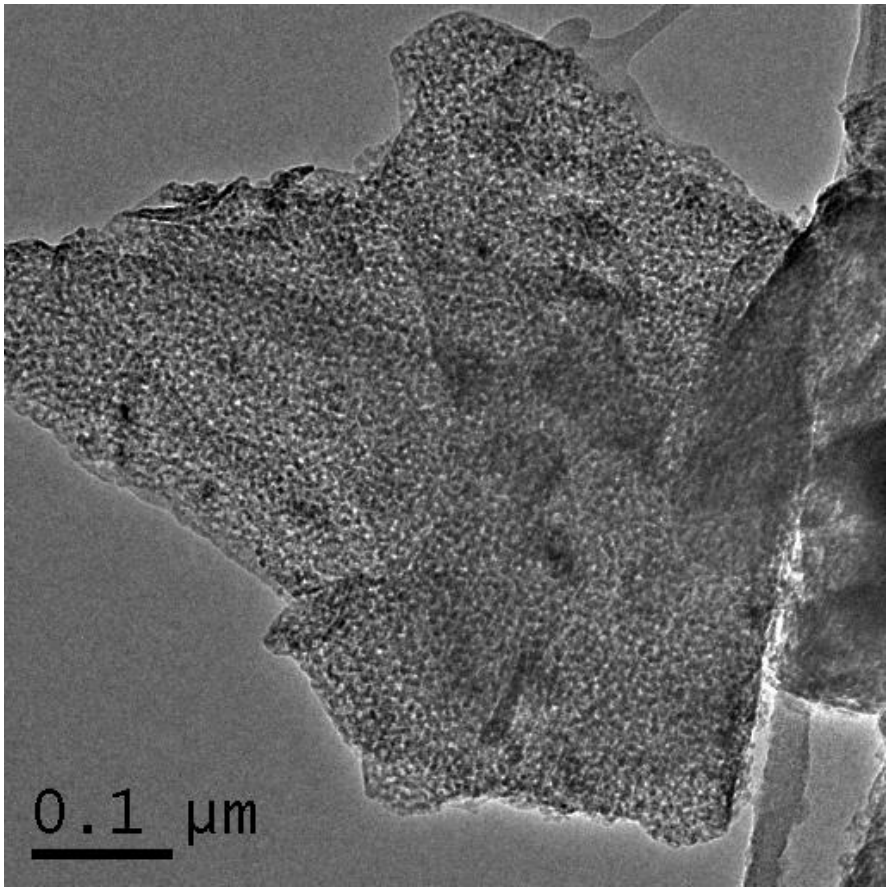

Figure S1. HRTEM image of a particle typical for 5% Co/χ-Al_2O_3 sample.

Figure S2 shows the 14 kHz MAS ^{27}Al NMR spectra of the γ-Al_2O_3 and χ-Al_2O_3 samples obtained by calcination of pseudoboehmite and gibbsite at 650 °C accordingly. The spectra were recorded at ambient temperature using the Bruker AVANCE 400 Fourier NMR spectrometer (9.4 T constant magnetic field) at the ^{27}Al Larmor frequency of 104.31 MHZ. A single π/6 sequence was used with the pulse length of 0.5 μs and 2 s delay between the experiments. 1024 accumulations were made for both samples. 1 M solution of $AlCl_3$ was used as an external reference at 0 ppm. The NMR parameters (Table S1) were obtained by decomposition of the experimental into Czjzek Simple profiles using Dmfit software. The main parameter for the determination of metastable alumina phases is the ratio between $Al^{[6]}$ and $Al^{[4]}$ sites, which in our case agreed well with various literature data.

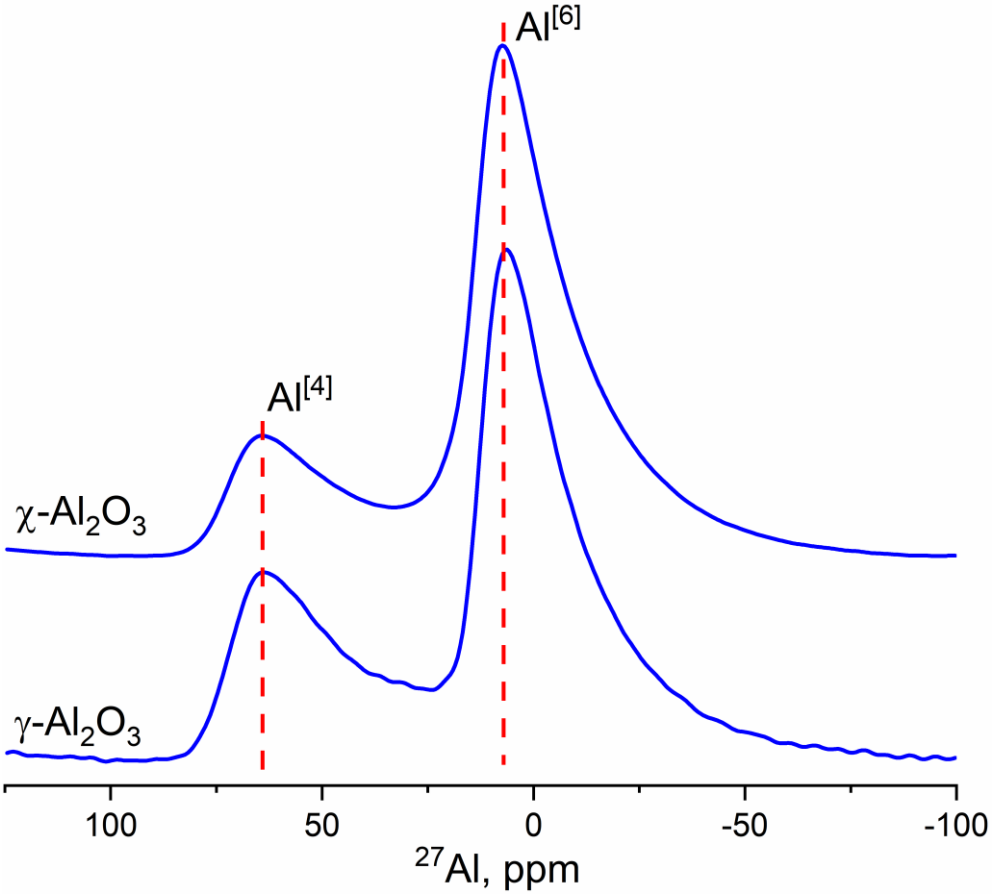

Figure S2. 14 kHz MAS ^{27}Al NMR spectra of γ-Al_2O_3 and χ-Al_2O_3 samples obtained by calcination of pseudoboehmite and gibbsite at 650 °C. Dashed lines depict the position of $Al^{[6]}$ and $Al^{[4]}$ bands that have a typical Czjzek Simple profile.

Table S1. NMR parameters of γ-Al_2O_3 and χ-Al_2O_3 obtained by decomposition of the experimental spectra.

	γ-Al_2O_3		**χ-Al_2O_3**	
	$Al^{[6]}$	**$Al^{[4]}$**	**$Al^{[6]}$**	**$Al^{[4]}$**
δ_{iso}, ppm	14.1	73.2	14.2	71.9
C_Q, MHz	5.1	6.1	4.3	5.6
Relative intensity, %	66	34	74	26

4.4 Conclusion

In this, chapter we have applied ^{59}Co Internal Field NMR to establish the influence of the support surface on the structure of the supported Co nanoparticles on the industrially relative example of alumina-supported Fischer-Tropsch catalysts. Previously, researchers have demonstrated both numerically and experimentally that the type of the available vacancy for anchoring the Co^{2+} ions from aqueous impregnation solution affects greatly the stability of the anchored Co site and the dispersion of Co over the surface of the support. This is the **initial** stage of metal Co deposition through the process of incipient wetness impregnation, which is widely used for preparation of Co catalysts. In turn, the approach used here addressed the cumulative effect of the initial impregnation and consecutive thermal treatments (calcination and reduction) on the structure of the **resulting** Co nanoparticles.

In order to focus on the effect of the support surface on the structure of Co nanoparticles, we studied the samples with extremely small Co contents that still allowed observing the NMR signal. A useful side effect of such a small Co content was the lack of necessity to consider the width of particle size distribution as evident from **Chapter 3** and thus the experiments were conducted at a single cryogenic temperature.

According to the experimental data obtained by both TEM and ^{59}Co IF NMR, the surface of χ-Al_2O_3 favored the formation of larger Co nanoparticles with higher *hcp* content, while the use of γ-Al_2O_3 led to a higher dispersion of Co over the support surface. This was consistent with the semi-empirical predictions based on ^{1}H NMR and modelling of the surfaces of these metastable alumina phases.

The most important difference between these surfaces in terms of interaction with Co turned out to be their hydroxyl coverage: while the (111) crystal plane prominent on the surface of χ-Al_2O_3 supports only bridging hydroxyl groups, the hydroxyl coverage of the (110) crystal plane dominant in γ-Al_2O_3 can be described as a mixture of terminal and bridging hydroxyls. The latter hydroxyl coverage facilitates the anchoring of Co ions on the surface of γ-Al_2O_3 which leads to higher dispersion of the resulting Co metal nanoparticles and consequently their smaller sizes and tendency to *fcc* crystal packing. At the same time, the hydroxyl coverage of χ-Al_2O_3 promotes clustering of Co, which results in larger particles after reduction.

Thus, we have demonstrated that ^{59}Co IF NMR can be used as a tool for investigation of the effect that different support surfaces have on the structure of the resulting Co nanoparticles. The

practical result that the little-studied χ-Al_2O_3 phase promotes the formation of larger Co nanoparticles with tendency to *hcp* structure (i. e. particles with higher activity in Fischer-Tropsch synthesis) may be interesting for further investigation of this alumina as a prospective catalyst support.

4.5 References

[1] A.M. Portis, A.C. Gossard, Nuclear Resonance in Ferromagnetic Cobalt, Journal of Applied Physics. 31 (1960) S205–S213. https://doi.org/10.1063/1.1984666.

[2] M. Kawakami, T. Hihara, Y. Kōi, T. Wakiyama, The Co ^{59} Nuclear Magnetic Resonance in Hexagonal Cobalt, J. Phys. Soc. Jpn. 33 (1972) 1591–1598. https://doi.org/10.1143/JPSJ.33.1591.

[3] T.W. van Deelen, C. Hernández Mejía, K.P. de Jong, Control of metal-support interactions in heterogeneous catalysts to enhance activity and selectivity, Nat Catal. 2 (2019) 955–970. https://doi.org/10.1038/s41929-019-0364-x.

[4] O. Ducreux, B. Rebours, J. Lynch, M. Roy-Auberger, D. Bazin, Microstructure of Supported Cobalt Fischer-Tropsch Catalysts, Oil & Gas Science and Technology - Revue de l'IFP. 64 (2009) 49–62. https://doi.org/10.2516/ogst:2008039.

[5] D.I. Enache, B. Rebours, M. Roy-Auberger, R. Revel, In Situ XRD Study of the Influence of Thermal Treatment on the Characteristics and the Catalytic Properties of Cobalt-Based Fischer–Tropsch Catalysts, Journal of Catalysis. 205 (2002) 346–353. https://doi.org/10.1006/jcat.2001.3462.

[6] H. Karaca, O. V. Safonova, S. Chambrey, P. Fongarland, P. Roussel, A. Griboval-Constant, M. Lacroix, A.Y. Khodakov, Structure and catalytic performance of Pt-promoted alumina-supported cobalt catalysts under realistic conditions of Fischer–Tropsch synthesis, Journal of Catalysis. 277 (2011) 14–26. https://doi.org/10.1016/j.jcat.2010.10.007.

[7] M.K. Gnanamani, G. Jacobs, W.D. Shafer, B.H. Davis, Fischer–Tropsch synthesis: Activity of metallic phases of cobalt supported on silica, Catalysis Today. 215 (2013) 13–17. https://doi.org/10.1016/j.cattod.2013.03.004.

[8] S. Lyu, L. Wang, J. Zhang, C. Liu, J. Sun, B. Peng, Y. Wang, K.G. Rappé, Y. Zhang, J. Li, L. Nie, Role of Active Phase in Fischer–Tropsch Synthesis: Experimental Evidence of CO Activation over Single-Phase Cobalt Catalysts, ACS Catalysis. 8 (2018) 7787–7798. https://doi.org/10.1021/acscatal.8b00834.

[9] J.-X. Liu, H.-Y. Su, D.-P. Sun, B.-Y. Zhang, W.-X. Li, Crystallographic Dependence of CO Activation on Cobalt Catalysts: HCP versus FCC, Journal of the American Chemical Society. 135 (2013) 16284–16287. https://doi.org/10.1021/ja408521w.

[10] N.E. Tsakoumis, J.C. Walmsley, M. Rønning, W. van Beek, E. Rytter, A. Holmen, Evaluation of Reoxidation Thresholds for γ-Al 2 O 3 -Supported Cobalt Catalysts under Fischer–Tropsch

Synthesis Conditions, Journal of the American Chemical Society. 139 (2017) 3706–3715. https://doi.org/10.1021/jacs.6b11872.

[11] G.L. Bezemer, J.H. Bitter, H.P.C.E. Kuipers, H. Oosterbeek, J.E. Holewijn, X. Xu, F. Kapteijn, A.J. van Dillen, K.P. de Jong, Cobalt Particle Size Effects in the Fischer−Tropsch Reaction Studied with Carbon Nanofiber Supported Catalysts, Journal of the American Chemical Society. 128 (2006) 3956–3964. https://doi.org/10.1021/ja058282w.

[12] A. Barbier, A. Tuel, I. Arcon, A. Kodre, G.A. Martin, Characterization and Catalytic Behavior of Co/SiO2 Catalysts: Influence of Dispersion in the Fischer–Tropsch Reaction, Journal of Catalysis. 200 (2001) 106–116. https://doi.org/10.1006/jcat.2001.3204.

[13] A. Tuxen, S. Carenco, M. Chintapalli, C.-H. Chuang, C. Escudero, E. Pach, P. Jiang, F. Borondics, B. Beberwyck, A.P. Alivisatos, G. Thornton, W.-F. Pong, J. Guo, R. Perez, F. Besenbacher, M. Salmeron, Size-Dependent Dissociation of Carbon Monoxide on Cobalt Nanoparticles, Journal of the American Chemical Society. 135 (2013) 2273–2278. https://doi.org/10.1021/ja3105889.

[14] E. Rytter, N.E. Tsakoumis, A. Holmen, On the selectivity to higher hydrocarbons in Co-based Fischer–Tropsch synthesis, Catalysis Today. 261 (2016) 3–16. https://doi.org/10.1016/j.cattod.2015.09.020.

[15] N.E. Tsakoumis, M. Rønning, Ø. Borg, E. Rytter, A. Holmen, Deactivation of cobalt based Fischer–Tropsch catalysts: A review, Catalysis Today. 154 (2010) 162–182. https://doi.org/10.1016/j.cattod.2010.02.077.

[16] L. Vandewater, G. Bezemer, J. Bergwerff, M. Versluijshelder, B. Weckhuysen, K. Dejong, Spatially resolved UV–vis microspectroscopy on the preparation of alumina-supported Co Fischer–Tropsch catalysts: Linking activity to Co distribution and speciation, Journal of Catalysis. 242 (2006) 287–298. https://doi.org/10.1016/j.jcat.2006.06.004.

[17] J.-B. d'Espinose de la Caillerie, M. Kermarec, O. Clause, Impregnation of. gamma.-Alumina with Ni (II) or Co (II) Ions at Neutral pH: Hydrotalcite-Type Coprecipitate Formation and Characterization, Journal of the American Chemical Society. 117 (1995) 11471–11481.

[18] J.-F. Lambert, M. Che, The molecular approach to supported catalysts synthesis: state of the art and future challenges, Journal of Molecular Catalysis A: Chemical. 162 (2000) 5–18. https://doi.org/10.1016/S1381-1169(00)00318-6.

[19] K. Larmier, C. Chizallet, P. Raybaud, Tuning the Metal-Support Interaction by Structural Recognition of Cobalt-Based Catalyst Precursors, Angewandte Chemie International Edition. 54 (2015) 6824–6827. https://doi.org/10.1002/anie.201502069.

[20] T. Yang, M. Ehara, Probing the electronic structures of Co_n (n = 1–5) clusters on γ-Al_2O_3 surfaces using first-principles calculations, Phys. Chem. Chem. Phys. 19 (2017) 3679–3687. https://doi.org/10.1039/C6CP06785A.

[21] A.S. Andreev, M.A. Kazakova, A. V. Ishchenko, A.G. Selyutin, O.B. Lapina, V.L. Kuznetsov, J.-B. d'Espinose de Lacaillerie, Magnetic and dielectric properties of carbon nanotubes with embedded cobalt nanoparticles, Carbon. 114 (2017) 39–49. https://doi.org/10.1016/j.carbon.2016.11.070.

[22] M.A. Kazakova, A.S. Andreev, A.G. Selyutin, A. V. Ishchenko, A. V. Shuvaev, V.L. Kuznetsov, O.B. Lapina, J.-B. d'Espinose de Lacaillerie, Co metal nanoparticles deposition inside or outside multi-walled carbon nanotubes via facile support pretreatment, Applied Surface Science. 456 (2018) 657–665. https://doi.org/10.1016/j.apsusc.2018.06.124.

[23] I.V. Yakovlev, S.S. Yakushkin, M.A. Kazakova, S.N. Trukhan, Z.N. Volkova, A.P. Gerashchenko, A.S. Andreev, A.V. Ishchenko, O.N. Martyanov, O.B. Lapina, J.-B. d'Espinose de Lacaillerie, Superparamagnetic behaviour of metallic Co nanoparticles according to variable temperature magnetic resonance, Phys. Chem. Chem. Phys. 23 (2021) 2723–2730. https://doi.org/10.1039/D0CP05963C.

[24] A.S. Andreev, D.V. Krasnikov, V.I. Zaikovskii, S.V. Cherepanova, M.A. Kazakova, O.B. Lapina, V.L. Kuznetsov, J. d'Espinose de Lacaillerie, Internal field 59 Co NMR study of cobalt-iron nanoparticles during the activation of CoFe 2 /CaO catalyst for carbon nanotube synthesis, Journal of Catalysis. 358 (2018) 62–70. https://doi.org/10.1016/j.jcat.2017.11.025.

[25] A.C. Gossard, A.M. Portis, M. Rubinstein, R.H. Lindquist, Ferromagnetic Nuclear Resonance of Single-Domain Cobalt Particles, Physical Review. 138 (1965) A1415–A1421. https://doi.org/10.1103/PhysRev.138.A1415.

[26] V. V. Matveev, D.A. Baranov, G.Yu. Yurkov, N.G. Akatiev, I.P. Dotsenko, S.P. Gubin, Cobalt nanoparticles with preferential hcp structure: A confirmation by X-ray diffraction and NMR, Chemical Physics Letters. 422 (2006) 402–405. https://doi.org/10.1016/j.cplett.2006.02.099.

[27] A.S. Andreev, O.B. Lapina, S.V. Cherepanova, A New Insight into Cobalt Metal Powder Internal Field^{59}Co NMR Spectra, Applied Magnetic Resonance. 45 (2014). https://doi.org/10.1007/s00723-014-0580-0.

[28] A.S. Andreev, J.-B. D'Espinose De Lacaillerie, O.B. Lapina, A. Gerashenko, Thermal stability and hcp-fcc allotropic transformation in supported Co metal catalysts probed near operando by ferromagnetic NMR, Physical Chemistry Chemical Physics. 17 (2015). https://doi.org/10.1039/c4cp05327c.

[29] Y. Liu, J. Luo, Y. Shin, S. Moldovan, O. Ersen, A. Hébraud, G. Schlatter, C. Pham-Huu, C. Meny, Sampling the structure and chemical order in assemblies of ferromagnetic nanoparticles by nuclear magnetic resonance, Nature Communications. 7 (2016) 11532. https://doi.org/10.1038/ncomms11532.

[30] K. Pansanga, J. Panpranot, O. Mekasuwandumrong, C. Satayaprasert, J.G. Goodwin, P. Praserthdam, Effect of mixed γ- and χ-crystalline phases in nanocrystalline Al2O3 on the dispersion of cobalt on Al2O3, Catalysis Communications. 9 (2008) 207–212. https://doi.org/10.1016/j.catcom.2007.05.042.

[31] R. Prins, On the structure of γ-Al2O3, Journal of Catalysis. 392 (2020) 336–346. https://doi.org/10.1016/j.jcat.2020.10.010.

[32] S. V Tsybulya, G.N. Kryukova, Nanocrystalline transition aluminas: Nanostructure and features of x-ray powder diffraction patterns of low-temperature Al2O3 polymorphs, Physical Review B. 77 (2008) 24112. https://doi.org/10.1103/PhysRevB.77.024112.

[33] D.F. Khabibulin, E. Papulovskiy, A.S. Andreev, A.A. Shubin, A.M. Volodin, G.A. Zenkovets, D.A. Yatsenko, S.V. Tsybulya, O.B. Lapina, Surface Hydroxyl OH Defects of η-Al_2O_3 and χ-Al_2O_3 by Solid State NMR, XRD, and DFT Calculations, Zeitschrift Für Physikalische Chemie. 231 (2017) 809–825. https://doi.org/10.1515/zpch-2016-0822.

[34] L. Favaro, A. Boumaza, P. Roy, J. Lédion, G. Sattonnay, J.B. Brubach, A.M. Huntz, R. Tétot, Experimental and ab initio infrared study of χ-, κ- and α-aluminas formed from gibbsite, Journal of Solid State Chemistry. 183 (2010) 901–908. https://doi.org/10.1016/j.jssc.2010.02.010.

[35] S.A. Yashnik, A.V. Ishchenko, L.S. Dovlitova, Z.R. Ismagilov, The Nature of Synergetic Effect of Manganese Oxide and Platinum in Pt–MnOX–Alumina Oxidation Catalysts, Top Catal. 60 (2017) 52–72. https://doi.org/10.1007/s11244-016-0722-8.

[36] S.A. Yashnik, V.V. Kuznetsov, Z.R. Ismagilov, Effect of χ-alumina addition on H 2 S oxidation properties of pure and modified γ-alumina, Chinese Journal of Catalysis. 39 (2018) 258–274. https://doi.org/10.1016/S1872-2067(18)63016-5.

[37] D.A. Nazimov, O.V. Klimov, I.G. Danilova, S.N. Trukhan, A.V. Saiko, S.V. Cherepanova, Yu.A. Chesalov, O.N. Martyanov, A.S. Noskov, Effect of alumina polymorph on the dehydrogenation activity of supported chromia/alumina catalysts, Journal of Catalysis. 391 (2020) 35–47. https://doi.org/10.1016/j.jcat.2020.08.006.

[38] K. Pansanga, J. Panpranot, O. Mekasuwandumrong, C. Satayaprasert, J.G. Goodwin, P. Praserthdam, Effect of mixed γ- and χ-crystalline phases in nanocrystalline Al2O3 on the dispersion of cobalt on Al2O3, Catalysis Communications. 9 (2008) 207–212. https://doi.org/10.1016/j.catcom.2007.05.042.

[39] I. V. Yakovlev, A.M. Volodin, V.O. Stoyanovskii, O.B. Lapina, A.F. Bedilo, Effect of carbon coating on the thermal stability of nanocrystalline χ-Al2O3, Materials Chemistry and Physics. 240 (2020) 122135. https://doi.org/10.1016/j.matchemphys.2019.122135.

[40] I. V. Yakovlev, A.M. Volodin, V.I. Zaikovskii, V.O. Stoyanovskii, O.B. Lapina, A.A. Vedyagin, Stabilizing effect of the carbon shell on phase transformation of the nanocrystalline alumina particles, Ceramics International. 44 (2018) 4801–4806. https://doi.org/10.1016/j.ceramint.2017.12.066.

[41] P. Panissod, J.P. Jay, C. Meny, M. Wojcik, E. Jedryka, NMR analysis of buried metallic interfaces, Hyperfine Interact. 97–98 (1996) 75–98. https://doi.org/10.1007/BF02150169.

[42] J.R. Yates, C.J. Pickard, F. Mauri, Calculation of NMR chemical shifts for extended systems using ultrasoft pseudopotentials, Physical Review B. 76 (2007) 024401. https://doi.org/10.1103/PhysRevB.76.024401.

[43] P.E. Blöchl, Projector augmented-wave method, Physical Review B. 50 (1994) 17953–17979. https://doi.org/10.1103/PhysRevB.50.17953.

[44] J.P. Perdew, J.A. Chevary, S.H. Vosko, K.A. Jackson, M.R. Pederson, D.J. Singh, C. Fiolhais, Atoms, molecules, solids, and surfaces: Applications of the generalized gradient approximation for exchange and correlation, Physical Review B. 46 (1992) 6671–6687. https://doi.org/10.1103/PhysRevB.46.6671.

[45] B.G. Pfrommer, M. Côté, S.G. Louie, M.L. Cohen, Relaxation of Crystals with the Quasi-Newton Method, Journal of Computational Physics. 131 (1997) 233–240. https://doi.org/10.1006/jcph.1996.5612.

[46] S.J. Clark, M.D. Segall, C.J. Pickard, P.J. Hasnip, M.I.J. Probert, K. Refson, M.C. Payne, First principles methods using CASTEP, Zeitschrift Für Kristallographie - Crystalline Materials. 220 (2005) 567–570. https://doi.org/10.1524/zkri.220.5.567.65075.

[47] J.P. Perdew, K. Burke, M. Ernzerhof, Generalized Gradient Approximation Made Simple, Physical Review Letters. 77 (1996) 3865–3868. https://doi.org/10.1103/PhysRevLett.77.3865.

[48] D. Vanderbilt, Soft self-consistent pseudopotentials in a generalized eigenvalue formalism, Physical Review B. 41 (1990) 7892–7895. https://doi.org/10.1103/PhysRevB.41.7892.

[49] M.F. Hansen, S. Mørup, Models for the dynamics of interacting magnetic nanoparticles, Journal of Magnetism and Magnetic Materials. 184 (1998) L262-274. https://doi.org/10.1016/S0304-8853(97)01165-7.

[50] D.L. Leslie-Pelecky, R.D. Rieke, Magnetic Properties of Nanostructured Materials, Chem. Mater. 8 (1996) 1770–1783. https://doi.org/10.1021/cm960077f.

[51] O. Kitakami, H. Sato, Y. Shimada, F. Sato, M. Tanaka, Size effect on the crystal phase of cobalt fine particles, Phys. Rev. B. 56 (1997) 13849–13854. https://doi.org/10.1103/PhysRevB.56.13849.

[52] G. Mattei, C. de Julián Fernández, P. Mazzoldi, C. Sada, G. De, G. Battaglin, C. Sangregorio, D. Gatteschi, Synthesis, Structure, and Magnetic Properties of Co, Ni, and Co−Ni Alloy Nanocluster-Doped SiO_2 Films by Sol−Gel Processing, Chem. Mater. 14 (2002) 3440–3447. https://doi.org/10.1021/cm021106r.

[53] W. Sucksmith, The magnetic anisotropy of cobalt, Proc. R. Soc. Lond. A. 225 (1954) 362–375. https://doi.org/10.1098/rspa.1954.0209.

[54] C. Chizallet, C. Schlaup, E. Fonda, X. Carrier, Surface orientation dependent interaction of cobalt (II) precursors with alpha-alumina, Journal of Catalysis. 394 (2021) 157–166. https://doi.org/10.1016/j.jcat.2020.10.025.

[55] G. Busca, The surface of transitional aluminas: A critical review, Catalysis Today. 226 (2014) 2–13. https://doi.org/10.1016/j.cattod.2013.08.003.

[56] H. Knözinger, P. Ratnasamy, Catalytic Aluminas: Surface Models and Characterization of Surface Sites, Catalysis Reviews. 17 (1978) 31–70. https://doi.org/10.1080/03602457808080878.

[57] M. Digne, P. Sautet, P. Raybaud, P. Euzen, H. Toulhoat, Hydroxyl Groups on γ-Alumina Surfaces: A DFT Study, Journal of Catalysis. 211 (2002) 1–5. https://doi.org/10.1006/jcat.2002.3741.

[58] M. Digne, Use of DFT to achieve a rational understanding of acid?basic properties of ?-alumina surfaces, Journal of Catalysis. 226 (2004) 54–68. https://doi.org/10.1016/j.jcat.2004.04.020.

[59] X. Krokidis, P. Raybaud, A.-E. Gobichon, B. Rebours, P. Euzen, H. Toulhoat, Theoretical Study of the Dehydration Process of Boehmite to γ-Alumina, J. Phys. Chem. B. 105 (2001) 5121–5130. https://doi.org/10.1021/jp0038310.

[60] A.T.F. Batista, D. Wisser, T. Pigeon, D. Gajan, F. Diehl, M. Rivallan, L. Catita, A.-S. Gay, A. Lesage, C. Chizallet, P. Raybaud, Beyond γ-Al2O3 crystallite surfaces: The hidden features of edges revealed by solid-state 1H NMR and DFT calculations, Journal of Catalysis. 378 (2019) 140–143. https://doi.org/10.1016/j.jcat.2019.08.009.

[61] T. Pigeon, C. Chizallet, P. Raybaud, Revisiting γ-alumina surface models through the topotactic transformation of boehmite surfaces, Journal of Catalysis. 405 (2022) 140–151. https://doi.org/10.1016/j.jcat.2021.11.011.

[62] H.C. Stumpf, A.S. Russell, J.W. Newsome, C.M. Tucker, Thermal Transformations of Aluminas and Alumina Hydrates - Reaction with 44% Technical Acid., Ind. Eng. Chem. 42 (1950) 1398–1403. https://doi.org/10.1021/ie50487a039.

[63] V.P. Pakharukova, D.A. Yatsenko, E.Y. Gerasimov, S.V. Tsybulya, A study of γ-Al2O3 from the viewpoint of 3D nanostructure, Journal of Solid State Chemistry. 302 (2021) 122425. https://doi.org/10.1016/j.jssc.2021.122425.

[64] C.V. Chandran, C.E.A. Kirschhock, S. Radhakrishnan, F. Taulelle, J.A. Martens, E. Breynaert, Alumina: discriminative analysis using 3D correlation of solid-state NMR parameters, Chem. Soc. Rev. 48 (2019) 134–156. https://doi.org/10.1039/C8CS00321A.

[65] D.A. Yatsenko, V.P. Pakharukova, S.V. Tsybulya, Low Temperature Transitional Aluminas: Structure Specifics and Related X-ray Diffraction Features, Crystals. 11 (2021) 690. https://doi.org/10.3390/cryst11060690.

[66] D.A. Ksenofontov, Yu.K. Kabalov, Structure refinement and thermal stability of gibbsite, Inorg Mater. 48 (2012) 142–144. https://doi.org/10.1134/S0020168512020136.

[67] J.M.R. Mercury, P. Pena, A.H. de Aza, D. Sheptyakov, X. Turrillas, On the Decomposition of Synthetic Gibbsite Studied by Neutron Thermodiffractometry, J American Ceramic Society. 89 (2006) 3728–3733. https://doi.org/10.1111/j.1551-2916.2006.01191.x.

[68] T. Mitsui, T. Matsui, R. Kikuchi, K. Eguchi, Microstructural Transformation with Heat-Treatment of Aluminum Hydroxide with Gibbsite Structure, BCSJ. 82 (2009) 618–623. https://doi.org/10.1246/bcsj.82.618.

[69] M. Salmeron, H. Bluhm, M. Tatarkhanov, G. Ketteler, T.K. Shimizu, A. Mugarza, X. Deng, T. Herranz, S. Yamamoto, A. Nilsson, Water growth on metals and oxides: binding, dissociation and role of hydroxyl groups, Faraday Discuss. 141 (2009) 221–229. https://doi.org/10.1039/B806516K.

[70] X. Deng, T. Herranz, C. Weis, H. Bluhm, M. Salmeron, Adsorption of Water on Cu_2O and Al_2O_3 Thin Films, J. Phys. Chem. C. 112 (2008) 9668–9672. https://doi.org/10.1021/jp800944r.

General conclusions

This PhD thesis is devoted to the development and application of ^{59}Co Internal Field nuclear magnetic resonance technique to study Co nanoparticles. Metallic Co nanoparticles play an important role in various fields of science and technology including heterogeneous catalysis where they are most famously used in the process for production of synthetic fuels – Fischer-Tropsch synthesis. These nanoparticles are intricate objects of study due to the complicated interconnections of their various properties: the physical and chemical (catalytic) properties of Co nanoparticles depend on their size, shape and crystal structure which itself depends on temperature and interaction with the surface on which the particles are supported. Consequently, an efficient application of Co nanoparticles in any field of interest requires the most detailed study of these properties and their connections.

One of the most informative techniques that can be used for studying the Co nanoparticles is ^{59}Co Internal Field nuclear magnetic resonance (^{59}Co IF NMR) – an unconventional magnetic resonance technique, where no external magnetic field is used, but the absorption of radio frequency radiation still happens due to the presence of strong internal magnetic field. This rarely used technique was efficiently applied to studies of bulk Co metal structures as well as various alloys of Co with different metals. ^{59}Co IF NMR is extremely informative about the structure of Co particles since its spectra contain the information about their crystal and magnetic structure as well as particle sizes and presence of guest atoms in the nearest environment of Co nucleus. Another important advantage of this technique is its bulk nature, which distinguishes it from any local techniques such as different electron microscopy approaches. At the same time, the analysis of the ^{59}Co IF NMR experimental spectra is very complicated due to the various interactions and structural features affecting their shape.

Thus, in this work we have studied two different model systems that allowed us to exclude some of the interactions in order to simplify the analysis of the ^{59}Co IF NMR spectra. A brief introduction to the theoretical aspects of this technique was given in **Chapter 1** to familiarize the reader with this unconventional technique. In **Chapter 2**, the details of the experimental approaches were provided with the main focus on ^{59}Co IF NMR.

Chapter 3 was devoted to studying the size effect of Co nanoparticles on the IF NMR spectra. It is well known that at high temperature (or conversely, when their volume becomes too small) ferromagnetic Co nanoparticles undergo a transition into superparamagnetic state, which for ^{59}Co IF NMR leads to a complete loss of signal. This property of Co nanoparticles can then be used to characterize their size, namely their volume distribution by varying the measurement temperature.

Thus, we have used a model sample consisting of small Co nanoparticles embedded inside the inner channels of multi-walled carbon nanotubes that served both as the support for separation of particles and as the Co particle size limiter. For these small particles we have observed almost no signal at room temperature, but at 30 K there was a drastic increase in spectral intensity that could not be attributed to any effect other than transition of superparamagnetic particles into ferromagnetic state – "blocking".

Using the supplementary techniques of high resolution transmission electron microscopy (HRTEM) and ferromagnetic resonance spectroscopy we were able to determine the superparamagnetic relaxation constant in the model of superparamagnetism originally developed by Néel. Consequently, this allowed us to analyze the obtained ^{59}Co IF NMR spectra using this model and achieve a good agreement with data obtained using HRTEM.

The method of the variable temperature ^{59}Co IF NMR demonstrates a great potential since it can be used to study the crystal and magnetic structure of Co particles in different regions of the size distribution separately from each other. Additionally, an inverse problem may be solved if enough statistics is gathered on the spectra of Co nanoparticles with different sizes – modelling the ^{59}Co IF NMR spectra based on the given particle size distribution obtained, for example, by TEM. Such approach may prove useful since TEM experiments are generally much quicker and less expensive than the IF NMR experiments.

In **Chapter 4**, another factor influencing the ^{59}Co IF NMR spectra was studied – the effect of the support surface, which is topical in the field of heterogeneous catalysis, where supported catalysts are often used. This study was conducted on the model case of samples of Fischer-Tropsch synthesis (FTS) catalysts supported on metastable alumina phases, with TEM and semi-empirical modelling used as supplementary techniques. Using ^{59}Co IF NMR, we have demonstrated that the surface of the χ-Al_2O_3 promotes formation of larger particles with higher *hcp* content compared to γ-Al_2O_3, something of consequence with respect with FTS activity and selectivity.

In order to explain such a difference between these supports, we have employed a ^{1}H NMR based semi-empirical approach that allowed us to model the surfaces of these metastable aluminas and most importantly their hydroxyl coverages. We have found that the hydroxyl coverage of (111) crystal plane dominant in χ-Al_2O_3 consists exclusively of bridging hydroxyl groups that make it less reactive toward aqueous Co^{2+} cations. At the same time the (110) crystal plane prominent in γ-Al_2O_3 includes both bridging and terminal hydroxyls that help to stabilize the Co^{2+} ions on the surface of the support and thus lead to a higher dispersion of Co after the reduction of the catalyst.

Such a semi-empirical approach may prove useful in the assessment of reactivity of other supports (including but not limited to metastable alumina phases) towards aqueous solutions of Co^{2+} during the initial stages of incipient wetness impregnation. At the same time, ^{59}Co IF NMR served here as a tool for analyzing the influence of both the initial stage of catalyst preparation and further thermal treatments on the structure of the resulting Co nanoparticles. Such a combination provides both a way to predict the influence of the support and a way to test this prediction. In the case of γ- and χ-Al_2O_3 we can say that the latter phase promotes the formation of particles closer to desirable parameters for Fischer-Tropsch synthesis, thus making the χ-Al_2O_3 a promising candidate as an FTS catalyst support.

The main goal of this work was to establish some basic relation between two important characteristics of materials containing Co nanoparticles and the experimentally observed ^{59}Co IF NMR spectra using well chosen model systems. We have demonstrated that this technique can be used as a tool for description of particle size distributions in the bulk of a sample. We have also shown that IF NMR can probe possible particle-support interactions. It is necessary to note here, that the contributions to the experimental spectra are not limited to the two factors that were the focus of this work. Such factors as interparticle interactions and substitution of Co with guest atoms may play a much more important role in different types of samples. Thus, we believe that ^{59}Co IF NMR has a great potential as a characterization technique in various application areas such energy storage materials, electromagnetic shielding materials, bimetallic and high entropy systems.

Even though the experimental procedure for ^{59}Co IF NMR experiment seems well established and agreed upon, there are still ways to improve the experimental setup. Particularly interesting may be the experimental arrangement that includes a constant but varying external magnetic field that would add a dedicated quantification direction to the experiment. Such an approach can be used to study the magnetic properties of strongly anisotropic systems such as Co nanowires or 2D layered systems.

RÉSUMÉ

Les propriétés chimiques de nanoparticules de Co supportées dépendent de leur taille, de leur morphologie, de leur structure cristalline et de la force de l'interaction avec le support. Ces caractéristiques se reflètent dans les propriétés magnétiques des nanoparticules, notamment dans la distribution du champ magnétique hyperfin à travers la particule et donc dans leur ferromagnétisme et dans la fréquence de résonance des noyaux de ^{59}Co dans une expérience de RMN à champ interne (IF NMR). Cette technique de RMN non conventionnelle est un outil puissant pour étudier la structure cristalline et magnétique du cobalt métallique ainsi que l'environnement local des noyaux de Co dans des matériaux ferromagnétiques. Cependant, l'application de cette technique est entravée par la nature complexe des spectres expérimentaux qui sont soumis à diverses contributions. Ainsi, l'objectif principal de ce travail était d'établir les effets sur les spectres IF NMR du ^{59}Co de deux aspects particulièrement importants dans l'application à la catalyse hétérogène : la distribution de la taille des particules et l'interaction avec la surface du support.

L'effet de la distribution de la taille des particules a été démontré sur un échantillon modèle de petites nanoparticules de Co supportées sur des nanotubes de carbone multi-parois où la transition des particules de l'état superparamagnétique à l'état ferromagnétique a été observée en utilisant la spectroscopie IF NMR du ^{59}Co. La température d'une telle transition pour une particule individuelle est liée à son volume, ce qui rend possible l'utilisation de la spectroscopie IF NMR pour la caractérisation de la distribution de la taille des particules dans un échantillon.

L'influence de la surface du support sur la structure des nanoparticules de Co a été étudiée en utilisant des échantillons supportés sur alumine. Selon les mesures de ^{59}Co IF NMR, la surface de χ-Al_2O_3 a favorisé la formation de plus grandes particules de Co de structure principalement *hcp*. En utilisant des calculs semi-empiriques, nous avons montré qu'un tel effet du support sur la structure des nanoparticules de Co était dû à la couverture hydroxyle de l'alumine.

MOTS CLÉS

RMN en champ interne; Catalyse; Ferromagnetisme

ABSTRACT

The chemical properties of supported Co nanoparticles depend on their size, morphology, crystal structure, and the strength of interaction with the support. These characteristics reflect themselves in the magnetic properties of ferromagnetic nanoparticles, namely in the distribution of the hyperfine magnetic field across the particle and thus in the resonant frequency of ^{59}Co nuclei in a ^{59}Co Internal Field NMR (IF NMR) experiment. This unconventional NMR technique is a powerful tool for studying the crystal and magnetic structure of ferromagnetic metallic cobalt as well the local environment of Co nuclei. However, the application of this technique is hindered by the complicated nature of the experimental spectra that are subject to contributions from various sources. Thus, the main aim of this work was to establish the effects on ^{59}Co IF NMR spectra of two aspects particularly important in heterogeneous catalysis – particle size distribution and metal-support interaction.

The effect of particle size distribution was demonstrated on a model sample of small Co nanoparticles supported on multi-walled carbon nanotubes where the transition of the particles from superparamagnetic to ferromagnetic state was observed using ^{59}Co IF NMR spectroscopy. The temperature of such a transition for an individual particle depends on its volume, making it possible to use ^{59}Co IF NMR to characterize particle size distribution in a sample.

The influence of the support surface on the structure of the Co nanoparticles was investigated using samples supported on metastable alumina phases. According to the ^{59}Co IF NMR, the surface of χ-Al2O3 promoted formation of larger Co particles and favored the *hcp* crystal structure. Using semi-empirical calculations, we suggest that the hydroxyl coverage of the alumina is the main support characteristic determining the Co nanoparticles structure.

KEYWORDS

Internal Field NMR; Catalysis; Ferromagnetism